DEVELOPMENT OF A SYSTEM MEASURING ADHESION FORCES IN POWDER COLLECTIVES

DISSERTATION

zur Erlangung des Grades
"Doktor der Naturwissenschaften"
im Promotionsfach Physik

Fachbereich Physik, Mathematik und Informatik
der Johannes Gutenberg-Universität
in Mainz

Stefanie Wanka
geboren in Mainz

Mainz, Oktober 2013

Tag der mündlichen Prüfung: 08. Januar 2014
1. Berichterstatter: [In der elektronischen Fassung aus Datenschutzgründen entfernt]
2. Berichterstatter: [In der elektronischen Fassung aus Datenschutzgründen entfernt]
Dissertation an der Universität Mainz (D77)

Zusammenfassung

Feine Pulver weisen im Allgemeinen schlechte Fließ- und Dispergiereigenschaften auf, da sie auf Grund starker Haftkräfte (Adhäsionskräfte) zwischen den Pulver-Partikeln zur Bildung von Agglomeraten neigen. Die Kenntnis über die Adhäsionskräfte in Partikel-Kollektiven ist unverzichtbar um ein tieferes, grundlegendes Verständnis der mechanischen Eigenschaften von Partikeln und des Partikelverhaltens in Pulvern zu erlangen. Besonders im Bereich der pharmazeutischen Industrie spielt die Kontrolle der Partikel-Adhäsion für die Erhöhung der Leistungsfähigkeit von Inhalationsprodukten, beispielsweise von Trockenpulver-Inhalatoren, eine entscheidende Rolle. Die Größe inhalierbarer Partikel liegt hierbei typischerweise im Bereich $1-5\,\mu\mathrm{m}$.

Im Rahmen der vorliegenden Arbeit wurde eine neue Methode zur Messung von Partikel-Adhäsionskräften entwickelt, welche eine Alternative zu den konventionellen Methoden darstellt. Konventionelle, weitverbreitete Methoden sind die Colloidal Probe- und die Zentrifugentechnik, die allerdings beide nicht nur mit großem experimentellen und zeitlichen Aufwand verbunden, sondern auch in ihrer Anwendbarkeit begrenzt sind.

Die neu entwickelte Methode basiert auf der Ablösung einzelner Pulver-Partikel von einer Oberfläche auf Grund der Partikel-Massenträgheit. Die hierfür nötige Beschleunigung der Oberfläche, welche in der Größenordnung von $500\,000\,g$ liegt, wird von einem Hopkinson-Stab-Stoßerreger erzeugt und mittels Laser-Doppler-Vibrometrie gemessen. Die Partikelablösung wird während des Experiments mit optischer Video-Mikroskopie detektiert. Durch anschließende automatisierte Datenauswertung kann eine statistische Verteilung von Partikel-Adhäsionskräften erhalten werden.

Um die neue Methode zu validieren wurden die Adhäsionskräfte von Polystyrol- und Silica-Mikrokugeln auf einer mit Polystyrol beschichteten Stahloberfläche unter Umgebungsbedingungen gemessen. Hier war es möglich, mit einem einzigen Experiment Adhäsionswerte von mehr als 150 einzelnen Partikeln im Größenbereich $3-13\,\mu\mathrm{m}$ zu erhalten. Dies erlaubt eine statistische Datenauswertung, während Messaufwand und Messzeit im Vergleich zu den konventionellen Methoden erheblich geringer sind. Die gemessenen Adhäsionkräfte der kleineren Partikel zeigten eine gute Übereinstimmung mit Werten aus Colloidal Probe-Messungen und theoretischen Vorhersagen. Für größere Partikel hingegen wurde ein stärkeres Anwachsen der Adhäsion mit dem Partikeldurchmesser beobachtet. Diese Abweichung könnte durch den Einfluss der Oberflächenrauigkeit und -heterogenität verursacht werden, welche sich auf kleine und große Partikel unterschiedlich auswirken.

Durch Messung der Adhäsionskräfte von Dextran-Partikeln mit gewellter Morphologie und Größen bis minimal 2 µm konnte gezeigt werden, dass die Hopkinson-Stab-Methode ebenfalls zur Charakterisierung komplexerer Probensysteme geeignet ist. Die neue Apparatur bietet daher die Möglichkeit, eine große Vielzahl unterschiedlicher Partikel-Oberflächen-Kombinationen routinemäßig zu untersuchen. Dies schließt auch stark kohäsive Pulver mit ein, wie beispielsweise Inhalationspulver, die in der pharmazeutischen Industrie zur Behandlung von Atemwegserkrankungen zum Einsatz kommen.

Abstract

Fine powders commonly have poor flowability and dispersibility due to interparticle adhesion that leads to formation of agglomerates. Knowing about adhesion in particle collectives is indispensable to gain a deeper fundamental understanding of particle behavior in powders. Especially in pharmaceutical industry a control of adhesion forces in powders is mandatory to improve the performance of inhalation products. Typically the size of inhalable particles is in the range of $1 - 5\,\mu\text{m}$.

In this thesis, a new method was developed to measure adhesion forces of particles as an alternative to the established colloidal probe and centrifuge technique, which are both experimentally demanding, time consuming and of limited practical applicability.

The new method is based on detachment of individual particles from a surface due to their inertia. The required acceleration in the order of $500\,000\,g$ is provided by a Hopkinson bar shock excitation system and measured via laser vibrometry. Particle detachment events are detected on-line by optical video microscopy. Subsequent automated data evaluation allows obtaining a statistical distribution of particle adhesion forces.

To validate the new method, adhesion forces for ensembles of single polystyrene and silica microspheres on a polystyrene coated steel surface were measured under ambient conditions. It was possible to investigate more than 150 individual particles in one experiment and obtain adhesion values of particles in a diameter range of $3 - 13\,\mu\text{m}$. This enables a statistical evaluation while measuring effort and time are considerably lower compared to the established techniques. Measured adhesion forces of smaller particles agreed well with values from colloidal probe measurements and theoretical predictions. However, for the larger particles a stronger increase of adhesion with diameter was observed. This discrepancy might be induced by surface roughness and heterogeneity that influence small and large particles differently.

By measuring adhesion forces of corrugated dextran particles with sizes down to $2\,\mu\text{m}$ it was demonstrated that the Hopkinson bar method can be used to characterize more complex sample systems as well.

Thus, the new device will be applicable to study a broad variety of different particle-surface combinations on a routine basis, including strongly cohesive powders like pharmaceutical drugs for inhalation.

Contents

1 Introduction

1.1 Introduction and Motivation

Granular matter is a large assembly of solid particles with sizes ranging between few micrometers and several meters. The term includes coarse granules such as sand, rice, corn, coal or debris but also any kind of powders containing micrometer-sized particles. Thus, granular matter is omnipresent in nature and our everyday life and also used in a broad variety of industrial applications.

Fine powders, which contain particles smaller than 10 μm, are of particular interest. As drug, food or cosmetics powders, fertilizers or toner particles: fine powders are used in industry to a great extent. In pharmaceutical industry they are of special relevance in pulmonary drug delivery, since the size of inhalable particles reaching the human alveoli is typically in a range of $1-5$ μm [1, 2].

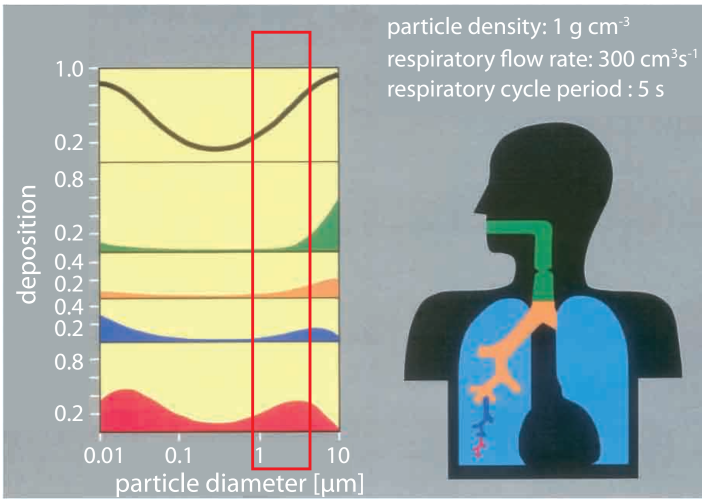

Figure 1.1: Total (black curve) and regional (colored curves) deposition of spherical powder particles in the human respiratory tract after oral inhalation, predicted by a deposition model [2]. In contrast to particles with diameters above 5 μm, which mainly deposit in the extra-thoracic or bronchial region, particles with diameters in a range of $1-5$ μm reach the alveolar region (red box). Since submicron particles (first peak of the red curve) are not usable for aerosol medicines, inhalation powders have to contain drug particles in a range of $1-5$ μm.

Inhalation powders are mainly used to treat airway diseases, such as asthma, chronic obstructive pulmonary disease (COPD) or cystic fibrosis (CF). However, they also offer the possibility to be used for vaccination or to treat diseases which do not directly affect the lungs, like diabetes or migraine [3, 4].

After inhaling the particles are carried with the tidal air through the human respiratory tract and deposit due to sedimentation, inertial impaction and diffusion [5]. In which region of the airways they deposit does not only depend on the breathing pattern of the person but also on particle density and particle diameter. Figure 1.1 shows the deposition of unity-density spheres in the human respiratory tract predicted by a deposition model [2]. Particles in a diameter range of $1-5\,\mu\text{m}$ are able to reach the alveolar region (red box in Figure 1.1), whereas larger particles mainly deposit in the extrathoracic or bronchial region (green, orange and blue in Figure 1.1). Most of the submicron particles with diameters between 0.2 and $1\,\mu\text{m}$ are exhaled before migration to the lung walls [6, 7]. There is in fact an enhanced deposition in the alveolar region also for ultrafine particles with diameters in a range of $0.01-0.2\,\mu\text{m}$ (first peak in the red curve in Figure 1.1). However, this size range is not used for aerosol medicines, since an appropriate formulation technology to generate ultrafine particles is lacking. Furthermore, particles in this size range can deliver only a very small drug dose within a reasonable aerosol volume and inhalation time [8]. Thus, pharmaceutical inhalation powders targeting the human alveoli have to contain drug particles with a diameter range of $1-5\,\mu\text{m}$.

However, fine powders commonly have very poor flow and dispersion properties. The reason is the formation of particle agglomerates due to interparticle adhesion forces. The adhesion force, which is caused by attractive surface forces, is the maximum force needed to overcome the attractive interaction and separate two attaching particles. Especially for particles in the size range of $1-5\,\mu\text{m}$, surface forces are by far dominating over inertial forces, making these powders strongly cohesive and resulting in a poor flow and dispersion behavior.

Knowing about the adhesion forces of particles is important from the fundamental point of view, since it is indispensable to gain a deeper understanding of the flow behavior of powders. Many experimental as well as theoretical and numerical studies have already been carried out to better describe particle flow properties and mechanics of granular matter [9–13]. Nevertheless, a full understanding of mechanical microcontacts in particular is lacking so far. One reason is that even relatively monodisperse powders show wide distributions of adhesion forces rather than a single value. In these powders adhesion forces of particles can vary by a factor of two to ten [14–16] which is caused by surface roughness and surface heterogeneity [17–20].

Knowlege about the adhesion forces between particles is of great significance for many industrial applications as well. This includes storage, mixing and dosing of powders, surface cleaning in semiconductor industry, printing or food powders processing. Especially in pharmaceutical industry an improvement of the dispersibility of inhalation powders is desired. Here, the agglomerates in the cohesive drug powder have to be successfully dispersed in the Dry Powder Inhaler (DPI) (Figure 1.2, HandiHaler® by Boehringer Ingelheim as example) before inhalation into the lungs, otherwise particles cannot reach the alveolar region [21, 22]. So far, much effort has been made in particle engineering to optimize the powder properties of pharmaceutical drugs [7, 23–25].

Figure 1.2: Example of a Dry Powder Inhaler (DPI): the HandiHaler® by Boehringer Ingelheim.

In order to improve powder dispersibility and hence the performance of inhalation products, a control of adhesion forces is mandatory, concerning the adhesion between particles and between particles and the walls of the inhaler device.
However, existing techniques for measuring particle adhesion forces are experimentally demanding, time consuming and of limited practical applicability [26]. This includes the two most widely used methods: the colloidal probe technique using an atomic force microscope (AFM) [27, 28] and the centrifuge method [14, 29]. For colloidal probe measurements each single particle has to be attached manually to the end of a microcantilever. The adhesion force is measured by moving the sample under the cantilever up and down and recording the cantilever deflection. However, the high preparation effort limits the number of particles that can be investigated. Moreover, the direction of contact is predetermined and the particle cannot adjust freely as it is the case in real powders. In centrifuge experiments, which have as well been applied to pharmaceutical powders [30–32], adhesion forces are measured by detecting inertial detachment of particles from a surface. Here, a large number of particles can be measured simultaneously. However, evacuation and spin up/down times for each acceleration value make it a very time consuming method. Since both techniques are not usable for routine applications an alternative method to measure adhesion forces of powder particles is needed.

1.2 Aims of the Thesis

This thesis starts with the aim to develop a new method for measurement of particle adhesion forces as an alternative to the established methods.
As model system to characterize adhesion of fine powders, the interaction between single

microparticles and a flat substrate shall be considered. The new technique should offer the possibility to study particle collectives, meaning an ensemble of individual particles simultaneously, which enables a good statistical evaluation. Measurements should be less time consuming and effortful compared to the established methods. Thus, the new method should have the potential to be used on a routine base, e.g. for standard analysis in industrial research. Another important point is that it shall be possible to investigate particles with sizes in the range of $1 - 5\,\mu\text{m}$. This is of great significance for pharmaceutical industry, since it includes cohesive drug powders used for inhalation.

The new method should be based on inertial detachment of particles from a substrate. Hence, the initial idea is to place single particles on a surface, retract the surface with a high acceleration, and observe their detachment due to their inertia. In this thesis a technical system has to be found to realize a mechanical excitation of the substrate in order to detach particles in the mentioned size range. An experimental set-up shall be constructed, which enables adhesion force measurements by optical detection of particle detachment events and recording the surface acceleration.

After development and construction of the set-up adhesion forces shall be measured using different particle-surface combinations. These measurements should serve to validate the new method and assess its potential for future applications but also help to deepen the fundamental knowledge about mechanical microcontacts, regarding the influence of surface roughness or heterogeneity, for instance.

1.3 Overview

The structure of this thesis is the following:

Chapter 2 gives an introduction of the fundamentals of contact mechanics, describing basic principles of surface forces, such as van der Waals, electrostatic and capillary forces, surface and adhesion energy as well as elastic properties of solids. Furthermore, the common contact theories like Hertz, Johnson-Kendall-Roberts (JKR), Derjaguin-Muller-Toporov (DMT) and Rabinovich model are discussed.

In **chapter 3** the established techniques to measure adhesion forces of particles are presented. Starting with the colloidal probe technique, the principles of imaging and force measurement with the atomic force microscope (AFM) are explained. Afterwards the centrifuge method is introduced and an overview of the advantages and drawbacks of the established methods is given.

Chapter 4 describes the theory of elastic waves in solids. The new technique for measurement of particle adhesion developed in this thesis uses the Hopkinson bar principle which is based on the propagation of elastic waves in a long thin rod. Hence, fundamentals of elastic wave motion in solids are introduced and a historical outline of the Hopkinson and Kolsky bar is presented.

Chapter 5 deals with the new technique to measure adhesion of particles using a Hopkinson bar. Considering the requirements the system has to fulfill, the development of the method is described, starting with the basic idea of the principle and the creation of a first concept. Afterwards, the technical conversion is presented by explaining details of the experimental set-up, followed by a description of the measuring procedure and the development of programs for automatic data evaluation.

Chapter 6 contains the materials used for the adhesion measurements with the new Hopkinson bar method. The employed powders and surfaces are presented as well as the sample preparation. Moreover, different methods that were used for material characterization are described.

In this work, comparative measurements were carried out using the colloidal probe technique. In **chapter 7** it is shown how the colloidal probes were prepared. Additionally, the measurement of force-versus-distance curves with the used samples as well as the subsequent data evaluation to obtain adhesion forces are explained.

Results and discussion of the Hopkinson bar measurements are presented in **chapter 8**. This chapter contains adhesion measurements with spherical polystyrene particles ($4 - 13\,\mu\text{m}$) in comparison with colloidal probe measurements and theoretical predictions using the JKR and Rabinovich approach. Furthermore, results from experiments with spherical silica particles ($3-7\,\mu\text{m}$) in comparison with theory values are shown and discussed. This is followed by the presentation of measured adhesion forces of corrugated dextran particles ($2 - 4\,\mu\text{m}$).

Finally, in **chapter 9** the main results of the thesis are summarized and a conclusion of the work is drawn. The Hopkinson bar method is assessed according its relevance for industry and research and some perspectives for future applications are proposed.

2 Fundamentals of Contact Mechanics

The focus of this work lies on the experimental study of adhesive forces between microscale particles and planar surfaces. In order to gain an understanding of the interaction between solid bodies it is necessary to consider the elastic properties as well as surface forces, which govern the mechanical microcontact. Thus, in this chapter fundamentals of contact mechanics are introduced, including the relevant forces, elasticity properties of solids and the most prominent adhesion theories[1].

2.1 Surface Forces

Surface forces strongly influence the interactions between solid bodies, especially in the micron sized range, where they are the dominant interaction forces. In many applications there is the need to control forces between particles, between particles and surfaces or between two surfaces.

However, the expression "surface force" is more general. It does not only include forces between solids in a fluid medium but also between all different kinds of interfaces. Examples are interactions between two liquid-vapor-interfaces that can be found in foams or between a solid-liquid and a liquid-vapor interface, which corresponds to a thin liquid film on a solid surface. Furthermore the expression includes forces between macromolecules or lipid bilayers.

Depending on the concerned surfaces and the surrounding medium many different forces are relevant, leading to an attractive or repulsive interaction: van der Waals forces, capillary forces, electrostatic double layer forces (charged solid surfaces in liquids), solvation and hydration forces or hydrodynamic forces (moving solids in a fluid).

This work deals with the adhesion force between two solid surfaces in air. If two bodies are brought into mechanical contact, attractive surface forces will lead to adhesion. Per definition the adhesion force is the maximum force needed to overcome the attractive interaction and separate the two bodies again [33], depending on the strength of the attractive forces, the contact area and the minimum distance between them. Many different forces may contribute such as van der Waals forces F_{vdW}, electrostatic forces F_{el},

---

[1] This chapter is mainly based on [33] and [34]

chemical and hydrogen bonding forces F_{chem} and F_H, capillary forces F_{cap} and others. The adhesion force between two bodies is the sum of all contributions:

$$F_{adh} = F_{vdW} + F_{el} + F_{chem} + F_H + F_{cap} + ... \tag{2.1}$$

Therefore adhesion does not only depend on the materials of the two objects but also on the ambient conditions. For micro- and nanocontacts capillary condensation and therefore relative humidity can play an important role. Moreover, all solid bodies in contact deform, either due to external or to surface forces. As a consequence, to describe adhesion realistically, it is mandatory to explicitly calculate the forces for a given contact geometry and to also take the surface deformations into account. Different contact models are discussed in 2.4.

2.1.1 Van der Waals Force

One of the main contributions to the adhesion force between two solid bodies is the van der Waals force.

Van der Waals forces exist between all combinations of molecules and macroscopic objects. In the latter case, they originate from a complex interplay of the forces between the molecules in the objects and the medium separating them.

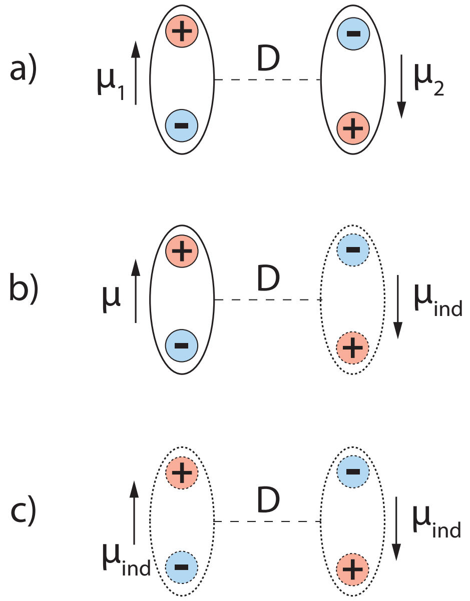

Figure 2.1: Schematic illustration of the three contributions to the van der Waals interaction between two molecules: (a) Keesom dipole-dipole interaction, (b) Debye dipole-induced dipole interaction and (c) London induced dipole-induced dipole interaction

The van der Waals force between neutral molecules has three different contributions that sum up to an attractive force [35–37]:

1. **Keesom interaction**: describes the interaction between two static dipoles, which are free to rotate (Figure 2.1a), corresponding to two molecules with permanent dipole moments (polar). On one hand, the dipoles prefer to orient with their opposite charges facing each other, on the other hand the thermal motion leads to an orientational fluctuation driving them away from the preferential orientation. The balance between both effects leads to a net attraction between the dipoles, which can be calculated by weighted averaging over all orientations. The Helmholtz free energy for this system is called the Keesom energy:

   $$V(D) = -\frac{\mu_1^2 \mu_2^2}{3(4\pi\varepsilon_0)^2 k_B T D^6} = -\frac{C_K}{D^6} \tag{2.2}$$

   with the dipole moments μ_1 and μ_2, the vacuum permittivity ε_0, the Boltzmann constant k_B, the temperature T and the distance D between the dipoles.

2. **Debye interaction**: describes the interaction between a static dipole which is free to rotate, corresponding to a polar molecule, and a molecule with induced dipole moment (Figure 2.1b). The molecule with permanent dipole moment μ induces a dipole moment $\mu_{ind} = \alpha \cdot E$ in the second molecule which has the polarizability α. Here E is the electric field strength created by the permanent dipole. This leads to an attraction between both and to the Helmholtz free energy of

   $$V(D) = -\frac{\mu^2 \alpha}{(4\pi\varepsilon_0)^2 D^6} = -\frac{C_D}{D^6} \tag{2.3}$$

   The Debye interaction can explain the attractive force between a polar and a nonpolar molecule, but one should note that this interaction also arises between two identical polarizable molecules with permanent dipole moments.

3. **London dispersion interaction**: describes the interaction between two molecules with induced dipole moments (Figure 2.1c). Due to quantum mechanical fluctuations of the charge distributions of the interacting molecules, instantaneous dipoles form. These fluctuating dipoles induce dipole moments in the other molecule which leads to a net attractive force. The Helmholtz free energy is

   $$V(D) = -\frac{3\alpha_1 \alpha_2}{2(4\pi\varepsilon_0)^2 D^6} \frac{h\nu_1 \nu_2}{(\nu_1 + \nu_2)} = -\frac{C_L}{D^6} \tag{2.4}$$

   with the polarizabilities α_1 and α_2 of the molecules and their ionization energies $h\nu_1$ and $h\nu_2$. Via the London dispersion interaction the attraction between two nonpolar molecules can be explained, which is not possible using classical physics but quantum mechanics. However, also polar molecules interact via dispersion forces, not only via Keesom and Debye forces.

Summation of these three contributions results in the attractive van der Waals interaction between two neutral molecules with the potential energy

$$V_{vdW}(D) = -\frac{C_{vdW}}{D^6} \quad \text{with} \quad C_{vdW} = C_K + C_D + C_L \tag{2.5}$$

The van der Waals interaction forms the attractive term in the Lennard Jones potential between two neutral molecules, consisting of an attractive term $\propto -1/D^6$ and a repulsive term $\propto 1/D^{12}$. The latter only plays a role at very short distances between the molecules, where the electron orbitals start to overlap leading to a Pauli repulsion.

Microscopic Approach

To calculate the van der Waals forces between macroscopic solids two different approaches exist: a microscopic approach developed by Hamaker [38], where the discrete atomic structure of the solid is considered, and a macroscopic approach, developed by Lifshitz [39], which treats the solid as a continuum.
In the microscopic approach, Hamaker assumed pairwise additivity, which means that the interactions between pairs of molecules are summed up ignoring the influence of the neighboring molecules on this interaction. Although this concept is an approximation, it helps to qualitatively understand van der Waals interactions between macroscopic objects and to derive analytical equations.
At first, the van der Waals energy between a molecule A and an infinitely extended body of molecules B with planar surface is calculated (Figure 2.2).

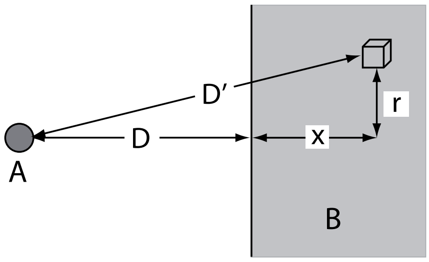

Figure 2.2: Calculation of the van der Waals energy between a molecule A and an infinitely extended body of molecules B with planar surface [33].

Using Equation 2.5 that represents the potential energy between two molecules A and B, the interaction energies between molecule A and all molecules in solid B are summed up:

$$\begin{aligned} V_{molA/planeB} &= -C_{AB} \iiint_V \frac{\rho_B}{D'^6} dV \\ &= -C_{AB}\rho_B \int_0^\infty \int_0^\infty \frac{2\pi r}{((D+x)^2+r^2)^3}\, dr\, dx \\ &= -\frac{\pi \rho_B C_{AB}}{6D^3} \end{aligned} \tag{2.6}$$

Compared to the van der Waals energy between two molecules, which decreases proportional to $1/D^6$, the energy between a molecule and a macroscopic solid decreases less strongly, proportional to $1/D^3$.

The second step is to calculate the interaction between two infinitely extended solid objects A and B, by integrating over all molecules in A using Equation 2.6. The van der Waals energy per area is

$$\begin{aligned} w &= \frac{V_{planeA/planeB}}{A} = -\frac{\pi \rho_A \rho_B C_{AB}}{6} \int_0^\infty \frac{1}{(D+x)^3}\, dx \\ &= -\frac{A_H}{12\pi D^2} \end{aligned} \tag{2.7}$$

with a $1/D^2$ dependence. ρ_A and ρ_B are the molecular densities in material A and B, respectively. Here, the Hamaker constant was introduced, which is defined as

$$A_H = \pi^2 C_{AB} \rho_A \rho_B \tag{2.8}$$

depending only on the material characteristics.

The force per unit area is given by the negative derivative of the energy per area w:

$$f = -\frac{A_H}{6\pi D^3} \tag{2.9}$$

Important for many applications is the van der Waals interaction between two spheres with radii R_1 and R_2 or between a sphere and a planar surface.

For the sphere/sphere geometry, assuming that the radii are significantly larger than the distance D, one obtains the potential energy

$$V(D) = -\frac{A_H}{6D} \cdot \frac{R_1 R_2}{R_1 + R_2} \quad \text{for} \quad D \ll R_1, R_2 \tag{2.10}$$

and the van der Waals force

$$F_{vdW} = -\frac{dV(D)}{dD} = -\frac{A_H}{6D^2} \cdot \frac{R_1 R_2}{R_1 + R_2} \qquad \text{(sphere/sphere)} \tag{2.11}$$

For the sphere/plane geometry R_2 goes to infinity and Equation 2.11 simplifies to

$$F_{vdW} = -\frac{A_H}{6D^2} \cdot R \qquad \text{(sphere/plane)} \tag{2.12}$$

In contact, the distance D equals the typical interatomic spacing $D = D_0 \approx 0.17\,\text{nm}$. Obviously, as Hamaker recognized, the distance dependence of the van der Waals interaction between macroscopic bodies can substantially differ from the $1/D^6$ dependence for single molecules. As a consequence, van der Waals forces between bodies can be much longer ranged than originally expected and reach significant values for small D. In most cases they are one of the main reasons for the high adhesive forces between objects in the lower micron size range, as for example powder particles.

Macroscopic Approach

The main problem of the microscopic approach is that the influence of neighboring molecules on the interaction between any molecule pair is ignored. In contrast to Hamaker, Lifshitz developed a macroscopic approach for the theoretical description of van der Waals forces between macroscopic solids by treating them as continuous materials with certain optical "bulk" properties like permittivity and refractive index. Thus, the problem of additivity can be avoided. The most important finding of the Lifshitz theory is that the form of the equations derived by Hamaker, especially the distance dependencies, are still valid. Only the Hamaker constant A_H is calculated differently.
In his theory, Lifshitz considered the forces between two dielectric plane half-spaces of material 1 and 2, separated by a distance d in vacuum [39]. His theory was extended together with Dzyaloshinskii and Pitaevskii [40] by including the effect of a third dielectric medium in the gap. In this configuration, the two materials interact by exchange of virtual photons. The presence of an intervening medium with refractive index > 1 influences the exchange by increasing the optical path of the photons leading to a reduced interaction. The Hamaker constant for material 1 interacting with material 2 across medium 3 is

$$\begin{aligned} A_H = {} & \frac{3}{4} k_B T \cdot \left(\frac{\varepsilon_1 - \varepsilon_3}{\varepsilon_1 + \varepsilon_3}\right) \cdot \left(\frac{\varepsilon_2 - \varepsilon_3}{\varepsilon_2 + \varepsilon_3}\right) \\ & + \frac{3h}{4\pi} \int_{\nu 1}^{\infty} \left(\frac{\varepsilon_1(i\nu) - \varepsilon_3(i\nu)}{\varepsilon_1(i\nu) + \varepsilon_3(i\nu)}\right) \cdot \left(\frac{\varepsilon_2(i\nu) - \varepsilon_3(i\nu)}{\varepsilon_2(i\nu) + \varepsilon_3(i\nu)}\right) d\nu \end{aligned} \tag{2.13}$$

with the Planck constant h, the static permittivities of the three media ε_1, ε_2 , ε_3, which are the values of the dielectric function at zero frequency, and the permittivities $\varepsilon_1(i\nu)$, $\varepsilon_2(i\nu)$, $\varepsilon_3(i\nu)$ at imaginary frequencies $i\nu$. Furthermore, $\nu_1 = 3.9 \cdot 10^{13}$ Hz at 25°C. The first term in 2.13 represents the Keesom and Debye energy.
For a nonconductive material the permittivity can be approximated by

$$\varepsilon(i\nu) = 1 + \frac{n^2 - 1}{1 + \nu^2/\nu_e^2} \tag{2.14}$$

with the refractive index n and the mean ionization frequency ν_e of the material, which is typically in the order of $3 \cdot 10^{15}$ Hz. Assuming that the ionization frequencies of the three materials are the same, one obtains the following approximation:

$$\begin{aligned} A_H \approx\ & \frac{3}{4} k_B T \cdot \left(\frac{\varepsilon_1 - \varepsilon_3}{\varepsilon_1 + \varepsilon_3}\right) \cdot \left(\frac{\varepsilon_2 - \varepsilon_3}{\varepsilon_2 + \varepsilon_3}\right) \\ & + \frac{3h\nu_e}{8\sqrt{2}} \cdot \frac{(n_1^2 - n_3^2) \cdot (n_2^2 - n_3^2)}{\sqrt{n_1^2 + n_3^2} \cdot \sqrt{n_2^2 + n_3^2} \cdot \left(\sqrt{n_1^2 + n_3^2} + \sqrt{n_2^2 + n_3^2}\right)} \end{aligned} \tag{2.15}$$

where n_1, n_2, n_3 are the refractive indices of the three materials.
The Hamaker constant A_H can be either positive, corresponding to an attractive force, or negative, corresponding to a repulsive force. Thus, in contrast to van der Waals forces between single molecules, that are always attractive, van der Waals interactions between macroscopic bodies might also be repulsive. Equation 2.15 allows to predict the sign of A_H and therefore the nature of the force. Van der Waals forces between similar materials ($\varepsilon_1 = \varepsilon_2$, $n_1 = n_2$) and between different materials in vacuum or gases ($\varepsilon_3 = n_3 = 1$) are always attractive, whereas forces between different materials in a condensed phase can also be repulsive.
For estimating the Hamaker constant Equation 2.15 is a useful approximation. However, Hamaker constants for different material systems are usually calculated from spectroscopic data taking all frequencies into account, which leads to more precise values. For nonconducting materials they are typically in the order of $10^{-21} - 10^{-20}$J, for metals they are about one magnitude higher, typically in the range of 10^{-19}J.

2.1.2 Electrostatic Forces

Electrostatic forces between two contacting macroscopic objects may contribute to their adhesion as well. The bodies can have a surface charge, leading to attraction or repulsion,

depending on the polarity.
In the case of two nonconductive spheres the electrostatic force is given by

$$F_{el} = \frac{\pi}{\varepsilon_0 \varepsilon_r} \cdot \frac{Q_1 Q_2 R_P^2}{\left(1 + \frac{D}{2R_P}\right)^2} \tag{2.16}$$

with the surface charges Q_1, Q_2 of the spheres, the sphere radius $R_1 = R_2 = R_P$, the distance D between the spheres and $\varepsilon_0, \varepsilon_r$ the permittivity of vacuum and the surrounding medium, respectively. In the case of antipolar charged spheres Equation 2.16 is an attractive force, for unipolar charged spheres it is a repulsive force. In contact, D can be replaced by the typical interatomic distance $D = D_0 \approx 0.17\,\mathrm{nm}$.

2.1.3 Capillary Force

The ambient conditions also influence the adhesive force between two solid bodies in contact. The relative humidity in particular, can have a significant impact on adhesion and may determine the behavior of powders. Capillary condensation of water from the surrounding air leads to the formation of a liquid meniscus in the contact area and therefore to an attraction between the two objects. Thus, capillary forces have to be taken into account in studies of powders and granular materials [11, 41–46], adhesion between particles and particles to surfaces [47, 48].
In order to understand capillary forces it is necessary to shortly introduce the fundamental terms and equations describing liquid surfaces.

Surface Tension

The most fundamental quantity in this context is the liquid surface tension. To increase the surface area of a liquid by dA, work hast to be done:

$$dW = \gamma_L \cdot dA \tag{2.17}$$

The proportionality constant γ_L is called the surface tension of the liquid and depends on the composition of the liquid and the vapor, temperature and pressure. Increasing the surface area of a liquid is always related to the creation of new surface by increasing the number of molecules N at the surface. Considering a liquid-vapor interface on the microscopic scale, this concept can be explained as follows: the molecules in the bulk, which are completely surrounded by neighboring molecules, attract each other by different forces like van der Waals forces or hydrogen bonds. However, the molecules at the surface are only partially surrounded by neighbouring molecules, which is energetically unfavorable. Thus, to bring a molecule from the bulk to the surface and increase the surface area, work has to be done. The surface tension is therefore a measure of the interaction strength between the liquid molecules.

Young-Laplace Equation

If a liquid surface in equilibrium is curved, a pressure difference between the two phases exists. The relation between pressure difference and the curvature of the surface is given by the Young-Laplace [49, 50] equation

$$\Delta P = \gamma_L \cdot \left(\frac{1}{R_1} + \frac{1}{R_2} \right) \tag{2.18}$$

where R_1 and R_2 are the principal radii of curvature. This can be illustrated by the following example: If the end of a tube is closed with a piece of stretched rubber (Figure 2.3), the membrane will remain planar as long as the inside and outside pressures are equal. The reason is that the surface tension tends to minimize the surface area. To obtain a curved surface, the pressure inside the tube has to be different from the pressure outside, which makes the membrane bulge in or out of the tube.

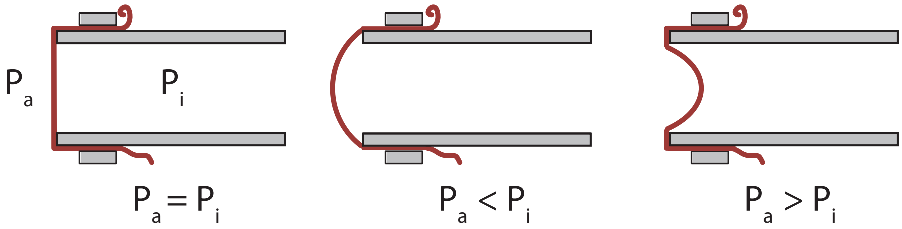

Figure 2.3: Scheme illustrating the Laplace pressure [34]: The end of a tube is closed with a stretched rubber membrane. In order to curve the surface, the inner pressure P_i has to be different from the outside pressure P_a.

This pressure difference ΔP is called the Laplace pressure. For a sphere, corresponding to a droplet or a bubble, the two principal radii are identical $R_1 = R_2 = R$, leading to a Laplace pressure of $\Delta P = 2\gamma_L/R$. However, for large structures where gravitation plays a role, the hydrostatic pressure has to be added to the term in Equation 2.18.

Contact Angle

Another important term is the liquid contact angle. If a liquid drop is placed on a solid surface usually the edge forms a defined contact angle Θ between the tangent of the drop at the location of contact and the surface (Figure 2.4).

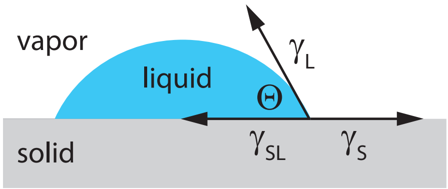

Figure 2.4: Schematic of a liquid drop on a flat solid surface with its contact angle Θ.

This means that a three-phase (solid-liquid-vapor) contact line is established. *Young's equation* relates the contact angle to the interfacial tensions γ_S, γ_L and γ_{SL}:

$$\gamma_{SL} + \gamma_L \cos\Theta = \gamma_S \tag{2.19}$$

The contact angle gives information about a liquid ability to spread over a certain solid surface and is therefore an inverse measure of wetting. A contact angle of zero $\Theta = 0$ corresponds to full wetting, $0 < \Theta < 90°$ to partial wetting, $90° \leqslant \Theta < 180°$ to low wetting and $\Theta = 180°$ corresponds to non wetting.

The terms hydrophilicity and hydrophobicity of surfaces are defined via the contact angle of a water droplet sitting on the surface: if $\Theta \leqslant 90°$ the surface is called hydrophilic, if $\Theta > 90°$ it is called hydrophobic.

The most common method to experimentally measure liquid contact angles and surface tension is the *sessile drop method*, where the drop shape is analyzed. A small droplet of the liquid is placed with a capillary tube on top of the horizontal surface and illuminated by a light source. After imaging the static drop with a microscope laterally, its contour can be fitted by the Young-Laplace equation, considering also the hydrostatic pressure, to obtain contact angle or surface tension. Here, rotational symmetry around the vertical axis is assumed.

Kelvin Equation and Capillary Condensation

The Kelvin equation [51] relates the vapor pressure of a liquid to its curvature:

$$\ln\frac{P_K}{P} = \frac{\gamma_L V_m}{RT}\left(\frac{1}{R_1} + \frac{1}{R_2}\right) \tag{2.20}$$

where P and P_K are the vapor pressures of the flat and the curved surface in equilibrium, respectively, γ_L is the liquid surface tension, V_m the liquid molar volume and R the universal gas constant. Inside a drop, for example, the Laplace pressure is raised which makes the molecules evaporate more easily and therefore leads to a higher vapor pressure than for a flat surface. On the contrary, in a bubble, the vapor pressure is lower, since the pressure in the liquid is reduced, which makes it more difficult for the molecules to evaporate.

Capillary condensation, which is responsible for the capillary force, having influence on the adhesion between solid bodies, is one of the most important applications of the Kelvin equation. Even for vapor pressures below the equilibrium vapor pressure of the liquid with planar surface, vapor condenses into capillaries or fine pores. The condensation continues until the radius of curvature of the liquid reaches the value given by the Kelvin equation (2.20). As a consequence, liquids are strongly adsorped into porous materials. Furthermore, capillary condensation in the gap of the contact zone between two bodies leads to a capillary force. In particular in the case of fine powders, capillary forces enhance adhesive forces between the particles and influence powder behavior. If two spherical particles are in contact, condensing liquid (usually water from the surrounding air) forms a curved meniscus in the contact zone (Figure 2.5), provided that the liquid wets the surface of the particles.

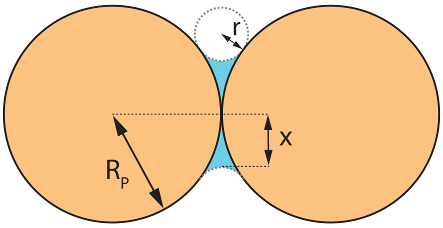

Figure 2.5: Liquid meniscus in the contact zone of two spherical particles leading to the attractive capillary force.

Since the Laplace pressure in the liquid is lower than the outside pressure this leads to an attractive force between the spheres, the capillary force

$$F_{cap} = 2\pi\gamma_L R_P \tag{2.21}$$

which depends on the surface tension of the liquid γ_L (usually water) and the particle radius of the spheres R_P ($R_1 = R_2 = R_P$). Surprisingly, Equation 2.21 neither depends on the curvature of the liquid meniscus, nor on the vapor pressure. The reason is that a decrease of vapor pressure causes a decrease of the meniscus radius r and the meniscus length x, but the Laplace pressure increases by the same amount. However, Equation 2.21 is an approximation assuming perfectly smooth, spherical and rigid particles and a liquid wetting the surfaces. Real capillary forces are strongly influenced by the exact contact geometry [52]. Due to surface roughness effects they are mostly much smaller than the calculated values. Elastic deformation of the surfaces plays an additional role. Furthermore, the relative humidity of the surroundings as well as the wettability of the particles has indeed an effect on the adhesive force [47, 53].

2.2 Surface Energy and Adhesion Energy

Considering a liquid, the energy dW to increase the surface area by dA is given by Equation 2.17 with the surface tension γ_L. For liquids an increase in surface area is always related to an increase in the number of molecules N at the surface while the area per molecule stays constant. Therefore surface tension and surface energy are identical. However, for solids this is not the case. The surface area of a solid can be increased by two ways: the first is an increase in the number of molecules N at the surface like for the liquid, which corresponds to a plastic change. The second is to stretch the surface elastically which causes an increase of the area per molecule at constant N. As a consequence the surface energy γ^S contains an elastic and a plastic contribution [33]:

$$dW = \gamma^S dA \quad \text{with} \quad \gamma^S = E_S \frac{\partial N}{\partial A} + N \frac{\partial E_S}{\partial A} \tag{2.22}$$

Here E_S is an excess energy which is associated with each molecule.
For a purely plastic change in surface area the surface energy is similar to that of a liquid and is called *surface tension* of the solid:

$$\gamma^S_{plastic} \equiv \gamma_S \tag{2.23}$$

For a purely elastic change the surface energy is the sum of surface tension and the change of surface tension with the elastic strain $\varepsilon_{elastic}$

$$\gamma^S_{elastic} = \gamma_S + \frac{\partial \gamma_S}{\partial \varepsilon_{elastic}} \equiv \Upsilon, \tag{2.24}$$

where Υ is called *surface stress.*
However, in most cases new surface area is created by both, a plastic and an elastic change. Therefore the surface energy of a solid is

$$\begin{aligned} \gamma^S &= \gamma_S + \frac{\partial \gamma_S}{\partial \varepsilon_{tot}} \\ &= \gamma_S \frac{d\varepsilon_{plastic}}{d\varepsilon_{tot}} + \Upsilon \frac{d\varepsilon_{elastic}}{d\varepsilon_{tot}} \end{aligned} \tag{2.25}$$

with the total strain $\varepsilon_{tot} = dA/A$ and the plastic strain $\varepsilon_{plastic}$. This means that work has to be done to expand the surface against the surface tension γ_S and the surface stress Υ.
Especially for the calculation of adhesion forces the surface energy of solids is of great significance. Mostly a detailed calculation of all affected surface forces is difficult and instead surface energy considerations are used, which is a simpler approach.

If a crystalline block with cross-sectional area A is cleaved in the middle, work has to be done to break all cohesive bonds in the cleavage interface and create new surface area of $2A$. This new surface is then in a highly energetic state since the energy used to form the bonds is now available at the surface. The work per unit area needed to separate two blocks of different materials with surface energies γ_1^S and γ_2^S and interfacial energy γ_{12} is

$$w_{adh} = \gamma_1^S + \gamma_2^S - \gamma_{12} \tag{2.26}$$

which is the adhesion energy or work of adhesion. Thus, w_{adh} characterizes the adhesion strength between two objects. In other words, the formation of interface between two materials leads to a reduction of surface energy. For two identical materials w becomes the work of cohesion $w = 2\gamma^S$.

However, experimental adhesion forces may be much lower than expected from surface energy considerations, due to surface roughness or contamination effects. Additionally, capillary forces may have a strong influence.

2.3 Elastic Behavior of Solids

Assuming solids to be rigid is in most cases an oversimplification since they will usually deform under an external force. Therefore, in order to calculate adhesion forces between solid bodies it is necessary to take the surface deformation into account.

The stress in units Pa=N/m^2 acting on a material is per definition the ratio of force and cross-section area:

$$\sigma = \frac{F}{A} \tag{2.27}$$

As a response to stress, the material will deform. The relative elongation is called strain:

$$\varepsilon_x = \frac{\Delta L_x}{L_x} \tag{2.28}$$

with the length of the object L_x in x-direction and its change in length ΔL_x in x-direction. A positive strain corresponds to a stretch of the material, whereas a negative strain corresponds to a compression.

For very small strains, stress and strain are related to each other via the general Hooke's law

$$\sigma_{ij} = C_{ijkl}\varepsilon_{kl} \quad \text{with} \quad i,j,k,l = 1,2,3 \tag{2.29}$$

where σ_{ij} is the stress tensor, ε_{kl} is the strain tensor and C_{ijkl} is the fourth-order stiffness tensor. For an isotropic elastic material, a stress σ_x which is applied only in x-direction, results in a strain ε_x in x-direction. Hence, Hooke's law simplifies to

$$\sigma_x = E\varepsilon_x \tag{2.30}$$

with Young's modulus E. This linear relation between stress and strain is valid only in the linear elastic regime of the material, which means for strains $\varepsilon < 1\%$. Higher stresses lead to plastic deformation or material failure. As an example, Figure 2.6 shows a stress-strain curve representing the typical behavior of many metals. Above a certain yield point the curve deviates from the original linear relation and the material deforms plastically or even ruptures.

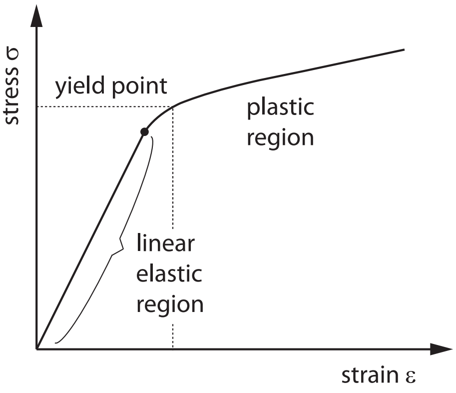

Figure 2.6: Schematic of a stress-strain curve typical for many metals [54].

Many materials behave according to the Poisson effect: If they are stretched in a particular direction, they will contract in the directions perpendicular to that direction (Figure 2.7).

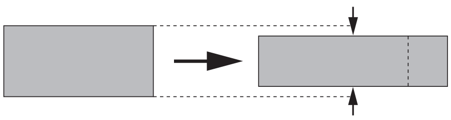

Figure 2.7: Scheme illustrating the Poisson effect: a stretch in one direction leads to a contraction in the directions perpendicular to this direction.

The poisson ratio ν characterizes the amount of contraction and has typically a value between 0.2 and 0.5. If a material is stretched for example in x-direction, the contractions in y- and z-direction are

$$\varepsilon_y = \varepsilon_z = -\nu\varepsilon_x \tag{2.31}$$

2.4 Contact Models

In order to calculate adhesion forces accurately it is mandatory to take surface deformations of the concerned bodies into account, depending on the contact geometry. Several models exist which consider the finite elasticity of the contacting solids.
Heinrich Hertz was the first who solved the problem of the elastic contact between two spheres and between a sphere and a planar surface in 1882. Since surface forces are not included in his model, Johnson, Kendall and Roberts extended his theory in 1971, taking also adhesive forces between the spheres within their contact zone into account (JKR model). In 1975 an alternative contact model was introduced by Derjaguin, Muller and Toporov, considering attractive surface forces outside the contact zone of the spheres (DMT model). Later in the early 1990s, Maugis developed a more general theory which can explain the transition between JKR and DMT model: both are the limiting cases of his Maugis-Dugdale theory.

2.4.1 Hertz Model

Hertz model [55] describes the elastic contact between two spheres or between a sphere and a planar surface. The main assumptions are the following:

- Surfaces are continuous, smooth and elastic
- Strains are small, within the elastic limit
- Contact radius is small compared to the sphere radii
- Frictionless contact
- No tensile stress within the area of contact
- No surface forces between the spheres

For the sphere/sphere geometry under an external load F_L Hertz derived an equation for the contact radius a

$$a^3 = \frac{3R^*}{4E^*} \cdot F_L \tag{2.32}$$

with the reduced radius R^* and the reduced Young's modulus E^*, which are defined as

$$\frac{1}{R^*} = \frac{1}{R_1} + \frac{1}{R_2} \tag{2.33}$$

$$\frac{1}{E^*} = \frac{1-\nu_1^2}{E_1} + \frac{1-\nu_2^2}{E_2} \tag{2.34}$$

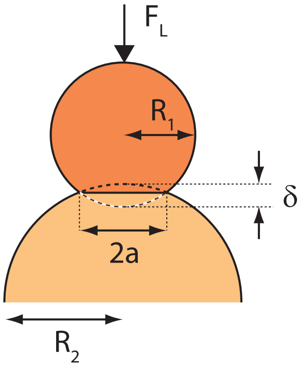

Figure 2.8: Two elastic particles in contact according to Hertz model.

Thus, according to Equation 2.32, the contact area πa^2 of the spheres changes with load. The contact radius determines the indentation δ

$$\delta = \frac{a^2}{R^*} \tag{2.35}$$

As a consequence, the force versus indentation relationship is

$$F_L = \frac{4}{3} E^* \sqrt{R^*} \cdot \delta^{3/2} \tag{2.36}$$

which shows that the contact does not act as a linear spring since the contact area changes with load. Thus, the contact stiffness $dF_L/d\delta = 2E^* a$ increases with load. Regarding a rigid sphere with radius R_P that indents an elastic half-space ($R \to \infty$), Equations 2.33 and 2.34 simplify to

$$R^* = R_P \tag{2.37}$$

$$E^* = \frac{E_1}{1 - \nu_1^2} \tag{2.38}$$

Figure 2.9 shows schematically the vertical displacement $\Delta z(r)$ of the half-space. Without an external force ($F_L = 0$) according to Equation 2.32 a point-like contact forms because no surface forces are considered.

In Hertz model the contact radius a is supposed to be much smaller than the sphere radius $a \ll R$. The indentation of a rigid sphere into an elastic surface without this approximation was studied by Sneddon [56] and Ting [57].

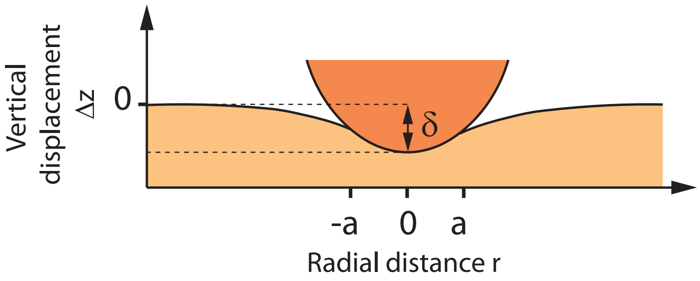

Figure 2.9: Contact between a rigid sphere and an elastic half-space.

2.4.2 JKR Model

In reality, attractive surface forces lead to an adhesion between the spheres and therefore to finite values of the indentation δ and the contact radius a in absence of an external load. Johnson, Kendall and Roberts extended the Hertz model by including adhesive forces, which is known as the JKR theory [58].

With the JKR model, an expression for the adhesion force between two spheres and a sphere and a planar surface can be derived by thermodynamic considerations. The theory is based on the balance between the adhesion energy and the stored elastic deformation energy of the spheres. However, the JKR model only considers adhesion forces within the contact zone, whereas interactions outside the contact zone are neglected.

Due to the adhesive forces the indentation and the contact radius for a given load are increased compared to the Hertzian contact, with a compressive stress within the inner circle of the contact area and a tensile stress near the periphery. Furthermore, a characteristic neck forms, while in the Hertz theory the surface contacts the sphere tangentially (Figure 2.10).

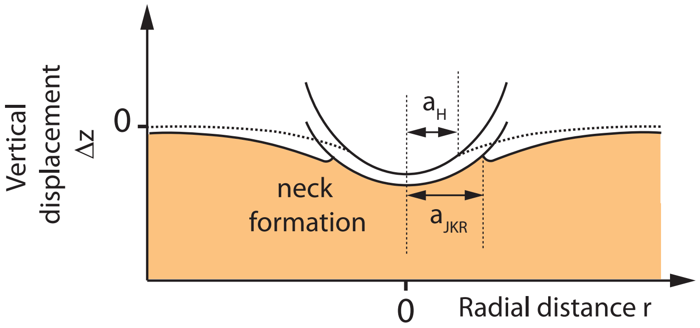

Figure 2.10: Contact between a rigid sphere and an elastic half-space in the JKR model (solid line) compared to the Hertz model (dashed line). In JKR model, due to adhesive forces in the contact zone, a neck forms.

Starting point for the derivation of the adhesion force is Griffith's criterion from fracture mechanics

$$G = \left[\frac{\partial U_E}{\partial A} + \frac{\partial U_P}{\partial A} \right] = w_{adh} \tag{2.39}$$

with the elastic energy U_E, the potential energy U_P and the contact area A. It means that the adherence becomes instable, corresponding to a rupture of the contact, when the energy release rate G equals the adhesion energy per area w_{adh}. From this, an equation for the equilibrium contact radius can be found:

$$a^3 = \frac{3}{4} \frac{R^*}{E^*} \left(F_L + 3\pi w_{adh} R^* + \sqrt{6\pi w_{adh} R^* F_L + (3\pi w_{adh} R^*)^2} \right) \tag{2.40}$$

Here, the first term is the Hertzian contact radius, the additional second and third term are due to the adhesive forces that increase the contact radius.
Without any external load ($F_L = 0$), unlike in Hertz model, the contact radius is different from zero:

$$a_0 = \left(\frac{9\pi w_{adh} R^{*2}}{2E^*} \right)^{\frac{1}{3}} \tag{2.41}$$

The pull-off force, which is the adhesion force, is given by

$$F_{adh} = -\frac{3}{2} \pi w_{adh} R^* \tag{2.42}$$

If the two spheres are from the same material with surface energy γ^S one obtains

$$F_{adh} = -3\pi \gamma^S R^* \tag{2.43}$$

For the sphere/plane geometry this expression simplifies to

$$F_{adh} = -3\pi \gamma^S R_P \tag{2.44}$$

At pull-off, the contact radius is

$$a = a_{min} = 0.63 a_0 \tag{2.45}$$

and the neck height, which corresponds to a negative indentation, is

$$\delta_{min} = -\left(\frac{\pi^2 w_{adh}^2 R^*}{\frac{64}{3} E^{*2}} \right)^{1/3} \tag{2.46}$$

Obviously, the adhesion force is independent of the elastic properties of the materials. The reason is the following: for hard materials the deformation and therefore contact area and attractive surface energy are small, but also the repulsive elastic component is small. For soft materials deformation and contact area are large but also the repulsive elastic component. Both effects compensate each other.
Thus, with the JKR model an expression for the adhesion force could be found only by surface energy considerations without a detailed calculation of all contributing surface forces. However, forces outside the contact area are not taken into account, which leads to an unphysical, infinite tensile stress at the rim of the contact zone. Therefore, with the JKR model adhesion forces can only be realistically predicted for soft materials with large sphere radii and short-ranged forces.

2.4.3 DMT Model

Few years after the development of the JKR model, Derjaguin, Muller and Toporov suggested an alternative theory describing the adhesive contact in the sphere/sphere or sphere/plane geometry, known as the DMT model [59]. In contrast to Johnson et al. they assumed a Hertzian contact profile within the contact and considered adhesion forces only in a circular zone outside the contact area.
To derive an expression for the adhesion force they assumed the surface forces to act as an additional load, which can be added to the Hertzian theory. However, the deformations due to the adhesive forces are not taken into account which leads to an identical surface profile as in Hertz model and to a contact radius of zero at pull-off. The adhesion force in the DMT model is given by

$$F_{adh} = -2\pi w_{adh} R^* \tag{2.47}$$

and

$$F_{adh} = -4\pi\gamma^S R^* \tag{2.48}$$

if the spheres are from the same material. At zero external load ($F_L = 0$) one obtains a contact radius of

$$a_0 = \left(\frac{3\pi w_{adh} R^{*2}}{2E^*}\right)^{\frac{1}{3}} \tag{2.49}$$

which differs from the equilibrium contact radius in the JKR theory (Equation 2.41). Since adhesive forces outside the contact are considered but not the caused deformations, the DMT model is valid for hard particles with small sphere radii and more long-ranged forces.
Tabor in 1977 was the first who tried to solve the apparent contradiction between JKR

and DMT model quantitatively and to find a transition between the two theories [60]. He defined the Tabor-parameter μ_T as the ratio between the neck height at pull-off and the typical range of the surface forces, which was set equal to the equilibrium atomic distance:

$$\mu_T = \left(\frac{w_{adh}^2 R^*}{E^{*2} D_0^3} \right)^{1/3} \tag{2.50}$$

For values $\mu_T \ll 1$ the DMT theory is applicable whereas for values $\mu_T \gg 1$ JKR theory is valid.

2.4.4 Maugis Model

In 1992 Maugis [61] improved Tabor's idea and verified that JKR and DMT model are the two limiting cases of a more general contact theory. His Maugis-Dugdale model is the most accurate theory and applies to the entire range of materials, from large soft materials with high surface energies to small hard materials with low surface energies. Using a Dugdale potential to describe the interaction between the contacting spheres (Figure 2.11), Maugis was able to derive several analytical equations for the JKR-DMT transition.

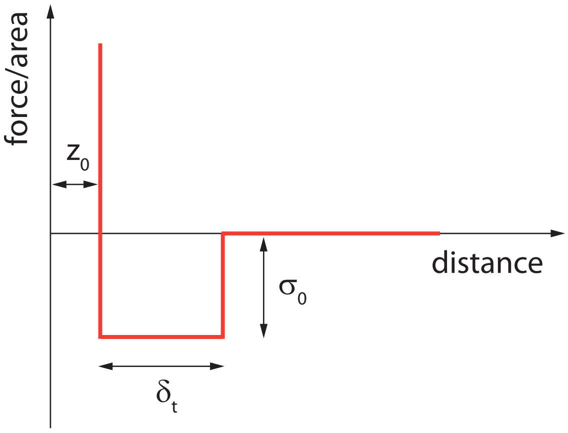

Figure 2.11: Dugdale potential describing the interaction between two spheres in the Maugis model. A constant adhesive stress σ_0 acts over the distance δ_t starting from the equilibrium atomic distance z_0.

He defined the Maugis parameter μ_M, which is almost identical to the Tabor parameter μ_T, as

$$\mu_M = \frac{2\sigma_0}{(16\pi w_{adh} E^{*2}/9R^*)^{1/3}} = 1.1570 \cdot \mu_T \tag{2.51}$$

where σ_0 is the minimum adhesive stress of a Lennard-Jones potential. The increase of μ_M from zero to infinity describes a continuous transition from the DMT to the JKR limit: for soft spheres with large radii μ_M becomes large, corresponding to the JKR limit, while for hard spheres with small radii μ_M becomes small, corresponding to the DMT limit. Maugis could demonstrate that the JKR model is a good approximation for $\mu_M > 3$ whereas the DMT model is a good approximation for $\mu_M < 0.1$, better $\mu_M \to 0$. Values in between correspond to the transition regime between both models.

2.4.5 Rabinovich Model

Experimentally determined adhesion forces of spherical particles may differ to a great extent from those predicted with the so far introduced contact models. One of the main reasons beside surface heterogeneities is the nanoscale roughness of real surfaces.

All above discussed models assume perfectly smooth surfaces of the contacting bodies. However, in reality all surfaces posses a finite surface roughness which significantly influences the adhesion force of two contacting bodies. Due to a decrease in the real contact area and an increase in the distance between the surfaces this nanoscale roughness reduces adhesion substantially. Much effort has been done to model roughness and describe real surfaces more accurately, for example by Greenwood and Williamson [62], Fuller and Tabor [63] or Iida et al. [64].

One of the most common models is the one of Rumpf [65], who approximates the real surface profile by spherical aspertities. His approach is based on the interaction between a single hemispherical asperity with radius r centered at a plane surface and a much larger spherical particle with radius R_P (Figure 2.12a).

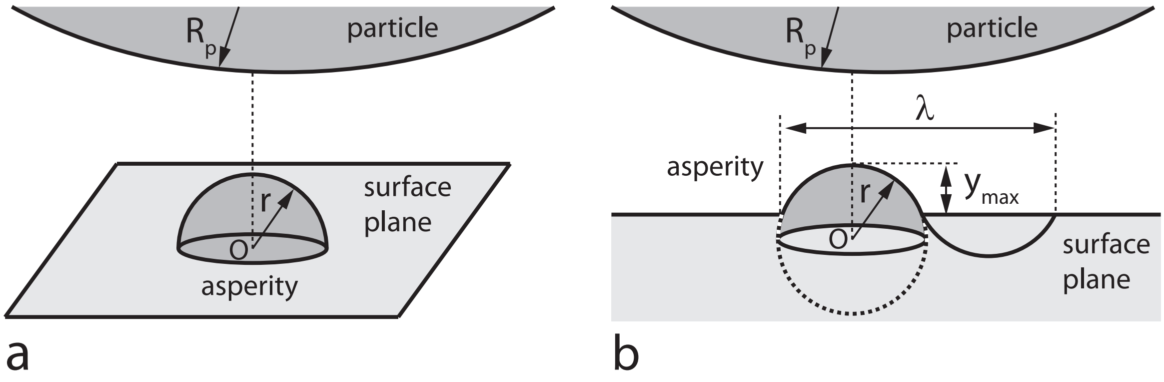

Figure 2.12: Schematic of the geometric model to describe the interaction of a sphere with a rough surface suggested by Rumpf (a) compared to the model by Rabinovich (b).

Rumpf derived an expression for the van der Waals interaction, consisting of a first term that represents the force between the particle in contact with the asperity and a second "noncontact" term describing the force between the particle and the flat surface separated by the asperity radius:

$$F_{adh} = -\frac{A_H}{6D_0^2}\left[\frac{rR_P}{r+R_P} + \frac{R_P}{(1+r/D_0)^2}\right] \tag{2.52}$$

Here A_H is the Hamaker constant and D_0 the distance of closest approach between surfaces (approximately 0.17 nm). However, the model by Rumpf does not accurately describe roughness in the nanoscale regime, since the center of the asperity is required to be at the surface. For real systems, especially with low surface roughness, this assumption is too simplistic. For vanishing roughness the asperity radius should approach infinity and result in a flat surface. If the asperity should be modeled as a sphere, this cannot be achieved when the center of the sphere is located on the surface plane. Moreover, the radius of an asperity r is hardly a measurable parameter, which is a crucial disadvantage when comparing experimentally determined adhesion forces with the theory.

In 2000 Rabinovich [17, 66] introduced a more general model based on the two measureable parameters root mean square roughness r_{rms} and average lateral distance λ between asperities. Both can be determined experimentally. With his new theory, Rabinovich was able to better explain his experimentally measured adhesion forces with the atomic force microscope (AFM). In his approach, the center of the spherical asperity is located below the surface plane (Figure 2.12b), implying that the maximum peak height y_{max} is not equal to the asperity radius r. Furthermore, not only the height of the asperity but also its breadth is considered. He obtained for the van der Waals force between an adhering particle and a surface with nanoscale roughness

$$F_{adh} = -\frac{A_H R_P}{6D_0^2}\left[\frac{1}{1+\frac{32cR_P r_{rms}}{\lambda^2}} + \frac{1}{(1+\frac{cr_{rms}}{D_0})^2}\right] \tag{2.53}$$

with the proportionality factor $c = 1.817$ and the two measurable parameters root mean square roughness r_{rms} and the average lateral distance between asperities λ (with $\lambda \gg r_{rms}$). The root mean square roughness for N data points is defined as the root mean square average of the height deviations z_i from the average surface plane

$$r_{rms} = \sqrt{\frac{1}{N}\sum_{i=1}^{N} z_i^2} \tag{2.54}$$

The value of r_{rms} depends on the length scale over which it is calculated.
The first term of Equation 2.53 corresponds to the contact interaction between particle and asperity while the second term describes the "noncontact" interaction between sphere and the average surface plane. It is valid for a roughness range of $0.1 \ll r_{rms} \ll 20\,\mathrm{nm}$.
When comparing experimentally determined adhesion forces with theory, one should keep in mind that the Rabinovich approach only takes van der Waals forces into account. All other surface forces like capillary forces, that may have a strong influence, as well as elastic deformation of the material are not considered. Therefore the Rabinovich model might underestimate adhesion.

3 Established Techniques to measure Adhesion Forces

Different techniques have been developed to measure adhesion forces of powder particles in air. In this chapter, the most popular and well established tools are presented: the colloidal probe technique based on the atomic force microscope (AFM) and the centrifuge method.

3.1 Atomic Force Microscope and Colloidal Probe Technique

3.1.1 The Atomic Force Microscope

The atomic force microscope (AFM) was invented by Binning in 1986 to image topographies of surfaces [67]. However, today the AFM can be used to study a great variety of surface properties, not only topography but also mechanical, viscoelastic and thermal properties as well as surface and friction forces.

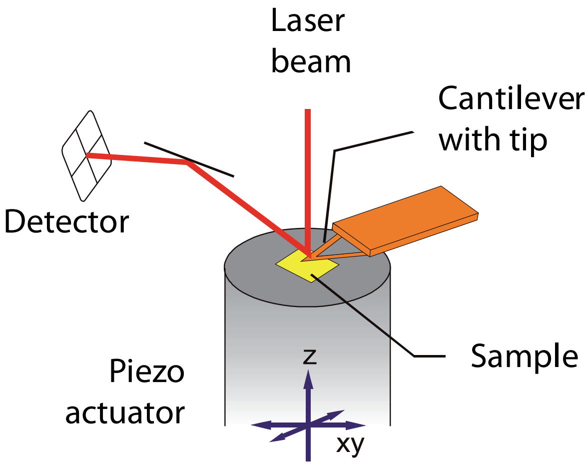

Figure 3.1: Schematic of an atomic force microscope (AFM): the cantilever is brought into contact with the sample, its deflection due to the interaction with the sample surface is measured with a laser beam which is reflected from the cantilever backside onto a photodiode.

One important characteristic of the AFM, which makes it to one of the most prominent tools in surface science, is the high imaging resolution. Depending on the sample system, even atomic resolution is achievable.

In the AFM (Figure 3.1), a probe is brought into contact with the surface where it interacts with the surface atoms. Usually the probe consists of a microcantilever with a sharp tip made of silicon or silicon nitride, which typically has a tip radius of $5 - 50\,\mu\text{m}$. Interaction with the surface leads to a deflection of the cantilever which is detected by reflecting a laser beam from the cantilever backside onto a split-photodiode (optical lever technique). The lateral and vertical movement of the probe or the sample, respectively, can be controlled by piezo actuators.

3.1.2 Imaging with the Atomic Force Microscope: Contact and Tapping Mode

Topography images can be obtained by raster-scanning the tip over the surface, either by moving the tip over the fixed sample or by moving the sample under the fixed probe. Scanning can be performed in static mode (*contact mode*) or in dynamic mode (*tapping mode*).

Contact Mode

In *contact mode*, the tip raster-scans the surface line by line staying in direct physical contact with the sample. Here, the force between tip and sample is kept constant. The user defines a preset cantilever deflection set-point, corresponding to a well defined force between tip and sample. While scanning, changes in the sample topography cause a cantilever deflection, which is detected with the photodiode and compared to the set-point value in a direct current feedback amplifier. The feedback amplifier tries to maintain the initial deflection set-point by applying a voltage to the z-piezo-scanner which results in a movement in z-direction. Recording this z-movement of the piezo leads to a topography image of the sample surface.

However, imaging in contact mode has several disadvantages. The lateral movement of the cantilever induces shear forces between tip and surface that can modify or even damage the sample. For soft samples, in particular, the tip also indents the surface easily which can cause surface modification and tip contamination.

Tapping Mode

The *tapping* or *intermittent contact mode* is an alternative to contact mode measurements. Here, the cantilever is excited to oscillate at or close to its resonance frequency by an additional piezo actuator. The tip motion can be described by a nonlinear, second order differential equation [68]:

$$m\ddot{z} + kz + \gamma\dot{z} = F_{ts} + F_0 \cos(\omega t) \tag{3.1}$$

where z is the position, F_0 and ω are the amplitude and the frequency of the driving force, and k and γ are the spring constant and the damping factor of the cantilever, respectively. F_{ts} contains the tip-surface interaction.

Assuming no interaction forces between tip and sample ($F_{ts} = 0$), the cantilever behaves like a damped forced harmonic oscillator and Equation 3.1 can be written as

$$\ddot{z} + \omega_0^2 z + \frac{\omega_0}{Q}\dot{z} = \frac{F_0}{m}\cos(\omega t) \tag{3.2}$$

where $\omega_0 = \sqrt{k/m}$ is the free cantilever resonance frequency and $Q = (\omega_0 m)/\gamma$ is the quality factor with the mass m. A solution of Equation 3.2 is

$$z(t) = A(\omega)\cos(\omega t + \phi) + z_0 \tag{3.3}$$

where the amplitude $A(\omega)$ and the phase shift $\phi(\omega)$ are given by

$$A(\omega) = \frac{F_0/m}{\sqrt{(\omega_0^2 - \omega^2)^2 + (\omega_0^2\omega^2)/Q^2}} \tag{3.4}$$

$$\phi(\omega) = \arctan\left(\frac{\omega\omega_0/Q}{\omega_0^2 - \omega^2}\right) \tag{3.5}$$

Approaching and slightly touching the surface leads to a change of the cantilever resonance frequency and therefore to a reduction of the oscillation amplitude.

Topography images can be obtained by two different techniques: either by *amplitude modulation* or by *frequency modulation*. In the amplitude modulation mode, the cantilever is excited at a fixed frequency while the change in amplitude is measured and compared with the user defined amplitude set-point. The feedback loop system tries to keep the amplitude of the cantilever constant by applying a voltage to the z-piezo-scanner which results in a change of the cantilever height. In the frequency modulation mode the cantilever oscillates with a fixed amplitude while the feedback loop maintains the frequency shift constant.

3.1.3 The Colloidal Probe Technique

The AFM can also be used to record force-versus-distance curves by moving the sample under the fixed cantilever up and down (or vice versa) measuring the deflection. By considering the cantilever as a spring and applying Hooke's law, the force between tip and surface can be calculated. Data from these curves can be used to study material properties, like elasticity, as well as all kinds of surface forces, even between single molecules.
The colloidal probe technique, using an AFM, is one of the most important established techniques to measure adhesion forces between particles or between particles and surfaces. It was first applied by Ducker [69, 70] and Butt [71] independently.
Here, instead of using a common cantilever with tip, a single micron sized particle is manually attached to a tipless cantilever to measure force-distance curves [27]. The well defined shape of the particle, in contrast to the AFM tip, makes it possible to compare measured forces with predictions from theoretical contact models. In principle force-distance measurements can be conducted in different environments like air, vacuum or in liquids. However, since this thesis deals with adhesion of particles in air, in the following, the focus lies on force measurements in air.
Usually probe preparation is performed by gluing a single particle to a tipless cantilever. The most common way to do this is by using a micromanipulator under the control of an optical microscope. This limits the minimum particle size to about 1 µm. In special cases also sintering of the particles to the cantilever is possible.

Principle of Force Measurement

In order to measure force-distance curves, the cantilever stays fixed while the sample is free to move vertically by control of a z-piezo translator (or the sample stays fixed while the cantilever is free to move). In this configuration, many approach-retract cycles are performed: the sample approaches the cantilever until contact and is afterwards retracted while the deflection is measured by reflecting a laser beam at the cantilever backside onto a position sensitive photodiode.
The measured raw signal is the detector signal in volts ΔV, which can be converted into the cantilever deflection, versus the piezo position Δz. Figure 3.2 gives a detailed overview, how the signal is obtained [33]. In the first step (1) the sample surface approaches the colloidal probe, but since it is still far away, no forces act between particle and surface. Therefore the cantilever will not deflect. Further approaching (2) causes a bending of the cantilever due to attractive interaction forces, which leads to a jump-into-contact if the gradient of the surface forces exceeds the cantilever spring constant. From this moment on, if no deformation of particle or surface occurs, cantilever and sample are in contact and move in parallel (3), which causes a linear increase of the deflection signal for further approach. This linear region is called the *constant compliance region.* Here, the load can be varied. Retracting the sample (4) leads to a decrease of

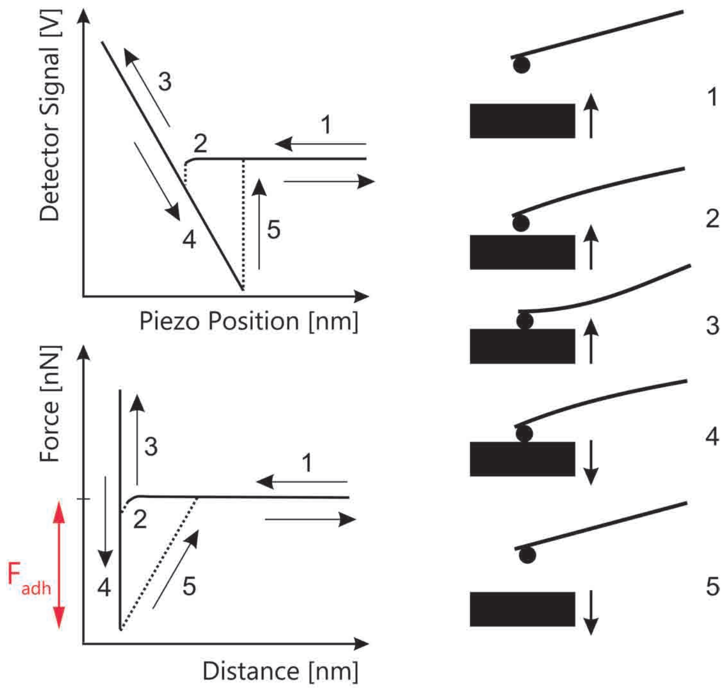

Figure 3.2: Illustration of force-versus-distance measurements with the colloidal probe technique [33]: Steps 1-5 represent an approach-retract cycle of the sample and the cantilever. The upper curve shows the measured raw signal, detector signal in V versus piezo position in nm. The lower curve is the force-versus-distance curve, which is obtained after a calibration. From this, the adhesion force F_{adh} can be determined.

the deflection signal, however, due to surface forces the colloidal probe adheres to the surface. When the bending force of the cantilever exceeds the adhesion, the probe will jump off the surface back to its initial position (5).

To obtain a force-versus-distance curve (Figure 3.2, lower curve), the raw detector signal in volts has to be converted into a force and the piezo displacement has to be converted in a separation distance between probe and surface.

At first, a line is fitted to the zero force region (region 1 in Figure 3.2), which gives an offset that should be subtracted from the deflection data. To obtain the force, the cantilever deflection is calculated by multiplying the detector signal ΔV with a conversion factor, the deflection sensitivity S. Afterwards the deflection is multiplied with the cantilever spring constant k, which is determined experimentally before or after the measurement:

$$F[\mathrm{N}] = \mathrm{S}[\frac{\mathrm{nm}}{\mathrm{V}}] \cdot \Delta\mathrm{V}[\mathrm{V}] \cdot \mathrm{k}[\frac{\mathrm{N}}{\mathrm{m}}] \tag{3.6}$$

The sensitivity S of the cantilever can be obtained from a linear fit of the constant compliance region, since in this part, due to the parallel movement, the deflection of the cantilever equals the piezo displacement. Therefore, the inverse slope is the conversion factor between detector signal in V and deflection in nm.

The tip-sample separation is calculated by adding the cantilever deflection to the piezo position.

From the resulting force-versus-distance curve, the adhesion force F_{adh} between the colloidal probe and the surface can be determined, which is the minimum of the curve (Figure 3.2, lower curve).

Thermal Noise Method: Spring Constant Calibration

For the determination of the force from the measured deflection, the spring constant k of the cantilever has to be known. It is possible to calculate k from the geometric dimensions and elastic properties of the cantilever, however, since thickness and elastic modulus of cantilevers are difficult to determine, an experimental calibration is more accurate.

A common method to measure the spring constant is the *thermal noise method*, which is implemented in many commercial AFMs. It was introduced by Hutter and Bechhoefer [72] who modeled the cantilever as a harmonic oscillator. They related its Brownian motion of the first oscillation mode to its thermal energy by applying the equipartition theorem:

$$\frac{1}{2}k\langle Z_c^2\rangle = \frac{1}{2}k_B T \tag{3.7}$$

with the mean square displacement of the cantilever $\langle Z_c^2\rangle$, the Boltzmann constant k_B and the temperature T. Thus, by measuring $\langle Z_c^2\rangle$, the spring constant of the cantilever k can be determined as

$$k = \frac{k_B T}{\langle Z_c^2\rangle} \tag{3.8}$$

The mean square cantilever displacement $\langle Z_c^2\rangle$ is obtained by carrying out a power spectral density analysis of the cantilever oscillation and afterwards integrating the area under the peak of the first oscillation mode.

Later Equation 3.8 was corrected, taking also the tilt of the cantilever into account [73]. The corrected equation for a rectangular cantilever is [74]

$$k = 0.817 \cdot \frac{k_B T}{\langle Z_c^{*2}\rangle} \cos^2\theta \tag{3.9}$$

where $\langle Z_c^{*2}\rangle$ is the displacement of the cantilever measured by optical detection and θ is the tilt angle of the cantilever.

3.2 Centrifuge Method

Another popular and well established technique is the centrifuge method, based on the centrifugal detachment of particles from a surface due to their inertia. This method, which was initially described by Boehme and Krupp [14, 29], has been used to measure particle adhesion since the 1960s. The performed experiments contributed substantially to our knowledge about the behavior of powders. A wide range of different powders has been studied, especially powders for pharmaceutical applications [30–32, 75] but also for food industry or electrophotography processes [76], for instance.
Particles are dispersed from the powder and deposited on a flat substrate, which is mounted in an ultracentrifuge (Figure 3.3). The sample (mostly placed into a special centrifuge cell) is attached to the rotor, which is then spinning in an evacuated chamber in order to avoid gaseous friction.

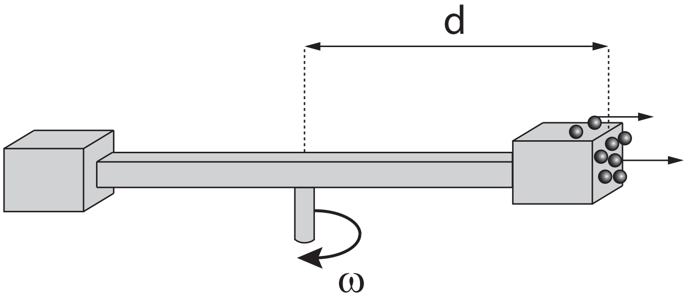

Figure 3.3: Schematic illustration of the centrifuge method: particles are detached from a rotating surface due to their inertia, which allows to determine the adhesion force.

The rotation causes a centrifugal force acting on the particles

$$F_{cen} = m\omega^2 d \tag{3.10}$$

with the particle mass m, the angular speed ω of the rotor and the distance d between the sample and the rotor center. F_{cen} can be applied either in compression direction (press-on), when the sample is put with the side of the particles surface facing the center of the centrifuge, or in detachment direction (spin-off), where the sample is put in the opposite direction [77]. The first configuration can be used to achieve a uniform particle deposition on the surface prior to the detachment tests, whereas the second configuration (Figure 3.3) is used to measure adhesion.
The surface is rotated at sequentially higher speeds in a series of centrifuging steps. When the centrifugal force exceeds the adhesion force of a particle at a critical speed, it

will detach from the surface caused by its inertia. At detachment, the adhesion force is equal in magnitude but with opposing sign to the applied centrifugal force:

$$F_{adh} = -F_{cen} \tag{3.11}$$

After each rotation step, the sample is removed from the centrifuge in order to determine the number of particles remaining on the surface, which is usually done by image analysis using an optical microscope. From the images, also the particle diameter (or the mean diameter in case of irregularly shaped particles) can be obtained, which allows to calculate the particle mass m.

With the centrifuge technique friction forces can be studied as well, by mounting the surface with the particles horizontally (Figure 3.3).

In contrast to the colloidal probe technique, where single particles are investigated, the centrifuge method allows to measure adhesion of many individual particles at different surface locations with a single series of runs. This results in a good statistical evaluation of the data.

However, the centrifuge method is an effortful and time-consuming technique. Especially for high rotation speeds, a considerable time is needed to reach the desired angular speed. For good statistics, between 10 and 20 centrifuging steps are required and after each, the sample has to be dismounted from the system for image analysis. Considering additionally the evacuation and spin up/down times for each acceleration value, this leads to measuring times of several hours. Moreover, the applicability of the method is limited by the maximum possible rotational speed of the available ultracentrifuges, which depends on the stability of the rotor material. This restricts adhesion measurements using the centrifuge method to particles larger than a few microns [33].

Furthermore, adhesion measurements under different environmental conditions are difficult to realize, since relative humidity and temperature can hardly be controlled during the experiment [31].

3.3 Overview: Advantages and Drawbacks of the Established Techniques

Both of the presented established techniques to measure particle adhesion forces offer several advantages but also some drawbacks. They are collected here as an overview:

	colloidal probe technique	**centrifuge method**
advantages	• the same particle can be further examined after the measurement • high flexibility of samples (measurements possible in liquids or different vapors...)	• many particles can be characterized in a single series of runs → statistical evaluation • particles are randomly oriented like in real powders
drawbacks	• high preparation effort: single particle experiments → low adhesion statistics • orientations of the particles are pre-defined (cannot adjust freely)	• limited rotor stability • time consuming • difficult to control environmental conditions

Summarized, the established techniques are strong tools for adhesion studies and they complement each other. However, they are experimentally demanding, expensive and time consuming and consequently not usable for routine applications. This gives rise to the need for a more simple alternative method.

A promising alternative is the completely new developed technique presented in this thesis. Since it is less time consuming and offers a good statistical evaluation of the adhesion data, this new method has the potential to be used on a routine base, even for investigation of very fine and cohesive powders.

4 Elastic Waves in Solids

The new technique for measurement of particle adhesion, which is presented in this thesis, uses the Hopkinson bar principle based on the propagation of elastic waves in a long thin rod. Thus, in this chapter fundamentals of elastic wave motion in solids are introduced, as well as a brief historical outline of the Hopkinson and Kolsky bar.

4.1 Longitudinal Wave Propagation in long Rods

The Hopkinson bar is a long thin cylindrical rod made of metal with two free ends. Due to an external force pulse on one bar end, an elastic wave is excited, propagating through the bar, which causes high accelerations at the other free end. The device in this thesis generates the external force pulse by mechanical impact of a solid body, particularly by a bullet impact. The acceleration available at the bar's free end is used to detach particles from a surface.

In the following, an expression for the acceleration is derived. We consider a long, cylindrical rod with cross-section area A and density ρ (Figure 4.1) under a dynamically varying external stress field $\sigma(x,t)$ [78].

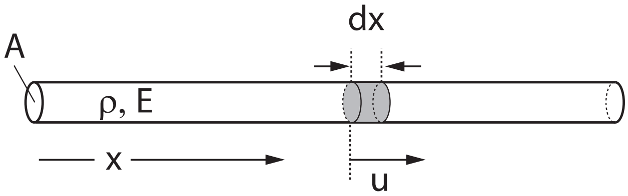

Figure 4.1: Long thin rod of density ρ, having a Young's modulus E and cross section area A. Here, u is the longitudinal displacement of the rod section dx in x-direction.

The stress field acting on the volume element Adx causes a change of the total momentum p of the mass points

$$\begin{aligned}\sigma(x,t)\cdot A &= \frac{\partial}{\partial t}p \\ &= \frac{\partial}{\partial t}\left(\rho A \frac{\partial u(x,t)}{\partial t} dx\right)\end{aligned} \tag{4.1}$$

assuming the absence of further external body forces. Here, $u(x,t)$ is the longitudinal displacement of the rod section. This leads to the 1-dimensional equation of motion in x-direction

$$\frac{\partial \sigma(x,t)}{\partial x} = \rho \frac{\partial^2 u(x,t)}{\partial t^2} \tag{4.2}$$

Presuming that the material behaves elastically, which means that Hooke's law $\sigma = E \cdot \varepsilon$ applies, and that the rod is homogeneous with location-independent Young's modulus E and density ρ, Equation 4.2 can be written as

$$E \cdot \frac{\partial^2 u(x,t)}{\partial x^2} = \rho \frac{\partial^2 u(x,t)}{\partial t^2} \tag{4.3}$$

with the axial strain $\varepsilon = \partial u / \partial x$. Equation 4.3 implies the additional assumption that plane cross-sections remain plane during the motion and that a uniform stress distribution exists. With the propagation velocity of a longitudinal wave in the rod

$$c_0 = \sqrt{\frac{E}{\rho}} \tag{4.4}$$

one obtains the equation of motion

$$\frac{\partial^2 u(x,t)}{\partial x^2} = \frac{1}{c_0^2} \frac{\partial^2 u(x,t)}{\partial t^2} \tag{4.5}$$

which is the homogeneous wave equation in one dimension. A general solution of Equation 4.5 is given by the d'Alembert approach

$$u(x,t) = f(x - c_0 t) + g(x + c_0 t) \tag{4.6}$$

which is the superposition of a longitudinal wave in x direction and a longitudinal wave in -x direction.

One should also take into account that a longitudinal pulse does not only cause an axial displacement but also lateral expansions and contractions according to the Poisson effect. However, the lateral motion is not further considered here.

If we consider a propagating longitudinal pulse $u(x,t) = f(x - c_0 t)$, the velocity of the mass points in the bar is

$$v(x,t) = \frac{\partial u(x,t)}{\partial t} = -c_0 f'(x - c_0 t) \tag{4.7}$$

With the stress

$$\sigma(x,t) = E \cdot \varepsilon = E \cdot \frac{\partial u(x,t)}{\partial x} = E \cdot f'(x - c_0 t) \tag{4.8}$$

we obtain

$$v(x,t) = -\frac{c_0}{E \cdot A} F(x,t) \tag{4.9}$$

depending on the force pulse $F(x,t)$. Therefore, at a fixed location in the bar the acceleration of the mass points is given by

$$a(t) = \frac{dv(t)}{dt} = \frac{c_0}{E \cdot A} \frac{dF(t)}{dt} \tag{4.10}$$

In this thesis, the acceleration at the bar's free end is of great significance. At the free end $x = x_e$, the propagating wave is reflected fulfilling the free end boundary condition $\partial u(x_e, t)/\partial x = 0$. Superposition of the incoming and the reflected wave causes a doubling of the displacement at the end of the bar. Thus, the acceleration is doubled as well, which leads to the final expression for the acceleration at the bar's free end [78]:

$$a(t) = 2 \cdot \frac{c_0}{E \cdot A} \frac{dF(t)}{dt} \tag{4.11}$$

depending on the properties of the bar, like Young's modulus E, wave propagation velocity $c_0 = \sqrt{E/\rho}$ and cross-section area A, as well as on the shape of the force pulse $dF(t)/dt$.

However, the stress is not doubled, but stays always zero at the free end. The stress pulse itself is reversed at the free end, meaning that a compression pulse is reflected as a tension pulse and vice versa. This *stress reversal* phenomenon is important for many practical applications. It was, for instance, one of the first methods to determine pulse characteristics [79] or dynamic tensile strengths of brittle materials [80].

To gain a deeper understanding of the wave motion in the Hopkinson bar, in the following the history of a stress pulse is considered.

We assume a finite rod with free end conditions, suspended by two light strings so that it is free to swing. The rod is subjected to an external pressure pulse, which is assumed to be a simple compressive step pulse

$$P(t) = \begin{cases} -P_0, & 0 < t < T \\ 0, & T < t \end{cases} \tag{4.12}$$

Due to the propagating stress wave

$$\sigma(x,t) = P(x - c_0 t) \tag{4.13}$$

a mass point in the bar at fixed location $x = x_0$ is brought from rest to the velocity

$$v(x_0,t) = -\frac{c_0}{E} P(x_0 - c_0 t) \tag{4.14}$$

which is constant during the pulse and will be zero after passage. The displacement of the mass point at $x = x_0$ increases according to

$$u(x_0,t) = \frac{c_0}{E} P_0 t \tag{4.15}$$

while the pulse passes. After the passage it remains constant. The compressive stress pulse travels the length of the bar l in time l/c_0 and is then reflected at the free end as a tensile pulse, travelling back to the other end. This cycle is repeated several times. Figure 4.2 shows the movement of three different mass points under a single passage of a step pulse [81]: one at the front side A, one at the bar midpoint B and one at the end face C. For better overview, the magnitudes of the displacements relative to the bar length are exaggerated.

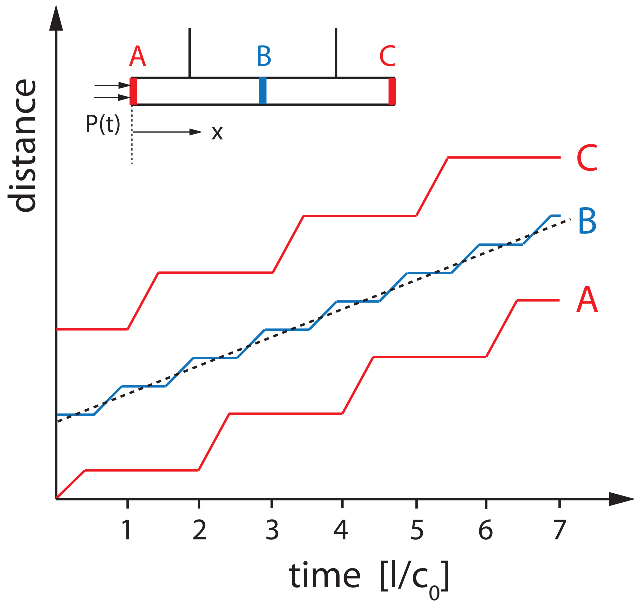

Figure 4.2: Discontinuous motion of three mass points A, B and C in a thin rod under a longitudinal pressure pulse [81]: A is located at the front side, B at the mid-point and C at the end face of the rod. The dashed line shows the average movement of B. The whole rod moves forward with a constant velocity, given by the slope of the dashed line.

The repeated reflections of the longitudinal pulse cause a discontinuous motion. Since a forward moving compression pulse is reflected as a backwards moving tension pulse, the direction of movement of a mass point remains the same. Thus, points A, B and C move to the right by several jerky movements. Due to velocity doubling at the free ends, the slopes in the displacement-time curve of point A and C (Figure 4.2) are doubled compared to point B. Moreover, point A and C move in intervals of $2l/c_0$, while point B is subjected to the pressure pulse twice as often. The dashed line corresponds to the average movement of B. However, with increasing time damping caused by internal friction and dispersive effects will occur. Dispersion means that high frequency parts of the pulse have a higher propagation speed than low frequency parts. Consequently, the length of the pulse increases continually with time. These effects lead to a rounding of the steps in Figure 4.2. The motion curve of B will approach the dashed line. Hence, the whole bar moves forward upon the pulse with a constant translational velocity, given by the slope of the dashed line. This velocity is the same as predicted from simple impulse-momentum considerations of rigid body dynamics [78].

Apart from longitudinal waves as discussed above, also transversal and torsional waves can propagate in a long thin rod. Their propagation velocity is given by

$$c_0 = \sqrt{\frac{G}{\rho}} \tag{4.16}$$

with the modulus of torsion G. In the same medium, usually, a longitudinal wave propagates faster than a transversal or torsional wave. However, since the acceleration at the free end of a Hopkinson bar is mainly generated by longitudinal waves, transversal and torsional waves are not considered further.

4.2 Impact of an elastic Sphere against a Rod

In the case of the Hopkinson bar used in this thesis the force pulse, which causes the acceleration at the free end, is generated by mechanical impact of a solid bullet.

A detailed theoretical description of this specific situation is quite complex, however, it can be approximated by the impact of an elastic sphere against a long rod (Figure 4.3). This problem was first solved theoretically by Eubanks in 1952 [82].

A collinear impact of a solid sphere against a rod is considered, taking the elastic deformation of the sphere and the rod into account but neglecting wave propagation within the sphere.

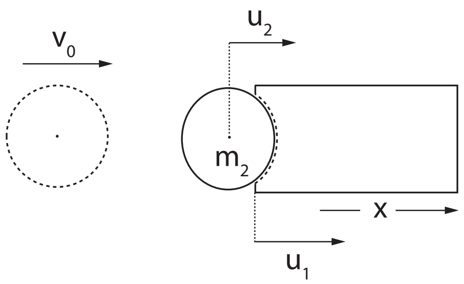

Figure 4.3: Impact of an elastic sphere with mass m_2 and initial velocity v_0 against a long thin rod.

With impulse-momentum considerations [78] one obtains

$$m_2 v_0 = \int_0^t F(\tau) d\tau + m_2 \dot{u}_2 \tag{4.17}$$

where u_1 is the rod displacement, u_2 is the displacement of the sphere center, m_2 is the mass of the sphere and F is the contact force on the rod, which is according to Equation 4.8 given by

$$F(t) = -AE \cdot f'(c_0 t) \tag{4.18}$$

The negative sign corresponds to a compressive stress. The motion of the rod contact surface is the displacement $u_1(0,t)$ plus the local deformation β_1, whereas the motion of the sphere is given by the forward movement of its center $u_2(t)$ minus the local compression β_2. During the impact, the rod surface and the sphere surface are in contact, therefore we obtain

$$\begin{aligned} & u_1(0,t) + \beta_1 = u_2(t) - \beta_2 \\ \Rightarrow \quad & u_2(t) - u_1(0,t) = \beta_1 + \beta_2 = \delta \end{aligned} \tag{4.19}$$

where δ is the deformation as in the Hertz contact model (chapter 2.4.1). The equation of motion for the deformation $\delta(t)$ can be written as

$$\ddot{\delta} - \frac{c_0}{EA} \dot{F}(t) + \frac{1}{m_2} F(t) = 0 \tag{4.20}$$

According to Hertz theory the relation between contact force and deformation is given by

$$F \propto \delta^{3/2} \tag{4.21}$$

where the proportionality constant depends on the elastic and geometric properties of the contacting bodies (Equation 2.36).

In order to obtain information about the shape of the resulting stress pulse $\sigma(t)$ that propagates through the bar after impact of the sphere, the complex non-linear equation of motion (Equation 4.20) has to be solved numerically for each specific impact situation. The initial conditions are

$$\begin{aligned} \delta(0) &= 0, \\ \dot{\delta}(0) &= v_0 \end{aligned} \tag{4.22}$$

The shape of $\sigma(t)$ depends on a large number of parameters: the Young's modulus and Poisson ratio E_1, ν_1 and E_2, ν_2 of the rod and the sphere, respectively, the cross section area A of the rod, the mass m_2 and radius R of the sphere, the longitudinal wave propagation velocity c_0 in the rod and the impact velocity v_0 of the sphere. Thus, for a given sphere-bar system, the resulting stress pulse is dependent on the impact velocity. By varying the impact velocity of the sphere v_0, the shape of the generated stress pulse $\sigma(t)$ in the bar can be controlled. The force is directly related to the stress via $F(t) = A\sigma(t)$. This means that the acceleration $a(t)$ at a bar's free end, which depends on the shape of the force pulse (Equation 4.11), can be controlled by changing the impact speed of the sphere.

The Hopkinson bar device, which was employed in this thesis, makes use of this effect: increasing the impact velocity of the bullet leads to increasing velocity and acceleration at the bar's end. In this special system, only the height of the pulse increases, while the pulse width and the principle shape remain nearly constant with increasing impact speed.

4.3 Hopkinson and Kolsky Bar

The first published technical application of the Hopkinson bar principle was in 1914 by Hopkinson [79]. He used a long thin steel rod to measure the pressure arising in detonations of high explosives and produced by a bullet impact.

The rod was hung up horizontally being able to swing freely. Then a pressure pulse was generated by an impacting rifle bullet or detonating gun cotton near the rod end. This pulse traveled through the rod (diameter: about 25 mm, length: $1 - 1.3\,\mathrm{m}$) and detached a test piece at the rod end, which had been held on by magnetic attraction (Figure 4.4a). By measuring the momentum of the test piece with a ballistic pendulum, Hopkinson was able to obtain information about the integral of the pressure-time curve of the shock pulse. However, calculating the pressure from the momentum of a piece that flies off a rod end implies several assumptions. It is supposed that the pressure wave transmitted into the rod represents exactly the pressure applied at the end. Furthermore, one has to assume that the pressure pulse does not change its shape when propagating through the rod and the joint between rod and test piece. Besides, the pulse should be perfectly reflected at the end. Due to the limited technical capabilities in this time, the accuracy of these measurements was relatively low. Another disadvantage is, that by measuring the momentum of the test piece, the integral but not the exact shape of the pressure-time curve can be obtained. Since a magnetic attraction exists between the detachable end-piece and the rod, the method only gives reliable results for very high pressures. However, this *fly away method* is in principle still used today for calibration of accelerometers [83].

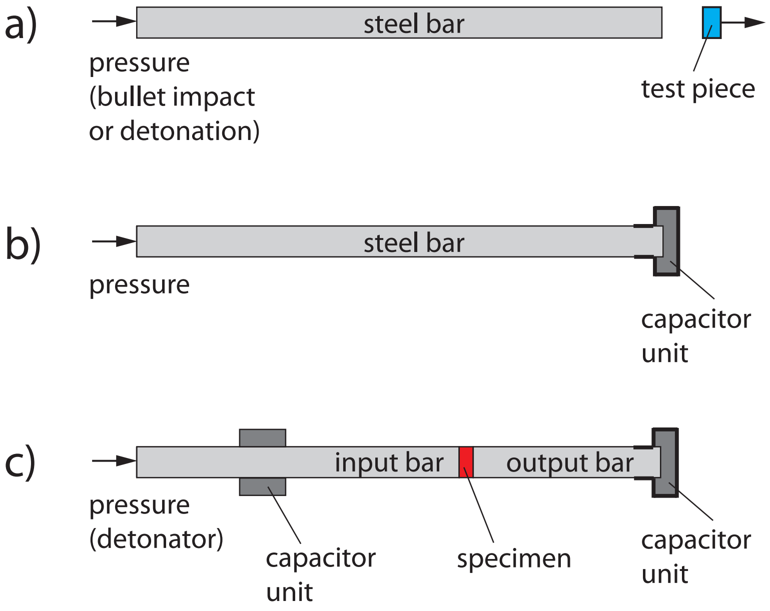

Figure 4.4: (a) Illustration of the Hopkinson bar system to measure pressures arising in detonations or produced by bullet impact with the *fly away method* developed by Hopkinson [79].(b) The system was modified and improved by Davies [84] who measured the bar displacement with a capacitor unit. (c) Split Hopkinson bar (Kolsky bar) for material characterization studies developed by Kolsky [85]: the specimen is mounted between two bars, the input and the output bar (c).

In 1948 Davies carried out a detailed study of the method introduced by Hopkinson and further developed the technique [84]. He was able to improve the accuracy of the pressure measurement by using a capacitor unit to electrically determine the displacement of the bar end (Figure 4.4b). This modified system enabled to measure much smaller pressures and to determine the shape of the pressure pulse.
Kolsky in 1949 was the first who used the Hopkinson bar for material characterization purposes [85]. He was interested in the mechanical behavior of different materials at high strain rates. Therefore he modified the set-up from Davies to conduct stress-strain

measurements by adding a second bar to the system (Figure 4.4c). The specimens, in the form of thin discs, were mounted in between the two freely suspended steel bars (input and output bar). Then a detonator was fired electrically at the end of the input bar, generating the pressure pulse. This pulse propagated down the input bar to the specimen, where a transmitted pulse travelled through the output bar and a reflected pulse was sent back to the input bar. With a parallel-plate capacitor unit the displacement at the free end of the output bar was measured, from which the stress-time curve for the specimen could be calculated. An additional cylindrical capacitor unit was mounted around the input bar to measure the amplitude of the pressure pulse arriving at the specimen. From the displacement-time relation of the initial pulse (without specimen) and the transmitted pulse (with specimen) the strain-time curve for the specimen was obtained. Thus, it was possible to derive the stress-strain relation for different materials like rubbers, plastics and metals.

The apparatus developed by Kolsky, which is called *split Hopkinson bar* or *Kolsky bar*, is still used today for material characterization and stress tests. However, instead of capacitor units mostly strain gauges are used, which are attached to the bar and measure the bar strains. From the measured bar strains the stress-strain relation of a test object can be derived.

Today, the two main applications of the Hopkinson bar are material characterization at high strain rates, where a single bar or a Kolsky bar are used [86, 87], and calibration of acceleration sensors [88, 89]. Due to the acceleration doubling at the free end (Equation 4.11), in principle very high accelerations up to several hundreds of thousands g are achievable with a Hopkinson bar ($g = 9.81\,\mathrm{m/s^2}$, standard acceleration of free fall). By varying the force pulse, the acceleration amplitude and pulse width at the bar's end can be controlled.

One example for a calibration device is the shock acceleration exciter with three Hopkinson bars, developed at the Physikalisch-Technische Bundesanstalt in Braunschweig, Germany [90]. The system consists of three bars arranged in parallel, which are each 4 m long. They differ in their material (steel or titanium) and diameters.

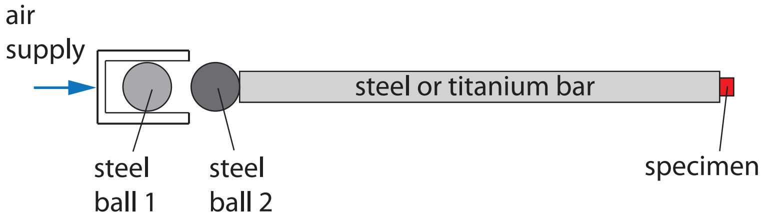

Figure 4.5: Principle of the shock acceleration exciter for calibration of accelerometers developed at the Physikalisch-Technische Bundesanstalt in Braunschweig, Germany.

In this device the shock wave is excited by shooting a steel ball pneumatically onto a second identical steel ball, which is kept in contact with the bar's end by vacuum (Figure 4.5). The collision causes a shock pulse propagating through the bar, which is reflected at the other bar's end where the accelerometer to be calibrated is attached to. The reference acceleration is measured interferometrically at the bar's end. By varying the driving pressure of the air supply the amplitude of the acceleration can be changed. Since the air supply is electronically controlled, this procedure is automated. The pulse width can be changed by using pairs of steel balls with different diameters. With this device, a great variety of different peak amplitudes ($100 - 10\,000\,g$) and pulse duration times are possible.

The company SPEKTRA GmbH in Dresden developed a Hopkinson shock excitation system for calibration purposes using a titanium bar and an air gun [91, 92]. Here, the shock pulse generation is achieved by shooting a projectile pneumatically against one bar's end. The acceleration available at the other free end can be controlled by the impact speed of the projectile. This can be varied by changing the distance between projectile starting point and bar end, thus the distance over which the projectile is accelerated. This procedure is automated. The reference acceleration is either measured interferometrically at the bar's end or by using strain gauges, which are laterally attached to the bar. The standard Hopkinson shock excitation devices produced by SPEKTRA provide defined accelerations up to $200\,000\,g$ [93]. The Hopkinson bar system, which was used in this thesis, is a custom-made device fabricated by SPEKTRA (details in chapter 5). The basic principle is the same as for the commercial devices, however, much higher acceleration amplitudes (up to $500\,000\,g$) are achievable at the bar's end. These high accelerations are used to detach particles from a surface in order to determine their adhesion forces.

5 The Hopkinson Bar Method to measure Particle Adhesion

Since the established techniques to measure particle adhesion, the colloidal probe and the centrifuge method, are experimentally demanding and time consuming, an alternative technique is needed that has the potential to be used on a routine base.
In this chapter the new method, which was developed in this thesis, is presented. The development of the basic principle, the technical conversion and the procedure to measure adhesion of particles are discussed here.

5.1 Development of the new Method

5.1.1 Requirements of the System

In order to develop such a new technique, at first one has to consider the requirements the system has to fulfill.
With the new apparatus it should be possible to measure adhesion forces between individual particles and a surface, including very fine and cohesive powders with particle diameters of $1 - 5\,\mu\mathrm{m}$. This size range, in particular, is important for many industrial applications. Additionally, the new method should offer a good statistical evaluation and therefore enable measurements of many individual particles simultaneously.
The basic idea is to deposit an ensemble of single particles onto a flat surface, which is then excited mechanically, and to observe particle detachment due to their inertia. The surface causes an inertial (detachment) force acting on each particle. When this detachment force exceeds the adhesion of a particle, it will detach from the surface. Thus in the moment of detachment, the adhesion force equals the inertial force provided by the surface:

$$F_{adh} = F_{detach} = \rho \frac{4}{3} \pi R_P^3 \cdot a \tag{5.1}$$

where ρ is the particle density, R_P is the particle radius and a is the acceleration of the surface. By increasing the acceleration of the surface and recording particle detachment events with an optical system, the adhesion force of the particles can be determined from the measured radii and acceleration.

However, estimations according to the JKR theory (Equation 2.44) and measured adhesion forces with the colloidal probe technique predict a needed acceleration of at least $300\,000\,g$ for detachment, depending on particle diameter and density ($g = 9.81\,\mathrm{m/s^2}$, standard acceleration of free fall). Thus, to achieve detachment of particles in a diameter range of $1-5\,\mu\mathrm{m}$ and determine their adhesion, a technical system has to be found that can provide well-defined accelerations in the order of $300\,000 - 500\,000\,g$. Accelerations of this magnitude are close to the fundamental limit of mechanically possible accelerations, since the yielding point of the material is nearly reached. Higher values can cause material failure.

5.1.2 Possible Techniques

An existing alternative technique to the established methods for particle adhesion measurements is the *vibration method*, first described by Derjaguin and Zimon [94] and further developed by Hein and Ripperger [95, 96]. It is based on particle detachment from a vertically oscillating surface. Derjaguin and Zimon used a dynamic speaker to generate the oscillation whereas Hein and Ripperger use a piezoelectric actuator.

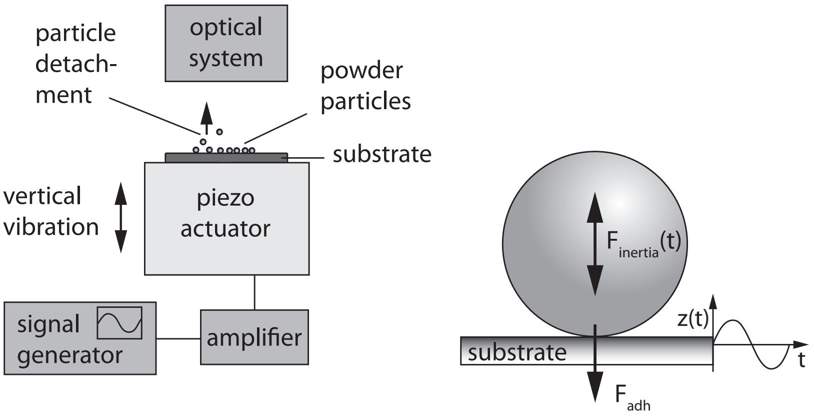

Figure 5.1: Left: Measuring principle of the vibration method, according to [95]: particles are detached from an oscillating substrate due to their inertia. This allows to determine their adhesion force. Right: Forces acting on a particle that sits on a sinusoidally vibrating surface. However, the piezo material limits the applicability of the vibration method: adhesion of particles smaller than about $5\,\mu\mathrm{m}$ cannot be measured.

In the set-up of Hein and Ripperger, single particles are placed on a substrate, which is attached to a piezo transducer that generates a vertical sinusoidal vibration by control of a waveform generator and an amplifier (Figure 5.1, left). The vibration causes alternating inertial forces on the particles: a detachment force at the upper reversal point and a compressive contact force at the bottom reversal point of the oscillating substrate

(Figure 5.1, right). In order to measure normal adhesion forces, the acceleration of the surface is increased continuously by increasing the vibration amplitude at fixed piezo frequency. By continuously recording particle detachment events with an optical microscope system and measuring the acting acceleration on the surface with a laser scanning vibrometer [95] the adhesion force of the detached particles can be determined according to Equation 5.1. In order to remove already detached particles from the surface and avoid reattachment, Hein and Ripperger use a flow channel with a horizontal laminar air flow which the sample is exposed to.

With the vibration method, just like with the centrifuge method, it is possible to measure adhesion forces of many particles at different substrate locations simultaneously, resulting in a good statistical evaluation of the data, compared to the single particle measurements with the colloidal probe technique. However, in contrast to the colloidal probe technique and the centrifuge method, where a uniform and incremental detachment force acts on the particles, the vibration method causes sinusoidal alternating stresses on the particles, which might have an influence on the adhesion force, depending on the investigated system.

The applicability of the vibration method is limited by the maximum piezo amplitude which determines the maximum possible detachment force. The maximum amplitude is limited by the piezo material, that easily breaks when it is subjected to high strains. Commercial piezo actuators, like those used by Hein and Ripperger, can provide a maximum acceleration in the range of $10\,000\,g$, which restricts the size of investigatable particles to $> 5\,\mu\mathrm{m}$ in diameter.

However, even with a custom-made preloaded piezo transducer, accelerations higher than $100\,000\,g$ are not achievable, since higher piezo amplitudes cause material breakage. Therefore the vibration method cannot be extended for measurements of fine particles.

Using the *hammer-anvil principle* to detach particles from a surface is another option, which was considered in this thesis. Particles are placed on the front side of a plate or block, the "anvil", and detached due to a shock pulse generated by the "hammer" hitting the backside of the "anvil". Possible technical systems are, for instance, a shock pendulum [97] or a pneumatically driven shock exciter using a projectile, which is accelerated by pressurized air, as a hammer [98]. The shock pendulum is for example used in the automotive industry. However, accelerations provided by these devices (maximum $200 - 15\,000\,g$) are by far too small to detach particles in the desired size range. Thus, the hammer-anvil principle cannot be used to measure adhesion of fine particles.

Summarized, defined accelerations of the magnitude, which is necessary to detach $1 - 5\,\mu\mathrm{m}$ sized particles, cannot be generated with simple technical systems like piezo actuators or devices employing the hammer-anvil principle.

5.1.3 Hopkinson Bar System: The general Idea

As discussed in chapter 4, a Hopkinson bar can provide accelerations of great magnitude. Commercial shock excitation systems based on the Hopkinson bar principle achieve up to $200\,000\,g$ at the bar's free end and have the potential to generate even higher acceleration values.

The new technique to measure particle adhesion developed in this thesis utilizes the Hopkinson bar principle to detach particles from a surface, employing a shock excitation system, which is standardly used for calibration purposes.

The main idea of the method is shown in Figure 5.2. The sample with the powder particles is attached to the right free end of the Hopkinson bar, which is in this case a long thin titanium bar. To enable detachment the particles are deposited on the backside of the overlapping edge (for details concerning sample geometry see chapter 5.2).

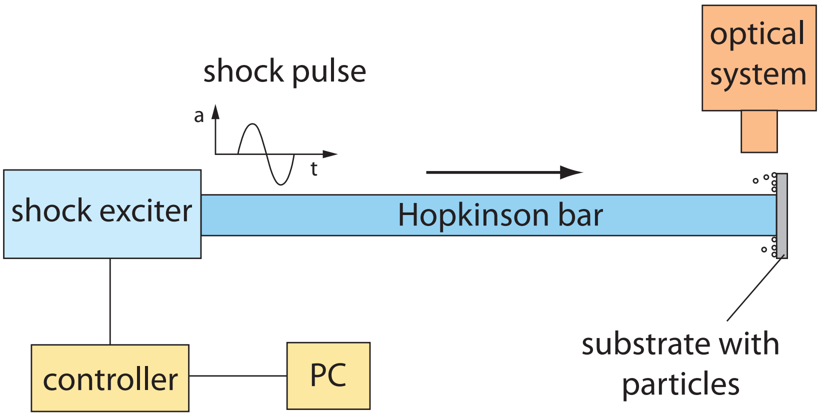

Figure 5.2: Schematic of the Hopkinson bar method to measure adhesion forces of particles.

Afterwards, a shock pulse is excited by shooting a projectile pneumatically against the left bar end (air gun). This mechanical impact generates an elastic wave that propagates through the bar and is reflected at the right free end. Superposition of incoming and reflected wave leads to a doubling of displacement and acceleration according to Equation 4.11. By varying the speed of the projectile, the force pulse dF/dt and therefore the acceleration at the right bar's end can be controlled.

Figure 5.3 shows the principle shape of the pulses: the propagating force pulse in the bar $F(t)$ causes a velocity pulse $v(t)$ at the right free bar's end which has the same time dependency according to Equation 4.9. The resulting acceleration $a(t)$, which is the derivative of the velocity, is ideally a sinusoidal one-period shock pulse. With increasing impact speed of the projectile the pulse height of $a(t)$ increases, whereas the pulse width and the principle shape remain constant. The displacement $x(t)$ at the bar's end is the integral of $v(t)$.

Stepwise increase of the acceleration leads to detachment of the particles from the sample

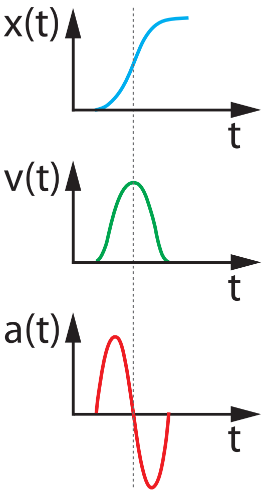

Figure 5.3: Principle shape of the displacement pulse $x(t)$, the velocity pulse $v(t)$ and the acceleration pulse $a(t)$ at the free end of the Hopkinson bar.

surface as soon as the inertial forces exceed the adhesion force. The sample acceleration is measured via laser Doppler vibrometry and particle detachment events are detected by optical video microscopy. The latter also allows to determine the particle radii. The microscope images are automatically analyzed and a statistical distribution of adhesion forces is obtained.

5.2 Experimental Set-up

To generate the surface acceleration for particle detachment a custom-made shock excitation system is used, built by the company SPEKTRA GmbH in Dresden. In principle it works like their commercial Hopkinson bar shock devices, however, it had been modified by SPEKTRA to achieve even higher accelerations than the standard systems.
According to $a(t) = 2 \cdot c_0/(EA) \cdot dF/dt$ (Equation 4.11) the bar geometry as well as the bar material have an influence on the achievable acceleration. The acceleration at the bar's end is maximized at a given force by maximizing the factor

$$K = \frac{c_0}{E \cdot A} \tag{5.2}$$

with the wave propagation velocity c_0, the Young's modulus E of the bar material and the cross section area A of the bar. With the relation $c_0 = \sqrt{E/\rho}$ (Equation 4.4) one obtains

$$K \propto \frac{1}{d^2} \cdot \sqrt{\frac{1}{E\rho}} \tag{5.3}$$

where ρ is the density of the bar material and d the bar diameter. Thus, halving the bar diameter d results in a four times higher K value. Therefore the diameter of the bar employed in the custom-made device had been reduced compared to the commercial systems, that have a typical bar diameter of $16 - 30\,\mathrm{mm}$. Furthermore the force pulse dF/dt had been modified to achieve a smaller pulse duration time compared to the standard systems, which have a typical pulse width of $20 - 25\,\mu\mathrm{s}$. Both modifications lead to a higher acceleration at the bar's end. Accelerations in the order of $500\,000\,g$ are possible with the modified shock excitation system, while the commercial ones achieve maximum $200\,000\,g$.
As bar material titanium is used. The chosen titanium alloy has a Young's modulus of $E = 110\,\mathrm{GPa}$ and a density of $\rho = 4.42\,\mathrm{g/cm^3}$ resulting in a good K value. Additionally, titanium has a high yield point (1000 MPa for the used alloy) and can therefore stand high mechanical stresses and strains while maintaining linear elastic behavior.
During this thesis, a new set-up was constructed to enable adhesion force measurements of particles (Figures 5.4 and 5.5) using the custom-made shock excitation system by SPEKTRA.

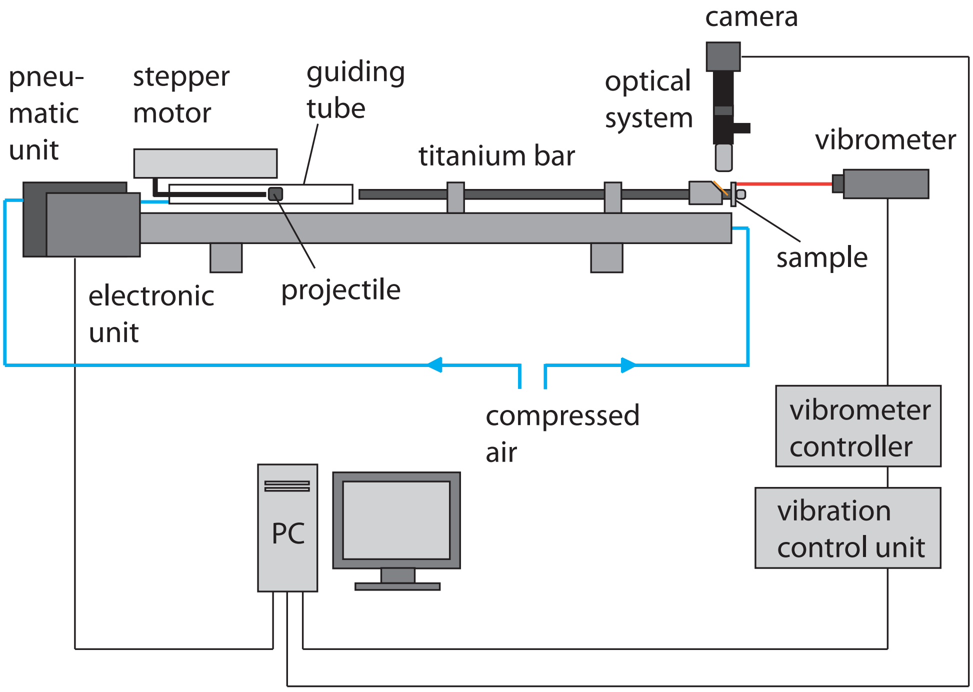

Figure 5.4: Set-up of the Hopkinson bar system, which was constructed to measure adhesion forces of particles.

The Hopkinson bar shock excitation system consists of a cylindrical titanium bar of 1 m in length and 10 mm in diameter. The bar is mounted on an aluminum frame using clamps lined with foam rubber so that the elastic wave can propagate unimpeded. The projectile consisting of a mushroom-shaped steel core and a Teflon liner (Figure 5.5a) is loaded into a guiding tube in which it can be shot pneumatically against the left bar end. The projectile is accelerated with pressurized air (4 bar) and retracted with vacuum using magnetic valves in a pneumatic unit that can be controlled electronically. The starting point of the projectile within the guiding tube is defined by a small rod which is inserted into the end of the guiding tube and acts as a stopper during retraction to the starting point. Its position can be varied via a stepper motor. The distance between projectile starting point and the left bar end determines the acceleration length and thus the impact speed of the projectile. The projectile speed can reach up to 15 m/s maximum. A linear dependence exists between acceleration length of the projectile and the resulting acceleration amplitude at the right bar end. Due to this linear relation between starting point of projectile and acceleration it is possible to generate well defined accelerations up to 500 000 g with a reproducibility of about 5%. The acceleration pulse at the bar's end has a width of 10 µs. An overview of the technical details is given in Table 5.1.

Shock pulse excitation and retraction of the projectile are automatized and can be controlled by a computer, as well as the positioning of the projectile with the stepper motor. The acceleration at the bar's end is mainly generated by longitudinal waves [99]. The influence of transversal or torsional waves can be neglected. Therefore all wave propagation processes in the bar can be described by the elastic longitudinal 1-dimensional wave theory (chapter 4.1).

bar	material	titanium alloy: 6AL4V, AMS 4928
	Young's modulus	110 GPa
	density	4.42 g/cm^3
	yield point	1000 MPa
	diameter	10 mm
	length	1 m
	velocity at bar's end	about 40 m/s maximum
	acceleration at bar's end	$(0.1 - 5) \cdot 10^6$ m/s^2
	acceleration pulse width at bar's end	10 µs
projectile	diameter	22 mm
	mass	18 g
	impact speed	about 15 m/s maximum
	air pressure	4 bar

Table 5.1: Technical details of the Hopkinson bar shock excitation system.

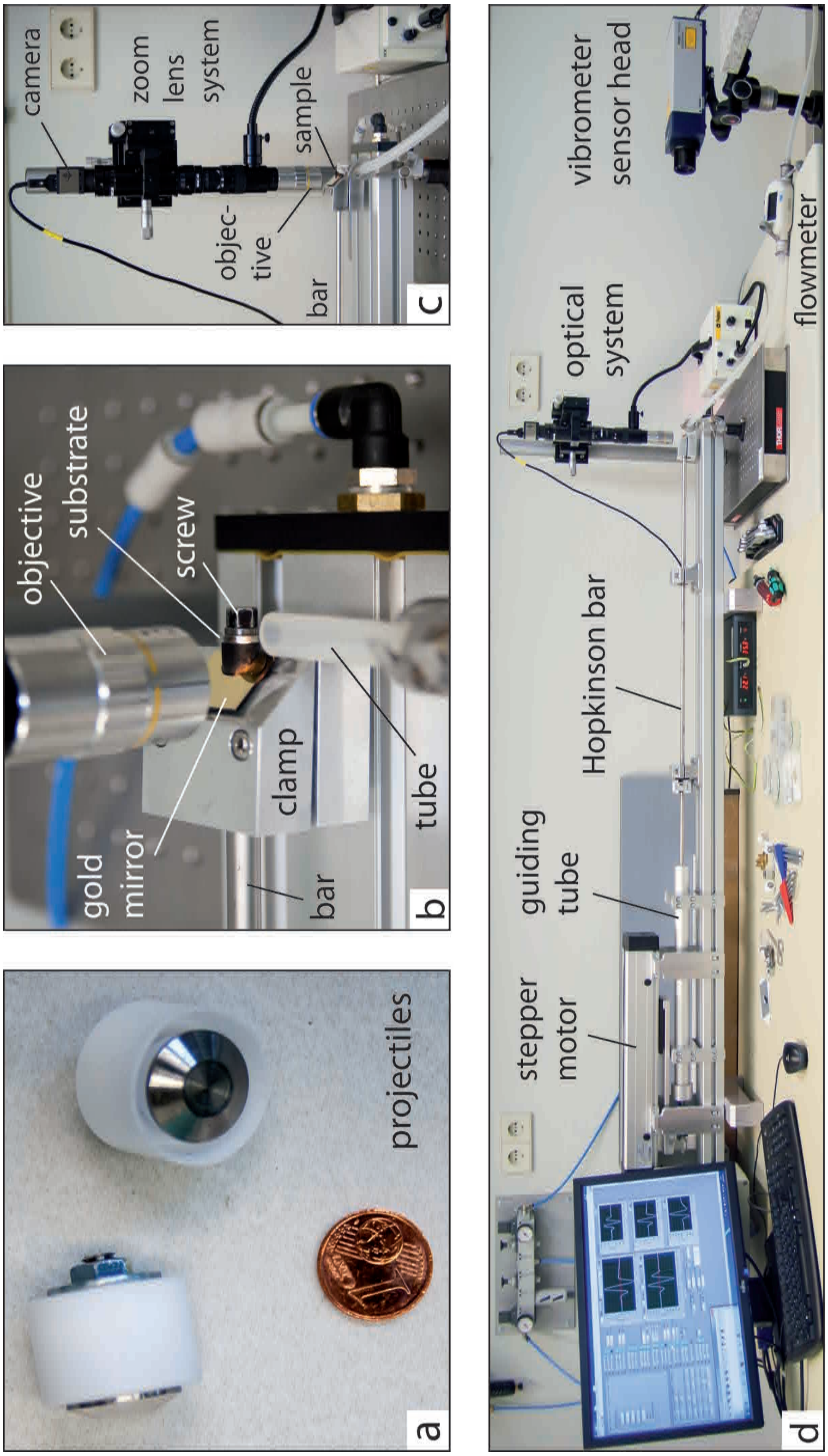

Figure 5.5: Photographs of the experimental set-up: (a) used projectiles consisting of a steel core and a teflon liner, (b) sample configuration, (c) optical system and (d) the complete Hopkinson bar set-up.

5.2.1 Sample Geometry

As sample surface a circular stainless steel plate of 16 mm in diameter is used. Here, steel with high quality is required to avoid plastic deformation of the sample plate during the shock pulses. The sample with the adhered particles is attached to the right end of the bar (Figures 5.4, 5.5b and 5.6).

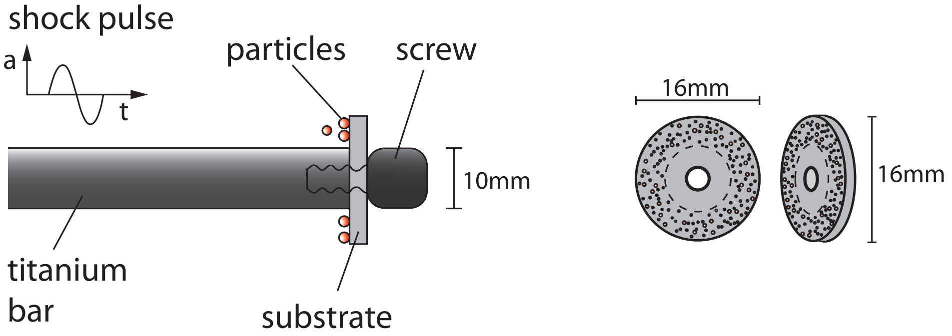

Figure 5.6: Sample geometry in the Hopkinson bar system: the sample plate with the particles is screwed to the bar's end. To allow particle detachment it overlaps the bar and particles are located on the backside of the overlapping rim.

To optimize the mechanical coupling between bar end and sample and to achieve full transfer of the acceleration, the plates were screwed to the bar end with a titanium screw with a fixed torque of 3.5 Nm. The titanium screw is necessary to obtain a stable and reproducible acceleration signal on the sample which was not possible by using steel screws (chapter 6.4). In some cases the steel screws even loosened after few shock pulses. The bar, including sample plate, moves about 0.3 mm forward during each shock pulse due to momentum conservation. To allow particle detachment during an acceleration pulse, the sample plate was designed in a way that it overlaps the bar end by 3 mm (Figure 5.6). The particles are located on the backside of the overlapping rim. This geometry ensures that particles experience an acceleration away for the surface first and are not first pressed against the surface.

5.2.2 Acceleration Measurement

The acting acceleration during the shock pulse is measured interferometrically with a laser Doppler vibrometer on the front side of the sample plate (Polytec OFV-525/-5000-S High Speed, bandwidth 2.5 MHz). The vibrometer device consists of a sensor head, which is mounted on a tripod, and a controller. The laser beam (wavelength $\lambda = 633\,\mathrm{nm}$, power $\leq 1\,\mathrm{mW}$, continuous wave, beam diameter about 1 mm) is adjusted at the overlapping edge of the plate exactly at the location that is investigated (Figures 5.4 and

5.5d). This measuring position is kept constant throughout the complete experiment.
A laser Doppler vibrometer can measure the velocity component of an object along the direction of the laser beam. Reflecting the beam at the moving surface causes a Doppler frequency shift which is measured by superposition of the incident and the reflected beam in an interferometer. This allows to determine the velocity of the moving surface. Generally, the output of a vibrometer device is a continuous analog voltage, which is directly proportional to the sample velocity.
Figure 5.7 shows the basic components of a laser Doppler vibrometer.

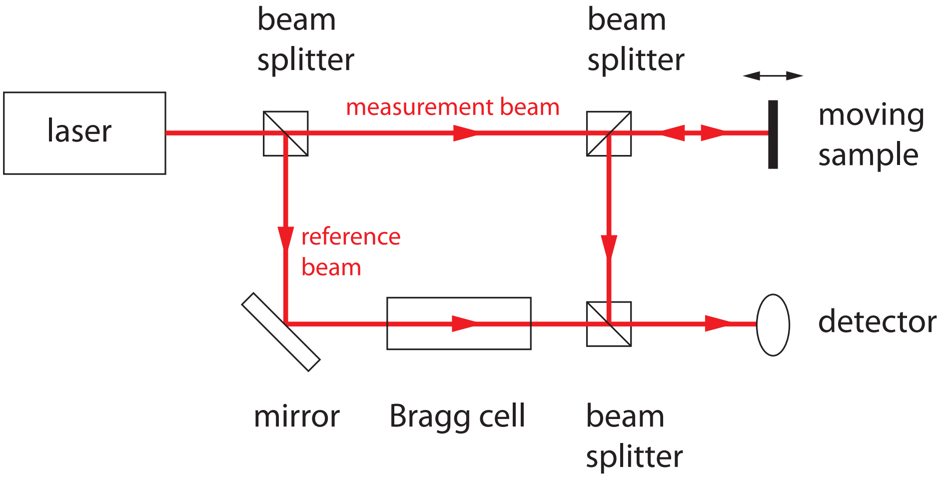

Figure 5.7: Schematic of the basic components of a laser Doppler vibrometer. Measuring the Doppler frequency shift of the laser beam, which is reflected on the moving sample, allows to determine the sample velocity. This can be realized by superposition of the reflected measurement beam and a reference beam in a heterodyne interferometer.

The beam of a helium-neon laser is divided into a measurement and a reference beam by a beam splitter. After passing a second beam splitter the measurement beam is focused on the moving sample surface where it is reflected. Due to the motion a Doppler shift is added to its frequency given by $f_D = 2v(t)/\lambda$, where $v(t)$ is the velocity component of the sample along the direction of the beam and λ is the wavelength of the light. The reflected measurement beam is combined with the reference beam at the photo detector. The detector output is a frequency modulated signal, which can be demodulated to derive the velocity versus time signal of the sample. To determine the direction of movement a Bragg cell is placed in the reference beam adding a known frequency shift of typically 40 MHz (heterodyne interferometer). When the sample is at rest this frequency shift causes a modulation frequency of the interference pattern of 40 MHz, defining the zero velocity position. Movement of the sample towards the interferometer reduces the modulation frequency while movement away from the interferometer raises the modula-

tion frequency. This way also the direction of movement can be detected.
In this set-up, measured analog signals are routed to a signal conditioner (vibration control unit, Figure 5.4) with the option to be filtered and amplified before they are digitized and further processed in the computer.
From the measured velocity signal of the sample surface during a shock pulse one obtains the acceleration and displacement signal on the sample plate (Figure 5.8) by derivation and integration, respectively. The relevant part of the acceleration signal (Figure 5.8, left) causing particle detachment is the first positive peak with a pulse width of $9-13\,\mu s$ that stems from longitudinal wave propagation in the elastic bar. The smaller peaks arise from reflections and dispersion effects of the pulse. The maximum value of the first positive peak in the acceleration signal is used for calculation of adhesion forces.

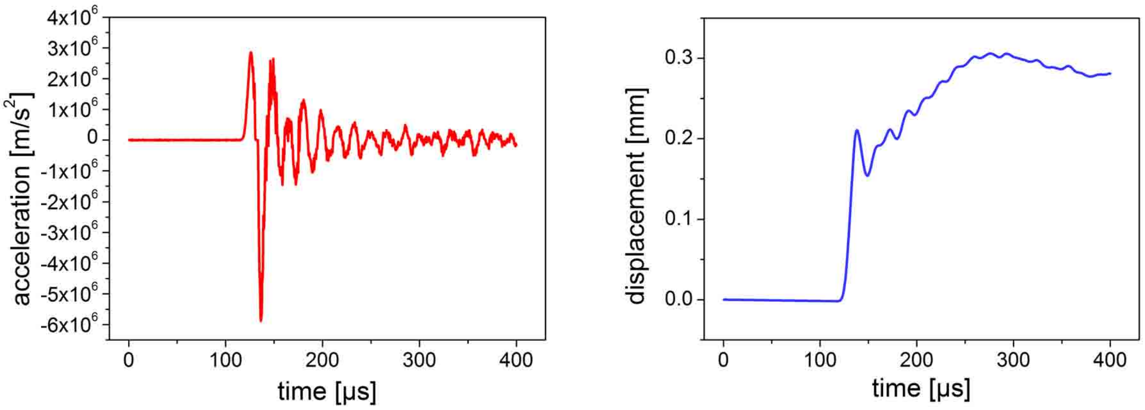

Figure 5.8: Acceleration signal (left) and displacement signal (right) on the sample plate during a shock pulse measured with the laser Doppler vibrometer.

The displacement signal (Figure 5.8, right) shows the forward movement of the complete bar including sample plate in the order of 0.3 mm for each shock pulse due to momentum conservation. The small overshot peak in Figure 5.8 (right) originates from the elastic response of the sample plate since the overlapping edges first bend forward and subsequently snap backwards during the shock pulse.
With the used laser Doppler vibrometer velocities up to 20 m/s are detectable (measuring inaccuracy 1.5%). This is the limit of maximal measurable velocities with current vibrometer devices available on the market. A velocity of 20 m/s corresponds to an acceleration of about $300\,000\,g$ for the $10\,\mu s$ pulse in the used Hopkinson bar system. Higher accelerations cannot be directly measured.
However, as already mentioned, the acceleration at the bar's end (maximum value of the first positive peak in the acceleration signal) is linearly related to the starting point of the projectile. The same applies to the acceleration on the sample plate at a fixed position. Due to this linear relation between acceleration on the sample and starting

point of the projectile (motorsteps number), one can determine the acting acceleration above the measuring limit from a calibration plot (Figure 5.9).

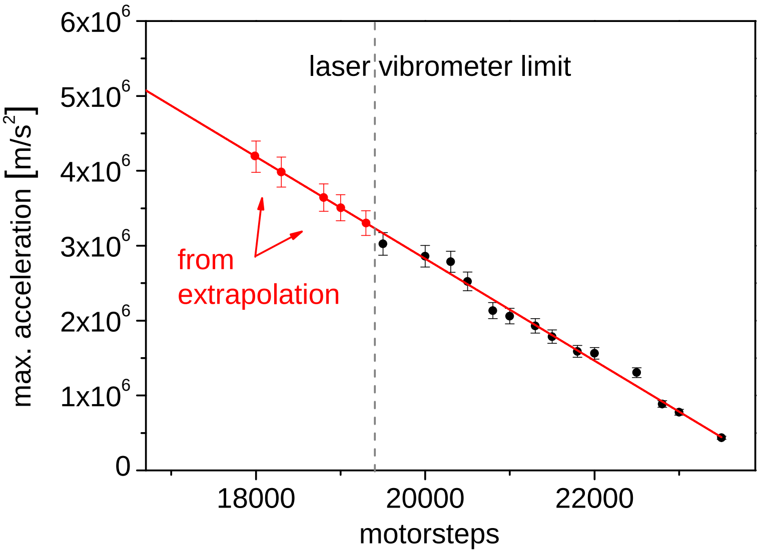

Figure 5.9: Calibration plot for measured sample surface accelerations. An extrapolation allows determination of the acceleration above the measuring limit of the vibrometer. Accelerations in the order of 500 000 g can be achieved with the Hopkinson bar system.

For the corresponding experiment, the maximum acceleration values measured on the sample (at the position that is investigated) are plotted versus the number of motorsteps, representing the starting position of the projectile in the guiding tube. With increasing distance between projectile and bar end, the number of motorsteps decreases. Especially for acceleration values above $1 \cdot 10^6$ m/s^2 a linear relation exists. After fitting the data with a linear function, the fit is linearly extrapolated above the measuring limit (10 000 points). The error bars below as well as above the vibrometer limit in Figure 5.9 correspond to the reproducibility of the shock pulses of 5%.

Assuming that the linear relation also holds above the measuring limit, one can calculate adhesion forces from the extrapolated acceleration values. Thus, the extrapolation allows determination of adhesion forces of particles that were detached above the measuring limit of the vibrometer. Figure 5.9 also indicates that accelerations up to 500 000 g are achievable with the used Hopkinson bar system. Higher values cause material damage of the bar and the projectile, particularly of the projectile teflon liner.

5.2.3 Optical System

To detect particle detachment events and determine particle diameters an optical system was developed that allows observation of the sample during the experiment (Figures 5.5b, 5.5c and 5.10).
It consists of a clamp that is fixed to the bar with foamed rubber. In addition, a gold coated glass plate acting as a mirror is attached magnetically to the clamp under 45°. The glass plate (26 mm × 22 mm) was cut according to Figure 5.11 and afterwards coated with a gold layer by thermal evaporation.

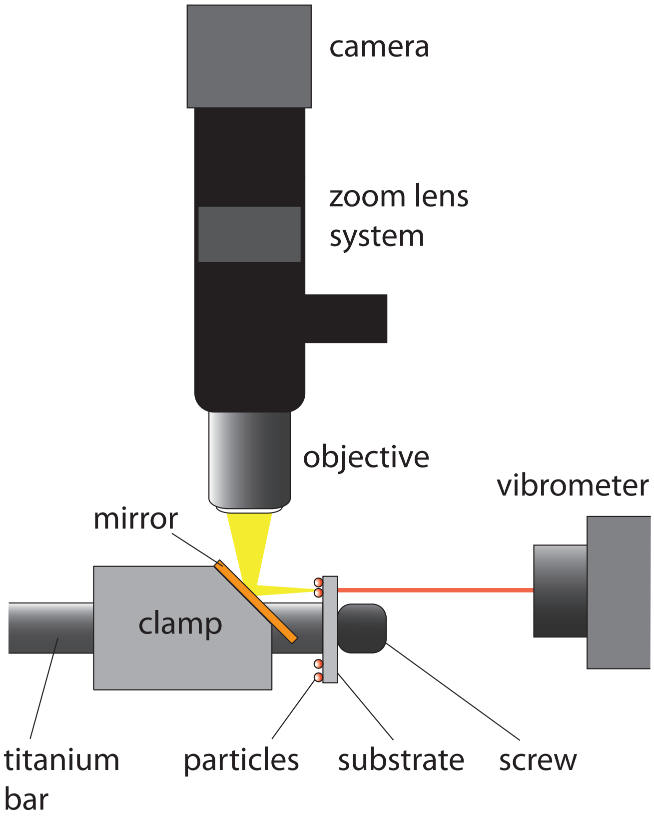

Figure 5.10: Optical system to detect particle detachment events and determine particle diameters during the experiment (side view).

Via the mirror the sample surface can be observed with a video microscope consisting of a tube system with variable zoom (Navitar 6.5x UltraZoom, 3 mm fine focus, detented zoom with nominal positions at 0.7×, 1×, 2×, 3×, 4× and 4.5×, coaxial illumination with 150 W cold light source, Polytec), a 10× objective (M Plan Apo, working distance 33.5 mm, numerical aperture 0.28, Mitutoyo, Japan) and a CCD camera (uEye UI 2280 SE monochrome, 2448 × 2048 pixels). Depending on the actual zoom setting the resulting microscope images have typically a field of view between 871 × 730 μm^2 (zoom setting 1×) and 250 × 298 μm^2 (zoom setting 3×).

This optical system allows to perform measurements without dismounting the sample after each acceleration step for image analysis, which considerably reduces measuring effort and time.

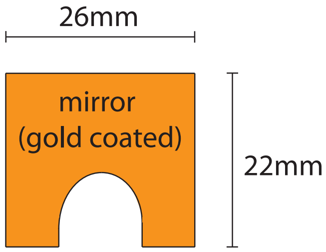

Figure 5.11: Front view of the gold coated glass plate acting as a mirror to observe the sample surface during an experiment. It is magnetically attached under 45° to the clamp, which is fixed to the bar.

5.2.4 Air Stream

To avoid reattachment of detached particles a lateral air stream with low flow rate (10 50 l/min in the tube) is applied next to the sample plate (Figure 5.12).
Reattachment of particles to the surface can occur especially due to the backwards movement of the overlapping edges of the sample plate during a shock pulse. As elastic response the edges first bend forward and subsequently snap backwards during the pulse (overshot peak in Figure 5.8, right).
The applied air flow leads to horizontal dislocation of already detached particles away from the surface. The flow rate in the tube is measured with a thermal mass flowmeter (4000 Series, TSI Instruments Ltd.).

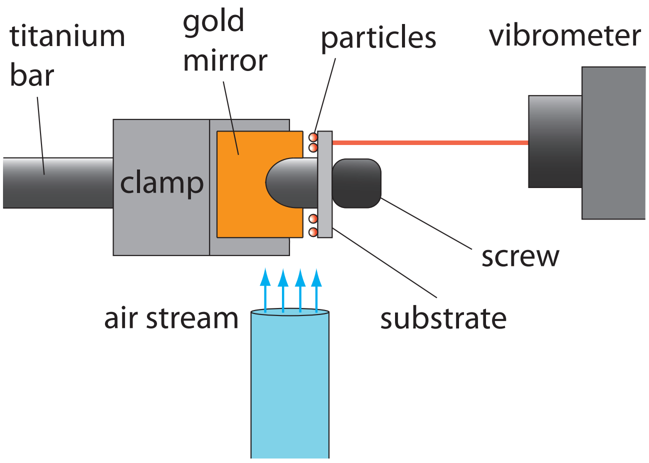

Figure 5.12: Air stream with low flow rate for horizontal dislocation of detached particles (top view).

5.3 Measuring Procedure

For measurement of adhesion forces, particles are dispersed on the sample surface to achieve an as dense as possible coverage of the substrate while still avoiding agglomeration of particles (chapter 6.2.2). The sample plate is then screwed to the bar's end and a series of shock pulses with stepwise increase of acceleration is applied.
The acceleration on the sample is increased by stepwise increase of the acceleration length of the projectile in the guiding tube. This is done by decreasing the motorsteps number, typically from 23 500 (small distance between projectile and bar) to 16 000 (large distance between projectile and bar) in increments of $200 - 300$. As a consequence, the acceleration step size is about $5\,000 - 20\,000\,g$. Smaller step sizes would not make sense since they would become comparable to the variation in acceleration due to shock pulse reproducibility. The number of shock pulses per experiment is typically between 20 and 30, depending on the investigated particle-surface combination. Projectile position and shock pulse excitation are controlled by a LabView program (written by M. Brucke, SPEKTRA GmbH, using LabView 8.6, National Instruments).

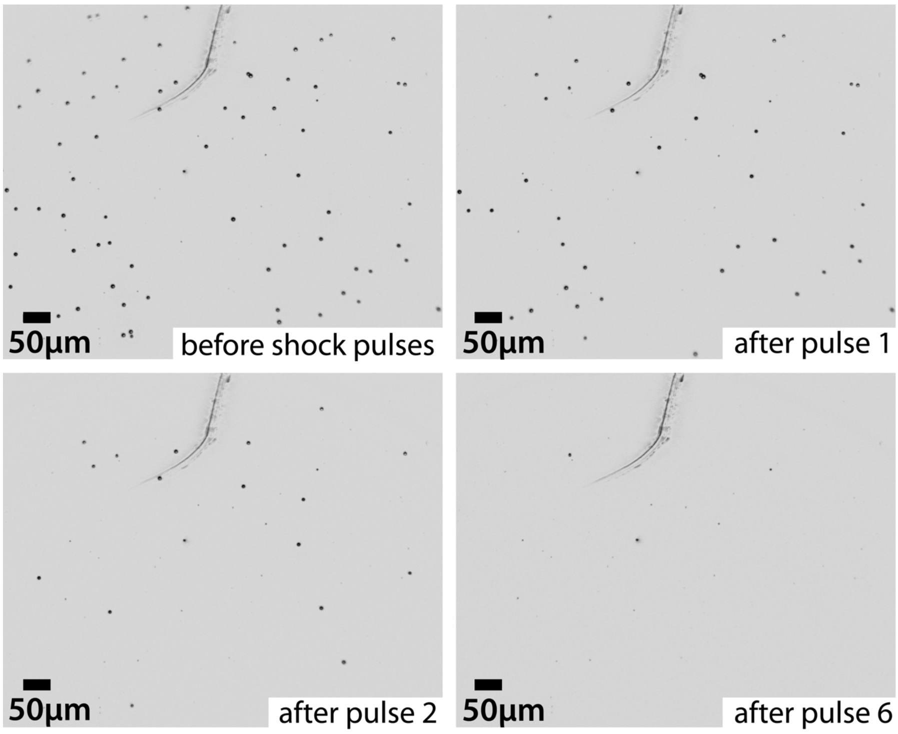

Figure 5.13: Microscope images showing detachment of spherical silica particles (diameter 5 μm) with increasing acceleration of the substrate in the Hopkinson bar system. The defined scratch helps to find the exact location on the surface.

When the inertial force exceeds the adhesion force, particles detach from the surface. After each shock pulse a microscope image is taken with the camera at exactly the same location on the sample surface (Figure 5.13). A defined scratch on the surface helps to find the location. To obtain better statistics, not only one but several locations can be investigated by translating the optical microscope with an x-y stage and taking consecutive images. Taking several microscope images per shock pulse also helps to verify that particles, which have disappeared after a pulse, really detached and not only rolled out of the image section.

Since the bar moves forward during a shock pulse, one needs to refocus by hand on the surface after each pulse. The camera is controlled by the software uEye Cockpit (IDS Imaging Development Systems GmbH).

The microscope images in Figure 5.13 exemplarily show detachment of spherical silica particles (diameter 5 µm) with increasing acceleration of the substrate. Here, pulse 1 corresponds to an acceleration of $(0.97 \pm 0.01) \cdot 10^6\,\mathrm{m/s^2}$, pulse 2 to an acceleration of $(1.14 \pm 0.02) \cdot 10^6\,\mathrm{m/s^2}$ and pulse 6 to an acceleration of $(1.93 \pm 0.03) \cdot 10^6\,\mathrm{m/s^2}$. For better overview, not the raw images but processed images are shown here: the contrast was enhanced and illumination gradients in the background were subtracted (Adobe Photoshop CS3 extended, version 10.0).

The velocity versus time signal of the sample plate during each shock pulse, measured with the laser Doppler vibrometer at the location which is investigated, is displayed in the LabView program. By derivation the acceleration versus time signal is obtained and afterwards saved. The maximum of the first positive peak is used as acceleration value for further calculations.

Comparison of before and after images with a program for automatic image processing allows identifying detached particles and determination of their diameters. From the recorded acceleration values the adhesion force for each detached particle can be calculated. Thus one obtains adhesion values of up to some hundred individual particles with one single experiment, depending on the surface coverage within the field of view of the video microscope.

5.4 Data Evaluation

The microscope images taken after each shock pulse are analyzed with automatic image processing[1]. After subtracting illumination gradients and removing irregularities like scratches (Adobe Photoshop CS3 extended, version 10.0), the images are converted from gray scale to black and white (binary) images (ImageJ, Version 1.46r). Particles within a predefined size and circularity range in the binary image can then be identified automatically in ImageJ to determine their coordinates and diameters. In this thesis a delphi program was developed that compares the images from the consecutive shock pulses, giving out a list of detached particles that can also be cross-checked by eye.

---

[1] The author acknowledges programming support by Markus Rein

To determine the diameter of detached particles a second program was developed using Mathematica (Wolfram Mathematica 7.0.0). Here, particles are assumed to be ideally spherical. The particle diameter determined from the black and white image in ImageJ strongly depends on the set threshold, defining which gray values correspond to "black" and which to "white" in the binary image. Thus, to obtain more precise values, the particle diameters are determined separately by fitting a circle to the particle shape in the gray scale image. The diameters and coordinates from the binary image derived by ImageJ are used here as starting parameters.
With a third program, which was developed using Mathematica, the adhesion forces of the detached particles and the corresponding errors can be calculated from the determined diameters and the acceleration values measured with the laser Doppler vibrometer. Adhesion forces are afterwards plotted with the program Origin (OriginPro 8.5.0G SR1, OriginLab corporation).
In the following, the different steps of data evaluation are described more precisely.

5.4.1 Image Processing and Identification of detached Particles

The raw images taken with the camera are 8-bit gray scale images (Figure 5.14a). In the first preparation step, two consecutive images, corresponding to the shock pulses N and N+1, are merged in Photoshop to cut out the overlapping image section. This is necessary since the consecutive camera images do not show exactly identical areas of the sample surface, however, all particles are later identified via their coordinates. Afterwards, each image is processed. Irregularities like scratches are removed at first. Since the field of view is not homogeneously illuminated, an illumination gradient arises in the microscope images. This gradient is removed by subtracting a smoothed copy of the picture (Gaussian smoothing filter) from the original one and inverting the result. Also brightness and contrast are adjusted.
In ImageJ the pictures are processed further. First, the scale is set, which converts pixels to micrometers depending on the used zoom in the optical system. Afterwards the images are converted from gray scale to binary (Figure 5.14b). Then they only contain the colors black and white, therefore a threshold has to be set defining which gray values are assigned to be black and which white. Additionally, the ImageJ function "fill holes" is applied which fills out the area of particles that only show a border in the binary image. This simplifies the later identification of particles. To make the procedure of image processing faster macros were written in Photoshop and ImageJ.
After image processing particles within a predefined size and circularity range are identified on the binary images of pulse N and pulse N+1 using the ImageJ funtion "analyze particles". This function gives out an ASCII file with a list of the coordinates and the area of the detected particles on the concerned image.
A delphi program was developed (written by M. Rein using Borland Delphi 3 profes-

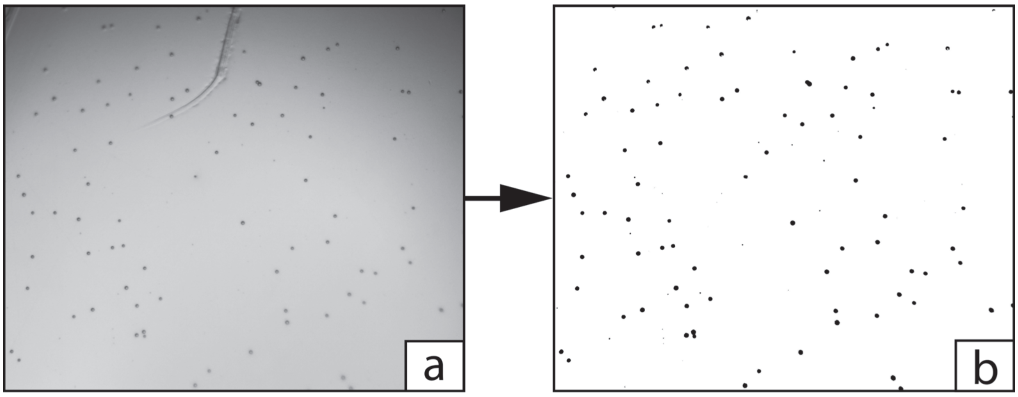

Figure 5.14: Raw gray scale image of particles (silica 5 µm) on the sample surface taken with the camera (a). After removing irregularities and the illumination gradient the image is converted into a black and white (binary) image (b), which simplifies the automatic identification of particles. For better overview brightness and contrast of the shown raw image were enhanced.

sional) in order to determine which particles have detached in the transition from pulse N to pulse N+1. This is realized by comparing the parameters of identified particles of two consecutive images, which are listed in the ASCII files from ImageJ. Particles of image N and image N+1 are compared concerning their x and y coordinate and their area within a preset tolerance range. The tolerance range, corresponding to the maximum allowed deviation in x and y coordinate and area, defines the range within which two particles in picture N and N+1 are regarded to be identical. The program takes the parameters of the first particle in picture N and compares them sequentially with the parameters of all particles in picture N+1. If a particle from picture N+1 fits to the regarded particle from picture N, which means that the deviation in location and area is within the defined tolerance range, it is saved on a list of matches. In case that several matches are found, the particle from picture N+1 with the smallest deviation is chosen. Both matching particles are considered to be identical. Consequently, the particle from picture N is regarded as not detached. In case that the particle from image N detached the list of matches is empty. This comparing procedure is repeated for all particles in image N. Finally, the program gives out three different ASCII files. The first one contains a list of particles from image N for which an identical partner in image N+1 could be found. This corresponds to a list of particles that did not detach. The second file contains a list of particles from image N for which no matching partner could be found in image N+1 and which should therefore have detached. The third file lists those particles from image N+1 without a matching partner in image N. This way also particles which might have rolled or reattached during the shock pulse can be identified. Additionally, the delphi program creates a file with color information. This is used to visualize detached and possibly rolled particles in the images. Particles that detached in picture N+1 are colored red in picture N. Particles that appeared at a certain location in picture N+1 but not in picture N and therefore might have rolled or reattached are marked green in picture N+1. This visualization helps to cross-check the suggestions of the program by eye.

For all experiments performed in this thesis the detachment of each single particle was verified by eye before further evaluation. In few cases rolling or reattachment of a particle was observed, which was verified by eye as well.

5.4.2 Size Determination of detached Particles

The list of detached particles obtained from the delphi program contains the area values of the particles, which were determined from the binary image using the "analyze particles" function in ImageJ. Assuming perfect spheres, it would be possible to derive the diameters. However, the area of a particle in a binary image strongly depends on the set threshold. The threshold has to be chosen in a way that also light gray particles appear black in the binary image to make sure that they are detected. However, this leads to an imprecise particle diameter. Thus, the diameter of detached particles, which is used to calculate the adhesion forces, is determined separately in a Mathematica program (written by M. Rein) using the original gray scale images. Here, a spherical shape of the particles has to be assumed.

In an 8-bit gray scale image 8 bits are used to indicate the gray value of each pixel. This allows $2^8 = 256$ different shades of gray for each pixel scaling from a value of 0, which represents black, to a value of 255, which represents white. The Mathematica program uses the coordinates and the area value of a detached particle obtained from the binary image by ImageJ as starting parameters to read out the gray values of the corresponding particle in the gray scale image.

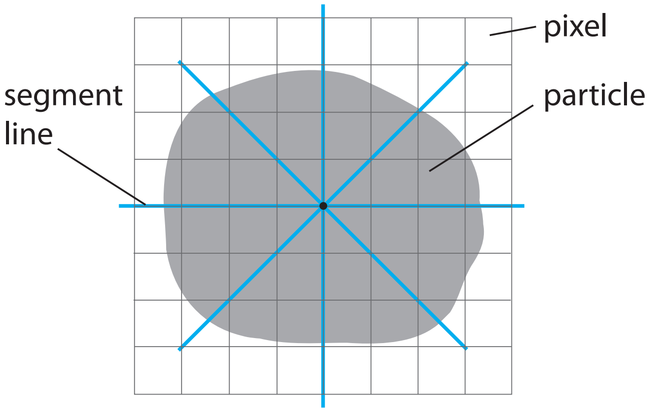

Figure 5.15: In order to determine the diameter of the particle in the gray scale image it is divided into n equally sized segments by defining n lines running from the center in different directions.

The particle in the gray scale image is divided into n equally sized segments by defining n lines of length l running from the center in different directions (Figure 5.15). The center, which is the starting point, is defined by the value from the binary image. Along these lines the profile of gray values is read out in order to find the particle border. The length of the lines defines the number of pixels taken into account. It equals twice the radius suggested by ImageJ for the particle's radius in the binary image. The choice of the line length can effect the further determination of the particle diameter.

Typically a particle on the gray scale image has a bright center surrounded by a darker ring with a certain width (Figure 5.17). The corresponding line profile showing gray value versus distance in pixels from the center is illustrated in Figure 5.16. The higher the gray value the brighter is the shade of gray. The profile has a maximum in the center, representing the bright spot in the middle of the particle, followed by a minimum, which represents the dark ring, and a second maximum due to the surrounding area (image background), which is normally brighter than the particle.

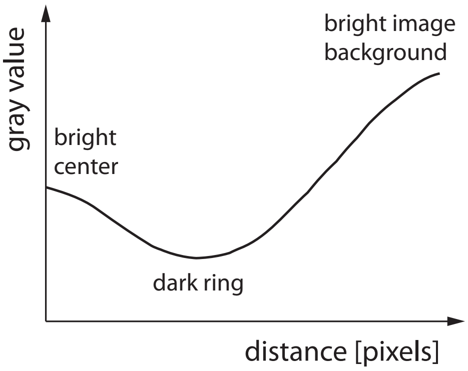

Figure 5.16: Schematic of a typical line profile of a particle showing gray value versus distance in pixels from the particle center.

For each line profile the position of the particle border is determined. The correct particle border is in most cases located at a pixel position around the minimum gray value of the line profile. This was verified by comparing microscope images of spherical particles with images from scanning electron microscopy (SEM). Best results for the particle diameter are obtained when the particle border point is determined by averaging around the position of the minimum gray value according to

$$x_B = \frac{c \cdot x_{max} + x_{min}}{2} \tag{5.4}$$

where x_B is the position (in pixels) of the particle border, x_{min} the position of the minimum gray value and x_{max} the position of the maximum gray value (image background). Here, c is a weighting coefficient that can take values in a range of [0...1], therefore

$$\frac{x_{min}}{2} \leq x_B \leq \frac{x_{max} + x_{min}}{2} \tag{5.5}$$

This way, for each of the n segment lines a border point is obtained.
The set of n border points for the particle forms a structure which is in general not spherical. In order to determine the particle diameter a circle is fitted. To find the radius r and the center of the circle (x_0, y_0) that fits best to all border points the model

$$f(x, y) := (x - x_0)^2 + (y - y_0)^2 - r^2 \tag{5.6}$$

is used. For an ideal circle $f(x, y)$ is zero, thus the values $f_i(x, y)$ for each border point P_i are summarized and minimized. The result is a value for the radius r and the center (x_0, y_0) of a circle that fits the structure of the set of border points. The quality of this fit depends on the accuracy of the chosen starting point of the segment lines. The more this starting point matches to the real particle center the more precise is the fit. Therefore, the fit is repeated using the derived center of the circle from the previous fit as new starting point for the segment lines. This iterative approach is performed as long as the center point derived from the fit deviates from the starting point for the segment lines at the beginning of the iteration. From the final circle fit a radius and a coordinate of the center can be obtained. The complete cycle is performed for 11 values of the weighting parameter c in a range of 0 to 1. The average of the 11 obtained coordinates for the center of the circle and the average of the 11 obtained radii are used for the final circle that fits the particle. The diameter of this final circle is considered to be the particle diameter. This circle is visualized in the gray scale image (Figure 5.17) and can easily be cross-checked by eye.

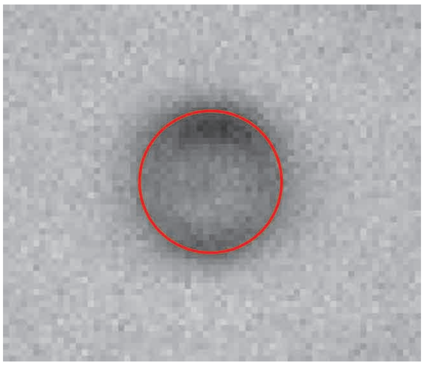

Figure 5.17: Determination of the particle diameter by fitting a circle to the particle border in the gray scale image.

However, not all particles in the image have the same gray value profile. Most of them show the bright spot in the middle with a darker ring at the border (Figure 5.17), which was described above. But some particles only consist of a dark spot without bright center. For these particles deviations between their real diameter and the diameter determined with the Mathematica program can arise. Furthermore, for polydisperse particles in particular, not every particle is exactly in the focus of the microscope. This leads to a blurring of the particle border. Thus, a cross-check by eye is necessary in every case.

In this thesis, for every performed experiment the diameters of all detached particles were additionally determined by manually fitting a circle in the gray scale image with Photoshop. In case of a deviation from the suggested diameter of the Mathematica program, always the manually determined value was chosen. For more than 90% of the particles the deviation was smaller than 1.5 µm, depending on the investigated particle-surface combination, the zoom setting and the actual illumination.

Comparison of microscope images of spherical particles with images from scanning electron microscopy (SEM) shows a total error of maximum 1 µm for the manual determination, which corresponds to a diameter error of $\Delta d = \pm 0.5\,\mu\text{m}$. This error in diameter is used for all experiments. The determination with the Mathematica program shows a total error of about $1 - 1.5\,\mu\text{m}$ in most cases.

5.4.3 Calculation of Adhesion Forces

From the determined particle diameters and the measured acceleration for each shock pulse the adhesion force of a detached particle can be calculated. This is done automatically with a third program in Mathematica. The detached particles are listed in an Excel file (Microsoft Office Excel 1997-2003) with their corresponding diameters and the number of the shock pulse which caused detachment. In a second Excel file the shock pulses are listed with the corresponding numbers and the respective acceleration on the sample plate measured with the laser Doppler vibrometer or determined from the extrapolation. From the Excel files the program calculates the adhesion forces for each detached particle according to

$$\begin{aligned} F_{adh} &= \rho \frac{4}{3} \pi R_P^3 \cdot a \\ \Delta F_{adh} &= \sqrt{(\rho \frac{4}{3} \pi R_P^3 \cdot \Delta a)^2 + (4 a \rho \pi R_P^2 \Delta R_P)^2} \end{aligned} \tag{5.7}$$

where ρ is the particle density, which is determined experimentally or taken from the manufacturer's information, R_P is the particle radius and a the acceleration. The error ΔF_{adh} is derived from Gaussian error propagation with the acceleration error Δa and the radius error ΔR_P. Within the measuring limit of the laser Doppler vibrometer the acceleration error corresponds to the vibrometer measuring inaccuracy of 1.5% ($\Delta a = 0.015 \cdot a$). Above the limit a is determined from the extrapolation, thus the error corresponds to the shock pulse reproducibility of 5% ($\Delta a = 0.05 \cdot a$). The error of R_P is given by the error in determination of the radius from the microscope images as $\Delta R_P = 0.25\,\mu\text{m}$. The density error is considered to be much smaller than the acceleration and the radius errors and is therefore neglected in the calculation.

5.5 Forces acting on the Particles in the Set-up

Considering a single particle on a flat surface, which is exposed to a shock pulse in the presented set-up, several forces are acting on the particle.

Due to a variety of attractive surface forces (chapter 2), the particle adheres to the substrate. For the particle-surface combinations investigated in this thesis, van der Waals forces are expected to dominate, whereas capillary and electrostatic forces play a minor role. Theoretical expressions for the adhesion force can be obtained with the JKR model (Equation 2.44), the DMT model (Equation 2.48) or the Rabinovich model (Equation 2.53).

Gravitational forces on the particle can be neglected for micrometer sized particles, since they are much lower than the surface forces.

The reflected shock wave at the bar's end causes a force pulse acting on the sample surface and therefore on the particle. This inertial force is given by

$$F_{detach} = \rho \frac{4}{3} \pi R_P^3 \cdot a \tag{5.8}$$

with particle density ρ, particle radius R_P and acceleration a of the surface.

Due to the lateral air stream that is used for removal of detached particles, fluid forces like lift and drag forces are acting on the particle as well. The lift force acts perpendicular to the flow direction, whereas the drag force acts parallel to the flow direction. The lift force on a particle near a flat wall in a linear air flow field in a tube can be described with a model by Leighton and Acrivos [100] which is in accordance with the results of Cherukat and McLaughlin [101]:

$$F_{lift} = 0.576 \cdot \rho_{air} \cdot \frac{d^4}{\nu_{air}^3} \left(\frac{6\eta_{air} \cdot c_{mean}}{h \cdot \rho_{air}} \right)^2 \tag{5.9}$$

with the density of air ρ_{air}, the particle diameter d, the dynamic and kinematic viscosity of air η_{air} and ν_{air}, the mean air velocity c_{mean} and the height of the tube h.
The drag force can be estimated according to O'Neill [102]:

$$F_{drag} = 5.1027 \cdot \pi \cdot \eta_{air} \cdot d \cdot c(y) \tag{5.10}$$

where $c(y)$ is the air velocity at the particle center.
To obtain an idea of the order of magnitude of the fluid forces in the presented set-up, lift and drag forces acting on the particles were estimated. Here, a laminar air stream was assumed with the low flow rates that were used in the performed experiments (measured in the tube). This estimation shows a negligible contribution of the fluid forces compared to the adhesion forces. Since the particles are not located inside but behind the air tube, the air velocity and thus the aerodynamic forces should be even smaller. As the influence of gravitational and fluid forces can be neglected, it is valid to determine the adhesion force of particles in the used set-up from the inertial force according to Equation 5.7.

6 Materials and Characterization

After development and construction of the Hopkinson bar system, adhesion forces of particles on a flat surface were measured using the new device. Two categories of particles were chosen. At first, to validate the new method, spherical particles with well known surface chemistry were used as model system. They were also employed for comparative adhesion measurements with the colloidal probe technique.
Secondly, in order to expand the applicability of the Hokinson bar device to more complex particles used for example in industry, strongly cohesive particles with corrugated shape were investigated.
In this chapter the employed materials, the sample preparation and the sample characterization with different experimental methods are described.

6.1 Particles and Substrates

Adhesion measurements were conducted with different powders consisting of spherical particles: polydisperse polystyrene powder (diameter $1-50\,\mu$m, polystyrene divinylbenzene (DVB), Duke Scientific Corp.) and porous silica powders (diameter $3.5\,\mu$m and $5\,\mu$m, Kromasil 100 SIL, pore size $100\,Å$). The particle properties are shown in Table 6.1.

material	diameter [μm]	r_{rms} [nm] (for $1 \times 1\,\mu m^2$)	density ρ [g/cm^3]
polystyrene DVB	$1-50$	0.57 ± 0.06	1.052
silica (porous)	3.5 and 5	4.67 ± 1.27	0.738

Table 6.1: Properties of the spherical particles investigated in this thesis.

Density values ρ of the particles were either obtained from the manufacturer (silica) or determined experimentally (polystyrene DVB) using an aqueous salt solution (measured by Gabriele Schäfer). The root mean square roughness r_{rms} of the particles was determined by AFM imaging (scanning area $1 \times 1\,\mu m^2$, chapter 6.3.3).
Figure 6.1 shows the particle morphology of the used polystyrene and silica particles imaged by scanning electron microscopy (SEM, chapter 6.3.1).

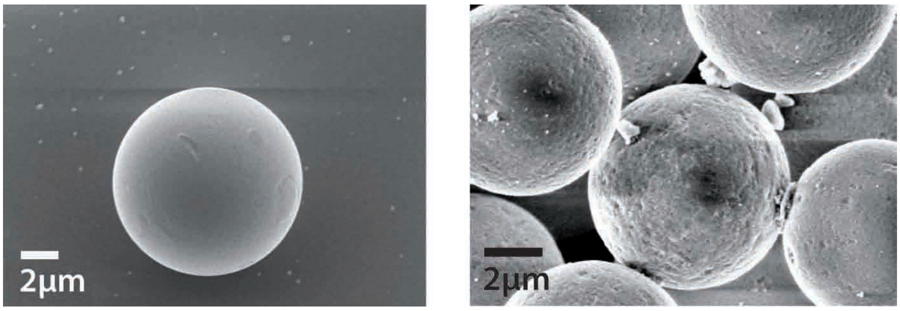

Figure 6.1: Spherical polystyrene particle on a polystyrene surface (left) and spherical porous silica particles (right) observed with SEM.

Moreover, dextran particles with a corrugated shape were investigated (dextran T1:dextran T3.5 = 9:1, diameter $2-4\,\mu m$, density $\rho = 1.47\,g/cm^3$). An SEM image of their morphology is shown in Figure 6.3.
Dextran is a branched glucan, which is a polysaccaride made of many glucose molecules. The structure of a fragment of a dextran molecule is illustrated in Figure 6.2. Dextran has many applications in the pharmaceutical and medical sector, where it is for example used in solution as blood plasma substitute, as carrier for vaccines or as lubricant in eye drops, but also in food industry as conditioner and stabilizer [103].

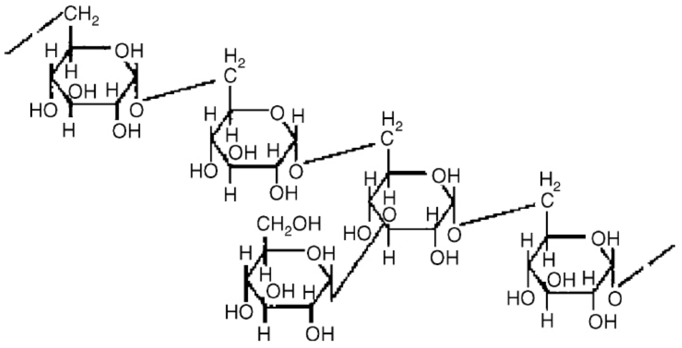

Figure 6.2: Structure of a fragment of a dextran molecule [103].

The corrugated particles had been fabricated by dissolving dextran T1 and dextran T3.5, which have different molecular weights, with ratio 9:1 in purified water and afterwards spray drying the solution (particles fabricated by Markus Wolkenhauer, Boehringer Ingelheim Pharma GmbH & Co. KG). Dextran T1 has a molecular weight of $M_W \approx 1000\,g/mol$, dextran T3.5 of $M_W \approx 3500\,g/mol$. The ratio of both determines the degree of surface corrugation of the resulting particles (Figure 6.3). The curvature of such a particle with wrinkled morphology is not being understood as an asperity or part of its surface roughness, but the curvature itself has its own nanoscale roughness.
It has been proved that, compared to spherical dextran particles, particles having a

corrugated shape show improved powder dispersibility [23, 24]. Powder dispersibility rises with the degree of surface corrugation [21]. This is of great significance in pharmaceutical industry, for instance, where an improvement of the dispersibility of cohesive inhalation powders is desirable.

A measure for the surface corrugation of a particle is the ratio of mass specific surface area $S_m[\mathrm{m}^2/\mathrm{g}]$, which can be determined by gas adsorption, and the volume specific surface area $S_V[\mathrm{m}^2/\mathrm{cm}^3]$, which can be measured by laser diffraction. The investigated dextran particles had a ratio of $S_m/S_V = 0.63\,\mathrm{cm}^3/\mathrm{g}$ (measured by Markus Wolkenhauer, Boehringer Ingelheim).

However, to determine particle diameters from the microscope images taken during the experiment, a spherical shape was approximated, since the corrugation is small compared to the error of diameter determination.

Particle density was measured by helium pycnometry (Boehringer Ingelheim).

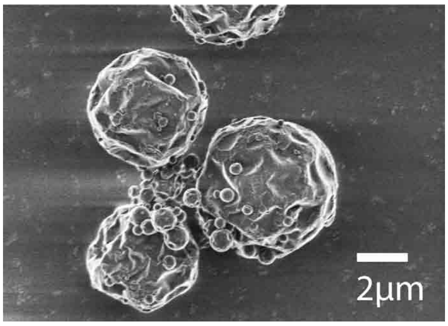

Figure 6.3: Dextran particles with corrugated shape (dextran T1:dextranT3.5 = 9:1) observed with SEM.

As sample surface a polished circular stainless steel plate (V2A 1.4301, 16 mm diameter, 2 mm thickness) with a polystyrene coating was used (molecular weight $M_W = 703\,200\,\mathrm{g/mol}$). The plate was provided with a hole in its center, which enables to screw it to the bar's end. Stainless steel was chosen since it is not only robust to stand the high accelerations with only small deformations, but also elastic enough to avoid brittle failure during the shock pulse. The polystyrene coating leads to a very smooth and well-defined surface, which can be characterized and modified rather easily. Additionally, polystyrene has a reduced surface energy compared to the bare steel, which facilitates particle detachment.

In this thesis adhesion measurements were performed with an untreated polystyrene layer, which is hydrophobic, and a polystyrene layer hydrophilized by oxygen plasma treatment (chapter 6.2.1).

Layer thickness and roughness were determined from AFM scans (chapters 6.3.2 and 6.3.3). The root mean square roughness r_{rms} was calculated for a scanning area of $1 \times 1\,\mu\mathrm{m}^2$.

For the measurements on the untreated polystyrene a layer with thickness of (18 ± 2) nm was used ($r_{rms} = (0.55 \pm 0.10)$ nm). However, for the experiments on the hydrophilized polystyrene a thicker layer was chosen (thickness (565 ± 16) nm) since plasma treatment removes several nanometers of the film [104]. Surface roughness did not change considerably after plasma treatment (before: $r_{rms} = (0.21 \pm 0.02)$ nm, after: $r_{rms} = (0.81 \pm 0.07)$ nm).

Generally, thinner films are preferable to avoid interference effects under the microscope causing illumination gradients which complicate image evaluation. Therefore, for all adhesion measurements on untreated polystyrene the 18 nm film was used.

To quantify the conditions during the experiment, temperature and relative humidity were measured with a hygrometer (custom-made device using a digital humidity and temperature sensor SHT15, Sensirion). All experiments were carried out under ambient conditions (temperature $20 - 25$°C, relative humidity $30 - 46\%$ in laboratory) in a dry lateral air stream with low flow rate ($10 - 50$ l/min, relative humidity $10 - 20\%$).

6.2 Sample Preparation

6.2.1 Preparation of the Substrate

The first step of the substrate preparation is a polish of the steel plate which had been ground planar before. This is necessary to obtain a smooth and optically flat surface, which is mandatory for a reliable optical detection of the particles. The substrate was polished in several steps using a polishing machine (Buehler Phoenix 4000) with different abrasive diamond suspensions (diamond particle sizes 9 µm, 3 µm, 1 µm) on different polishing cloths that were permanently rinsed with an oily lubricant.

Afterwards the polished steel surface was divided into easily recognizable sections by defined scratches using a thin needle. This ensures to quickly find the exact location of the investigated image section with the microscope system during the experiment.

The polished surface was subsequently cleaned with acetone and ethanol in an ultrasonic bath, dried with nitrogen and spin-coated with a polystyrene layer.

Spin-coating is widely used to deposit thin uniform films onto a flat substrate, for example in the microelectronics industry to manufacture photoresists [105, 106]. By pipetting, a small amount of diluted polymer solution is placed onto the substrate, which is spinning at a desired rotation rate. Excessive solution is ejected off the edges due to the centrifugal force and the remaining liquid forms the film. The layer thins due to the centrifugal force and solvent evaporation and then reaches its final thickness. The final average film thickness is independent of the volume of solution applied but increases with solution concentration and decreases with the rotation rate.

Polystyrene with high molecular weight ($M_W = 703\,200$ g/mol) was dissolved in toluene and spin-coated onto the polished steel substrate for $30 - 40$ s (SüssMicrotec spin coater).

Spin-coating of a 6 mg/ml solution at 1500 rpm led to a film thickness of (18 ± 2) nm, using a 6 wt% (weight percent) solution at 2000 rpm led to a thickness of (565 ± 16) nm (verified by AFM). The latter thickness was only chosen in case of a subsequent plasma treatment to hydrophilize the layer. For all other measurements the thinner 18 nm film was used. All investigated polystyrene layers had a very small surface roughness: their r_{rms} values were below 1 nm (chapter 6.1, measured with AFM).

Via spin-coating the layer thickness of a polymer film can be controlled with high reproducibility by solution concentration and rotation rate. Furthermore, resulting films are uniform, except at the edges where they are thicker due to retention of the solution [105]. Thus, all films which had been generated at a certain constant concentration and rotation rate are expected to have very similar thickness and also roughness.

In this thesis adhesion measurements were performed with untreated and hydrophilized polystyrene surfaces. The polystyrene was hydrophilized by O_2 plasma treatment (Femto plasma cleaner, Diener electronic) several hours prior to the experiment at a power of 10 W and an oxygen flow rate of 0.5 sccm for 36 s. Due to the oxygen plasma polar oxygen-containing functional groups are generated on the surface which increase the wettability. The wettability of the polystyrene layers was characterized by contact angle measurements (chapter 6.3.4).

6.2.2 Dispersing Particles on the Substrate

Particles were deposited onto the surface using a dispersing system (Figure 6.4) similar to commercially available dry powder dispersion units (e.g. Malvern Instruments Ltd).

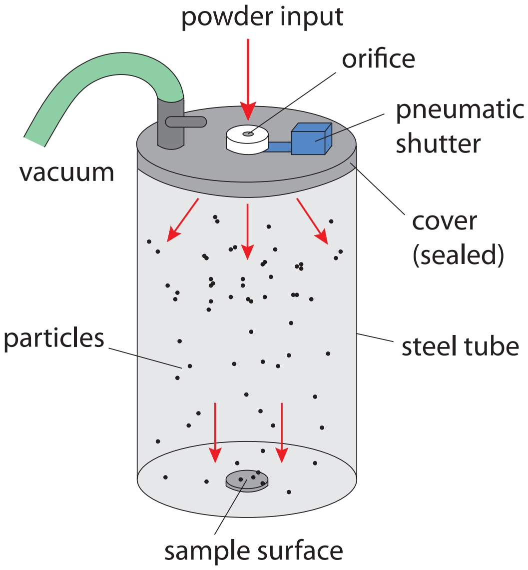

Figure 6.4: Dispersing system which is used to deposit separate individual particles on the sample surface.

The system consists of a sealed steel chamber in which the sample substrate is placed. After evacuation of the chamber using a vacuum pump (chemistry hybrid pump RC3, vacuubrand, $4 \cdot 10^{-4}$ mbar), a spatula tip full of powder is placed into a small funnel on top of a pneumatic shutter, that can be electronically controlled. When opening the shutter, particle agglomerates are efficiently dispersed by the shear stress of the inflowing air stream, leading to separate individual particles on the sample surface after sedimentation.

6.3 Sample Characterization

6.3.1 Scanning Electron Microscopy

In order to characterize the particle morphology, high-resolution scanning electron microscopy (SEM) was used. Images of the particles were recorded with a LEO 1530 Gemini instrument (Zeiss, Oberkochen, Germany) at low operating voltages ($0.7 - 3$ kV).
The sample in a vacuum chamber is scanned with an electron beam, which is emitted from a field emission cathode and focused by electromagnetic lenses. By detecting the secondary electrons, which are emitted due to the interaction of the electron beam with the sample, an SEM image can be obtained.
The recorded SEM images of the particles (taken by Lena Mammen) are shown in Figures 6.1 and 6.3.
Furthermore, SEM images of the spherical polystyrene particles were compared with microscope images recorded with the optical system, which was developed in this thesis. Comparison allowed to estimate the error of particle diameter determination from the microscope images (chapter 5.4.2).

6.3.2 Layer Thickness Measurements

The thickness of the polystyrene layer, which had been spin-coated onto the steel sample, was determined by AFM imaging in tapping mode (Dimension 3100, VEECO Instruments, Mannheim, Germany) using a silicon cantilever (OMLAC 160 TS-W2 silicon, back side Al coated, resonance frequency 300 kHz, spring constant 42 N/m, tip radius < 10 nm).
At first, a small part of the polystyrene layer was removed by scratching the surface with a thin copper wire. Copper was chosen to keep the deformation of the stainless steel as small as possible. Afterwards AFM scans of the transition zone between the polystyrene layer and the bare steel were performed on 2-4 different locations on the sample (scanning area between 6×6 and $10 \times 10\,\mu\text{m}^2$).
After leveling the data (program Gwyddion 2.25, http://gwyddion.net), for each scan 5-10 line profiles were chosen and from each of them a thickness was determined. This

was done by fitting a linear function to the polystyrene part and to the steel part (Figure 6.5) and afterwards averaging the minimum and maximum distance between the line fits. The final layer thickness of the film corresponds to the average of all thicknesses determined from the line profiles.

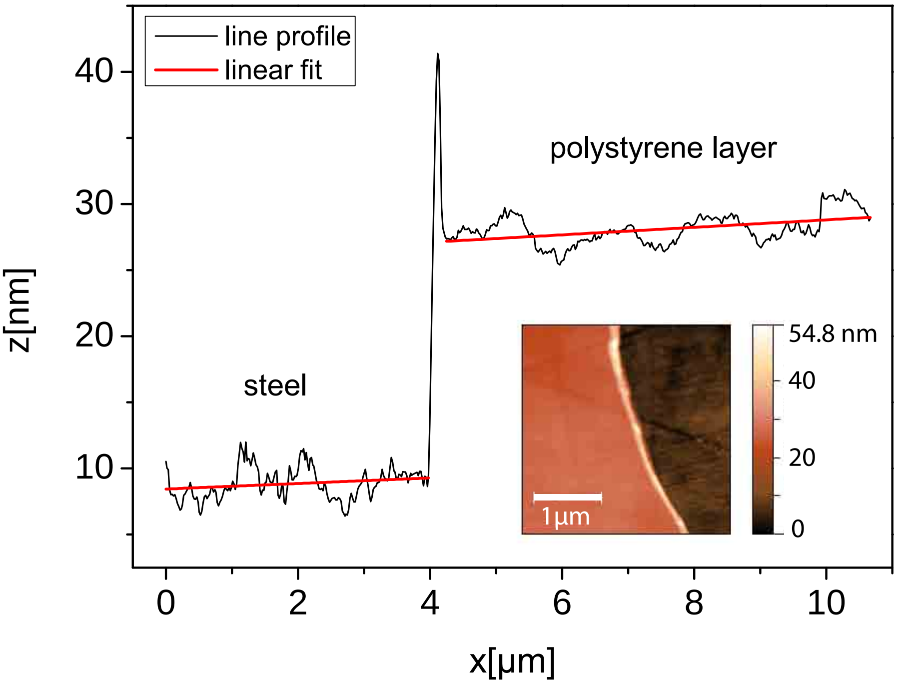

Figure 6.5: Determination of the layer thickness of the polystyrene film from a line profile of the transition zone between steel and polystyrene measured with AFM. x corresponds to the position in µm and z to the height in nm. The small image shows exemplarily a section of an AFM scan (height image). Averaging over several line profiles at different locations leads to the final value for the thickness.

In this work polystyrene films with a thickness of (18 ± 2) nm and (565 ± 16) nm were used (chapter 6.1). For the 18 nm film the order of magnitude of the thickness was confirmed by ellipsometry, where the change in polarization of a laser beam after reflection on the sample is measured (Nanofilm EP3SE ellipsometer, Accurion, laser wavelength $\lambda = 658$ nm). Here, a thickness of (24.6 ± 1.3) nm was obtained (measured by Walter Scholdei). Taking into account that the film is not ideally uniform the values from AFM and ellipsometry show good agreement.

However, the actual film thickness of the polystyrene has no influence on the adhesion force of particles, provided that the layer is thick enough that the van der Waals forces are dominated by the polystyrene and not by the metal underneath. This is the case for all used samples.

6.3.3 Roughness Measurements

Roughness of particles and substrates was characterized by AFM imaging (Dimension 3100, VEECO, tapping mode, OMLAC Silicon Al cantilever).
AFM scans were performed on 4-8 different locations on the polystyrene substrate and on several positions on 4-5 different polystyrene and silica particles, respectively (scanning area $1 \times 1\,\mu\text{m}^2$). To avoid rolling during an AFM scan, particles were glued to a glass substrate on a heating plate at 88°C prior to the measurement using a layer of epoxy resin (Epikote 1004 glue, Hexion, melting point around 90°C). The AFM images were measured on top of the particles.
From the $1 \times 1\,\mu\text{m}^2$ AFM scans the average root mean square roughness r_{rms} of the untreated 18 nm polystyrene film, the untreated 565 nm polystyrene film and the hydrophilized 565 nm polystyrene film was calculated (program NanoScope Analysis 1.40, Bruker). The calculation in the software is based on Equation 2.54. All images were flattened (first order) before calculating the r_{rms} values to subtract any sample tilt.
For the polystyrene and silica particles the average root mean square roughness was calculated as well. Here, all images were provided with a third order flattening before the calculation to remove the spherical curvature from the height data. All results are presented in chapter 6.1. They all refer to a scanning area of $1 \times 1\,\mu\text{m}^2$. The error Δr_{rms} is given by the standard deviation.

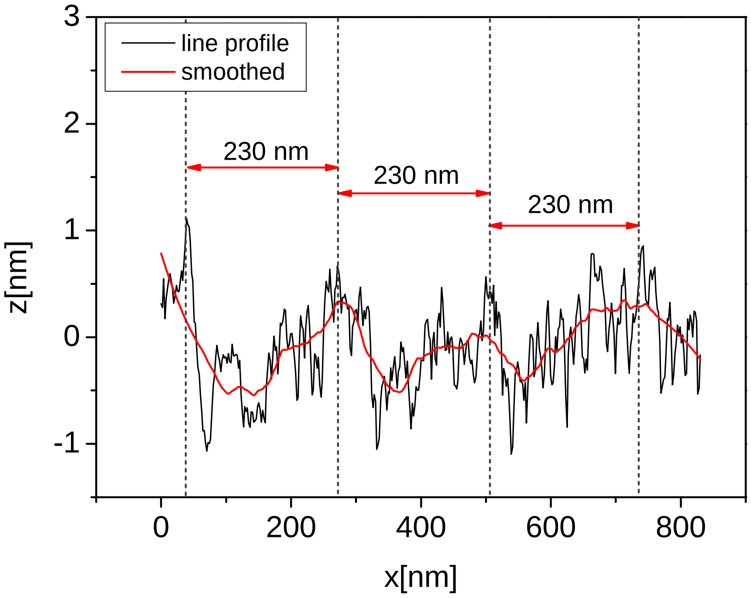

Figure 6.6: Determination of the lateral distance λ between two asperities of the polystyrene substrate from a line profile of the surface measured with AFM. x corresponds to the position in nm and z to the height in nm. In this example $\lambda \approx 230\,\text{nm}$. Averaging over 24 line profiles leads to the final value for λ.

Roughness parameters are important in order to compare the experimentally determined adhesion forces between particles and substrate with theoretical predictions from the Rabinovich approach (chapter 2.4.5). Here, the root mean square roughness of the total particle-surface system has to be considered. Assuming an independent statistical combination of the two contact surfaces the r_{rms} value for the total system is given by

$$r_{rms} = \sqrt{r_{rms}^2(\text{particle}) + r_{rms}^2(\text{substrate})} \tag{6.1}$$

Another important parameter needed for the Rabinovich model is the lateral distance λ between two asperities. The average λ was calculated for the untreated 18 nm polystyrene film. For 6 AFM scans at different locations on the polystyrene surface two horizontal and two vertical image sections were chosen. From each of these 24 line profiles a lateral distance between two asperities (Figure 6.6) was determined according to [17] after smoothing the graphs (OriginPro 8.5.0G SR1, OriginLab corporation). Averaging all values led to a lateral distance between asperities of $\lambda = (214 \pm 48)$ nm for the untreated polystyrene surface. The error is given by the standard deviation. The experimentally determined roughness parameters are later included in the Rabinovich model (chapter 8).

6.3.4 Contact Angle Measurements

In order to characterize the wettability of the polystyrene layers that had been spin-coated onto the steel plates, static water contact angles were measured with the sessile drop method using a contact angle meter DSA 10 (Krüss GmbH, Germany).

A small droplet of water (drop volume $1-3$ µl) was gently placed with a capillary needle on top of the horizontal substrate and illuminated by a light source. Imaging the drop laterally with a microscope enabled to determine the static contact angle from the drop shape. After removing the needle from the drop a microscope image was taken from which the contact angle was determined. This was repeated for 4-5 drops on several locations of the polystyrene surface to obtain an average contact angle.

Water on the hydrophilized polystyrene layer had an average static contact angle of $(18 \pm 2)^\circ$ compared to $(99 \pm 1)^\circ$ for the untreated polystyrene.

6.4 Shock Pulse Transfer

To enable adhesion measurements with the Hopkinson bar device developed in this work, a reproducible shock pulse transfer from the bar to the sample plate with minimum acceleration loss is mandatory. To attach the steel plate to the bar's end a screw is used. In order to quantify the pulse transfer, several shock pulses were excited at constant distance between projectile and bar (number of motorsteps 20 000). During each pulse the acceleration was measured either directly at the bar's end (without sample) or on the sample plate at the overlapping edges at different positions. Figure 6.7 shows the maximum value of the first positive peak in the measured acceleration signal for several consecutive shock pulses (measurement number) using a simple steel screw (left) and a custom-made titanium screw (right). The head size of the titanium screw was 10 mm corresponding to the bar thickness. While with the steel screw large variations of the acceleration signal and a high loss of acceleration on the sample are observed, attachment with the titanium screw leads to a stable signal and a much better acceleration transfer. In some cases the steel screw even loosened after few pulses, whereas the titanium screw remained tightened. Moreover, fixing the titanium screw with a torque wrench provides a reproducible torsional moment.

Therefore, in order to optimize the coupling, the sample plate is attached to the bar's end using a titanium screw that is fixed with a torque wrench at 3.5 Nm for each experiment. Thus, a stable signal without considerable loss in acceleration on the sample is obtained.

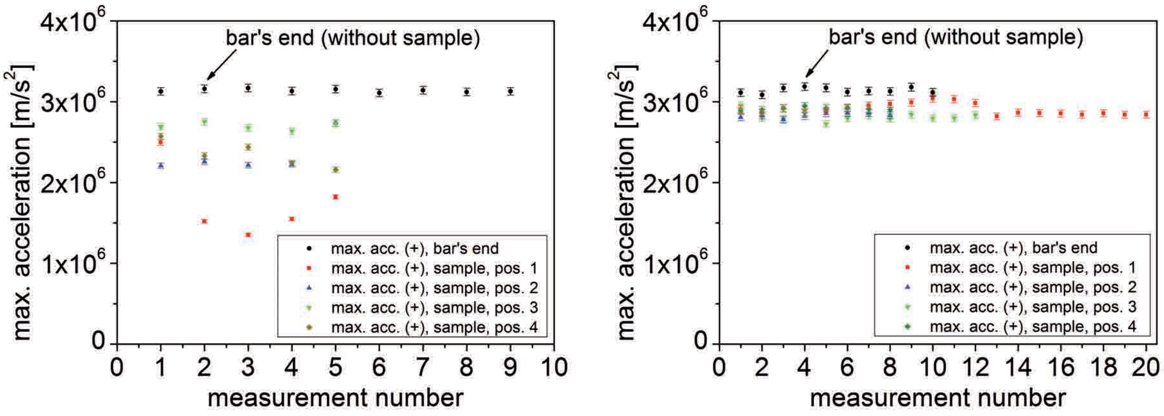

Figure 6.7: Shock pulse transfer from the bar to the sample plate using a steel screw (left) and a titanium screw (right). The black data points show the maximum acceleration (positive) measured directly at the bar's end during several shock pulses with constant distance between projectile and bar. The colored data points show the maximum acceleration (positive) on the sample plate measured at the overlapping edges at different positions. Titanium screw and torque wrench provide a stable and reproducible signal.

7 Colloidal Probe Measurements

In order to compare the Hopkinson bar measurements with measurements obtained from an established method, adhesion forces of particles were determined with the colloidal probe technique. In this chapter it is explained how the colloidal probes were prepared in this work. Furthermore, the measurement of force-versus-distance curves as well as the subsequent data evaluation to obtain adhesion forces are described.

7.1 Colloidal Probe Preparation

Polystyrene microspheres (polystyrene DVB, Duke Scientific Corp.) with diameters in a range of $6 - 13\,\mu\text{m}$ were attached to tipless cantilevers (μmasch, NSC12 tipless noAl, spring constant $5 - 12\,\text{N/m}$ and BudgetSensors, AIO-TL, spring constant $1 - 29\,\text{N/m}$) with two component epoxy glue (UHU Plus Endfest 300). This was done under control of an optical microscope (Zeiss, with objectives Epiplan 10× and 50×) using a micromanipulator (Narishige Co. Ltd, Japan).

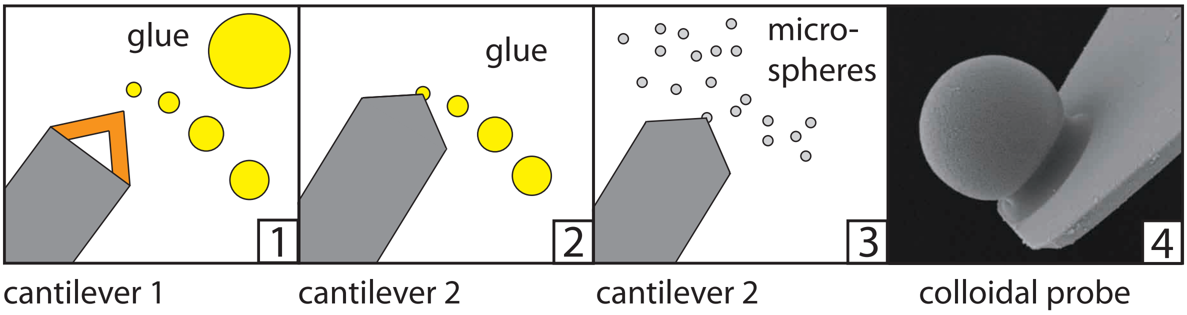

Figure 7.1: Preparation steps 1-4 to produce a colloidal probe.

To avoid contamination of the particles they were washed with distilled water in a centrifuge prior to attachment. In order to obtain separate individual spheres the suspension was then spin-coated onto a clean glass slide, which was placed under the microscope. Afterwards a small drop of glue was deposited onto a second glass slide. A cantilever was brought into contact with the glue under the microscope to pick up a tiny amount using the micromanipulator. By touching the glass slide several times with the cantilever, very small glue droplets were generated (Figure 7.1, step 1). After that, the first cantilever was exchanged by a second one, to which a particle should be attached. This was achieved by first touching a tiny glue dot with the cantilever end on the first glass slide (Figure 7.1, step 2) and afterwards picking up a polystyrene particle on the second glass slide (Figure 7.1, step 3). This way, a colloidal probe was obtained (Figure 7.1, step 4, example SEM image).

In this work 7 colloidal probes with different sphere diameters were prepared: a 6 µm probe, two 7 µm probes, a 10 µm probe, an 11 µm probe and two 13 µm probes (±0.5 µm). Diameters were determined by optical microscopy.

Spring constants of the cantilevers were measured with the thermal noise method [72] (MultiMode TUNA TR, VEECO, chapter 3.1.3). They were in a range of $3 - 15\,\mathrm{N/m}$, which agrees well with the range given by the manufacturers. The error of cantilever spring constants determined with the thermal noise method is in the order of 10% [107].

7.2 Adhesion Force Measurements

Colloidal probe measurements with the prepared probes ($6 - 13\,\mu\mathrm{m}$) were performed with AFM (VEECO Dimension 3100) on the untreated polystyrene coated steel substrate which is also used for the Hopkinson bar measurements (polystyrene layer thickness $(18 \pm 2)\,\mathrm{nm}$, root mean square roughness $r_{rms} = (0.55 \pm 0.10)\,\mathrm{nm}$).

The measured raw signal is the detector signal in volts versus the piezo position. The obtained curves can later be converted into force-versus-distance curves, from which the adhesion force can be determined. For each colloidal probe, 80-100 curves were recorded on 8-15 different locations on the polystyrene surface.

After the measurements it was checked for each colloidal probe with the optical microscope if the particle still adhered to the cantilever and if the particle was still optically clean.

7.3 Data Evaluation

The recorded raw curves were evaluated with a LabView program (Force Curve Analysis, written by Michael Kappl, Max Planck Institute for Polymer Research, using LabView, National Instruments). First, all 80-100 curves measured at a certain location on the sample with a certain colloidal probe, were calibrated. With the spring constant of each cantilever and by fitting a line to the zero force region and the constant compliance region, all raw curves were converted into force-versus-distance curves (according to chapter 3.1.3). For each force-versus-distance curve the minimum, corresponding to the adhesion force, was determined. The average over all 80-100 curves gives the final adhesion force of the used colloidal probe at a certain location. The adhesion force error is given by the standard deviation.

8 Results and Discussion

With the new developed Hopkinson bar device adhesion measurements of a variety of different particles were performed, which are presented and also discussed in this chapter. In order to validate the new method, measured adhesion forces of spherical particles with well known surface chemistry were compared with theoretical predictions and measurements using an established method, the colloidal probe technique. Afterwards, more complex particles, which are relevant for example in pharmaceutical industry, were investigated with the new device in order to demonstrate that the Hopkinson bar system can be used to study a broad range of particle-surface combinations.

8.1 Polystyrene Particles

8.1.1 Hopkinson Bar Measurements

Adhesion measurements with the Hopkinson bar system were carried out with spherical polydisperse polystyrene particles on a polystyrene coated steel surface (untreated). Figure 8.1 shows an example microscope image taken during the experiment (zoom setting 1×). For better overview, brightness and contrast were enhanced and a sharpening filter was employed. Images were taken at two adjacent locations on the sample.

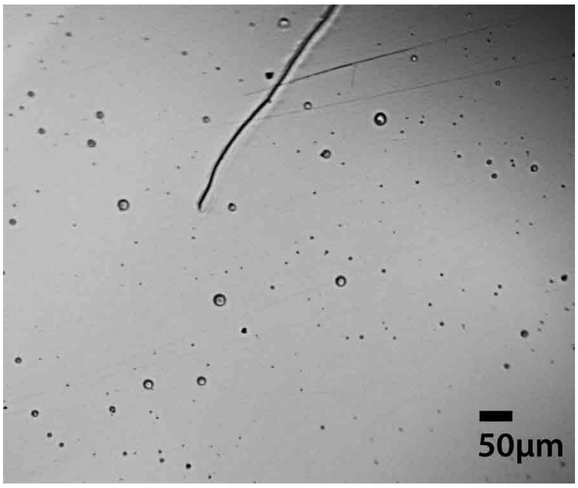

Figure 8.1: Microscope image of polydisperse spherical polystyrene particles on a polystyrene coated surface taken during the experiment.

The results for particles in a diameter range of 4 – 10 µm are shown in Figure 8.2, where the adhesion force is plotted versus particle diameter.

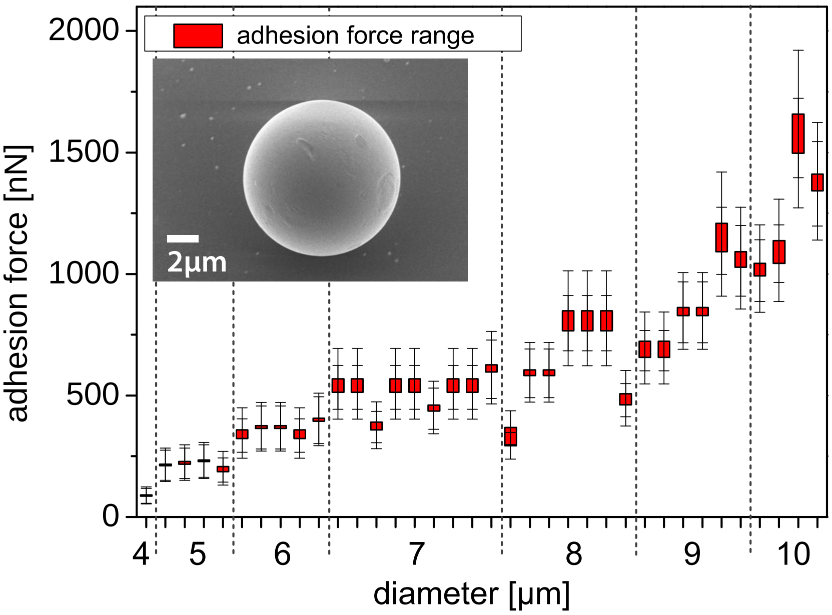

Figure 8.2: Adhesion forces (red ranges) of spherical polystyrene particles on a polystyrene coated surface measured with the Hopkinson bar. Each red adhesion range represents a different single particle which detached during the experiment (particle diameter 4 – 10 µm).

During this experiment, relative humidity and temperature in the laboratory were (45 ± 2)% and (25 ± 1)°C respectively. However, since the sample was exposed to an air flow for horizontal dislocation of detached particles (flow rate (10 ± 1) l/min, measured in the tube), it experienced the humidity of the air stream of about 20%. Adhesion values of 51 particles in total could be obtained with this experiment.

Since the acceleration on the sample is increased in discrete steps, one obtains an adhesion force range for each detached particle. The lower limit of that range corresponds to the last shock pulse where the particle still adhered; the upper limit corresponds to the pulse after which the particle was detached. Each adhesion range in Figure 8.2 corresponds to a different single particle with a specific diameter that detached during the measurement. In this particular experiment one particle was detected with a diameter of 4 µm, 4 particles with a diameter of 5 µm etc.

The error bars resulted from the combined error of the laser Doppler vibrometer (measuring inaccuracy 1, 5%) and the error in determination of particle radius ($\Delta R_P = \pm 0.5$ µm) according to Equation 5.7. For some of the particles, accelerations higher than the measurement range of the vibrometer were used, which had been determined from the calibration plot. In this case the error for the acceleration values corresponds to the shock

pulse reproducibility of 5%. For better overview, error bars in x-direction are left out.
Since polystyrene is hydrophobic and the particles in the set-up are exposed to an air stream with relatively low humidity, particle adhesion force is here mainly caused by van der Waals forces, whereas capillary forces are expected to play a negligible role.
The measured adhesion forces in Figure 8.2 show a clear increase with particle diameter from $(88 \pm 3)\,\mathrm{nN}$ for the $4\,\mu\mathrm{m}$ particle to $(1578 \pm 114)\,\mathrm{nN}$, which is the largest measured force for the $10\,\mu\mathrm{m}$ particles (mean values of upper and lower limit of the adhesion range).
However, as expected, even particles of the same diameter can show relatively large variations in their adhesion force. Here, the $8\,\mu\mathrm{m}$ sized particles, for instance, show variations in a range of about $500\,\mathrm{nN}$, corresponding to a factor of two approximately. This is a fundamental property of the adhesion forces, which is caused by surface roughness and surface heterogeneity [17–20]. The adhesion between a particle and a flat surface strongly depends on the precise location of contact, i.e. the nanoscale roughness and the exact chemical composition and molecular structure. The nanoscale roughness can cause a significant change in contact area and effective distance between the contacting surfaces. Furthermore, surface heterogeneities can change the adhesion energy. Both effects have a substantial influence on the adhesion force resulting in a force distribution rather than a single value, even for identically sized spherical particles.

8.1.2 Comparison with Theoretical Predictions

JKR model

Experimentally determined adhesion forces of the polystyrene particles with the Hopkinson bar device were compared with predictions from theoretical models. At first, theoretical values for the adhesion force of polystyrene spheres on a flat polystyrene surface depending on their radius R_P were calculated with the JKR model according to $F_{adh} = 3\pi\gamma^S R_P$ (Equation 2.44). As surface energy a value of $\gamma^S = 30\,\mathrm{mJ/m^2}$ was assumed. The theoretically predicted forces with the JKR model are plotted as black line in Figure 8.4.
The JKR model predicts a linear increase of the adhesion force with particle diameter. For the smaller particles (about $4 - 7\,\mu\mathrm{m}$) this trend can be observed qualitatively for the measured values as well. However, for the larger particles there seems to be stronger increase of the adhesion, which will be discussed later.
Furthermore, the JKR model overestimates the adhesion forces, presumably since perfectly smooth and chemically homogeneous surfaces are assumed. However, in reality surface roughness of particles and substrate leads to a considerable reduction of adhesion, which is not considered in the model.

Rabinovich Approach

In order to take the roughness influence into account adhesion forces were calculated using the Rabinovich approach.

A_H [J]	D_0 [nm]	r_{rms}(particle) [nm]	r_{rms}(substrate) [nm]	λ [nm]
$6.6 \cdot 10^{-20}$	0.17	0.57 ± 0.06	0.55 ± 0.10	214 ± 48

Table 8.1: Parameters to calculate adhesion forces of polystyrene particles on a polystyrene surface in air with the Rabinovich model: Hamaker constant A_H of the polystyrene-air-polystyrene combination, distance of closest approach between surfaces D_0, r_{rms} values of particle and substrate and the lateral distance between asperities λ.

To characterize surface roughness, AFM scans of the polystyrene particles and the polystyrene substrate were performed (Figure 8.3), from which the root mean square roughness r_{rms} (scanning area $1 \times 1\,\mu m^2$) and the lateral distance λ between two asperities were determined. The r_{rms} value of the particle-surface combination is given by Equation 6.1. The metal underneath the polystyrene film (thickness (18 ± 2) nm) has no considerable influence on the adhesive force of a particle, since the distance is too large.

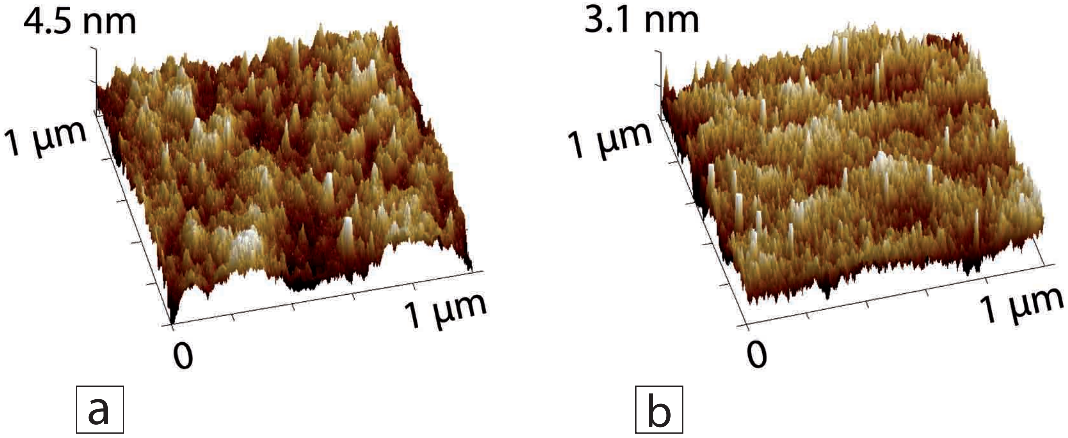

Figure 8.3: Example AFM height images of one of the used polystyrene particles (a) and the polystyrene surface (b) which was spin-coated onto the steel sample ($1 \times 1\,\mu m^2$ scanning area). It should be noted that the x and y axis are scaled in µm whereas the z axis is scaled in nm. Both images have different height scales to better distinguish the colors in each image. From several AFM scans roughness parameters needed for the Rabinovich model were obtained.

An upper and a lower limit of the theoretical adhesion force were calculated with the Rabinovich approach of Equation 2.53. For the lower adhesion limit, the maximum value of r_{rms} for the particle-surface combination was used, employing the upper error limits of r_{rms}(particle) and r_{rms}(substrate), as well as the minimum value of λ, which is the lower error limit of λ. For the upper adhesion limit, the minimum value for r_{rms} and the maximum value for λ were used. All employed parameters for the calculation are shown in Table 8.1.

The theoretical adhesion force range of the used polystyrene particles on the polystyrene surface calculated with the Rabinovich approach is plotted versus particle diameter in Figure 8.4 (green range) in comparison with the experimental data.

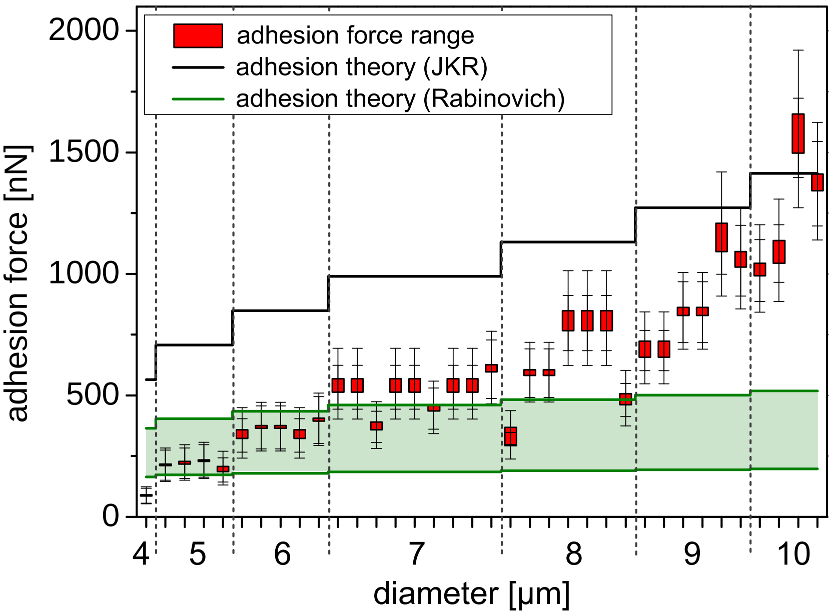

Figure 8.4: Adhesion forces (red ranges) of polystyrene particles on a polystyrene coated surface measured with the Hopkinson bar in comparison with theoretical values from JKR model (black line) and Rabinovich approach (green range). Each red adhesion range represents a different single particle (particle diameter 4 – 10 µm).

For the smaller particle sizes (5 – 6 µm) the measured adhesion force values are within the determined range according to Rabinovich. However, for larger particles (8 – 10 µm) the increase of adhesion with increasing particle diameter is stronger than theoretically predicted by the Rabinovich model and a deviation from the determined range can be observed. This trend was confirmed in several experiments using polystyrene particles but also for the silica particles (chapter 8.2.2).

The reason for the steeper increase of adhesion in the case of larger particles might be that roughness and heterogeneity influence the adhesion of small and large particles differently. A possible explanation is the following: A large particle in the Hopkinson bar set-up may be able to roll and adjust when it is deposited on the surface and during a

shock pulse (without noticeably changing its location on the surface), since its inertia is high enough to overcome rolling friction (Figure 8.5b). This rearrangement usually leads to more and stronger nanocontacts and thus to a higher adhesion force due to the larger contact area. Since rearrangement effects are not considered in the Rabinovich model, a deviation of adhesion values from theory is observed for larger particles. For smaller particles in the Hopkinson bar set-up the situation is different: since its inertia is too weak to overcome rolling friction, a small particle cannot rearrange on the surface during deposition or a shock pulse and presumably remains at the point of first contact kept in position, e.g. by van der Waals forces. Thus, it typically only attaches to the first asperity (Figure 8.5a). This is similar to the situation considered in the Rabinovich model, thus an agreement of experiment and theory is observed.
Besides, an increasing plastic flattening of the micro-asperities of a particle with increasing diameter may play an additional role, leading to a larger contact area and thus to higher adhesion for larger particles. This effect is neither considered in the Rabinovich model.

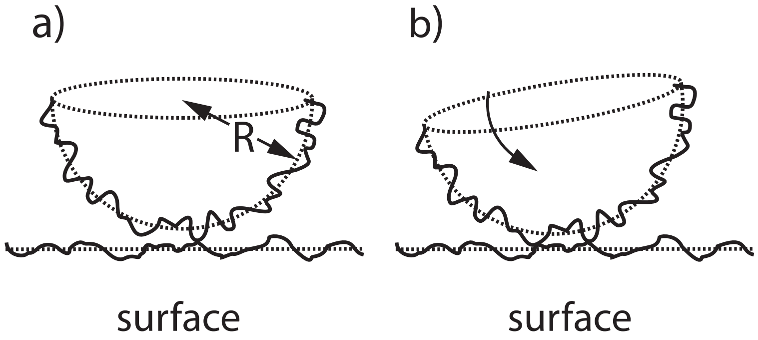

Figure 8.5: (a) A small particle in the Hopkinson bar set-up cannot rearrange and therefore remains at the point of first contact, typically attached only to the first asperity. This corresponds to the situation in AFM, where the direction of contact is predetermined. (b) A large particle in the Hopkinson bar set-up may still be able to move on the surface and adjust, leading to a larger contact area and therefore to stronger adhesion.

8.1.3 Comparison with Colloidal Probe Measurements

Comparative measurements with the colloidal probe technique using 7 probes with polystyrene particles of 6 µm, 7 µm, 10 µm, 11 µm and 13 µm in diameter are shown in Figure 8.6. The adhesion values were measured at 8-15 locations on the polystyrene surface (black symbols) under ambient conditions. Each data point corresponds to a mean value of about 80-100 force curves measured at this location, whereas each symbol represents one colloidal probe. The error is given by the standard deviation.

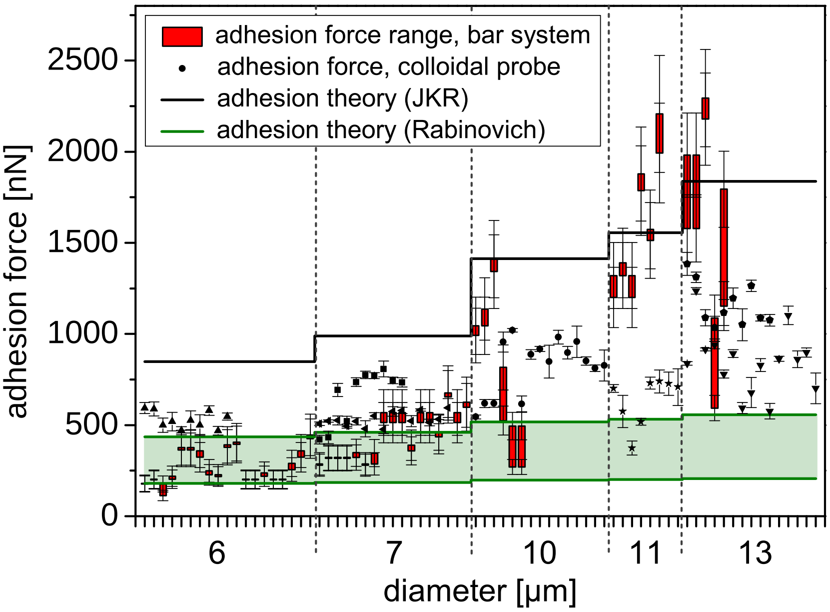

Figure 8.6: Comparison of adhesion forces measured with the Hopkinson bar system (red ranges), measured with the colloidal probe technique (black symbols) and determined theoretically with JKR model (black line) and Rabinovich model (green range).

The adhesion forces measured with the Hopkinson bar device (red ranges) stem from two different experiments using polystyrene particles on a polystyrene surface.
The colloidal probe measurements show good agreement with the adhesion values measured with the Hopkinson bar up to a particle diameter of about $7 - 10\,\mu\text{m}$. For larger diameters adhesion forces measured with the bar system tend to higher adhesion forces than those measured with colloidal probe.
The reason for this deviation might be the same as for the deviation from Rabinovich theory, namely an effect of the nanoscale roughness of particle and surface. A possible explanation is the following: For a colloidal probe in AFM the orientation of the particle and therefore the direction of contact is predetermined, meaning that the particle cannot adjust freely (Figure 8.5a). However, in the case of the Hopkinson bar, a particle may

still be able to rotate and rearrange when it is deposited on the surface and during a shock pulse, if its inertia is high enough to overcome rolling friction. This is the case for larger particles (Figure 8.5b) and may lead to more and stronger nanocontacts and thus to a stronger adhesion force. Hence, for larger particles adhesion forces measured with the Hopkinson bar system are higher compared to those measured with the colloidal probe technique. Small particles in the Hopkinson bar set-up probably remain at the point of first contact kept in position e.g. by van der Waals forces, since their inertia is too weak to overcome rolling friction. As a consequence, they only attach to the first asperity. This is also the case for a particle glued to a cantilever in the colloidal probe technique (Figure 8.5a). As a consequence, for small particles the adhesion forces measured with the bar system agree well with those obtained from colloidal probe measurements. The reason why the colloidal probe values are slightly higher than predicted by the Rabinovich model (green range in Figure 8.6) might be a plastic flattening of the micro-asperities caused by the applied load onto the particle during the measurement in AFM. This is not taken into account in the theory. However, this probable flattening effect in AFM seems to have a much smaller impact on the adhesion than the rearrangement effect in the Hopkinson bar system for larger particles.

8.1.4 Summary: Polystyrene Particles

Adhesion forces of spherical polystyrene particles (diameters $4-13\,\mu\text{m}$) on a polystyrene coated surface under ambient conditions were measured using the Hopkinson bar device and subsequently compared with theoretical predictions from JKR model and Rabinovich approach. JKR model underestimates the adhesion forces, presumably since the nanoscale roughness of particles and surface is not considered.

Comparison with the Rabinovich approach, where roughness is taken into account, shows an agreement for smaller particles. However, for larger particles a steeper increase of the adhesion force with diameter is observed than theoretically predicted. For small particles, adhesion forces measured with the bar system also agree well with results obtained from the colloidal probe technique. For larger particles, adhesion values measured with the Hopkinson bar are higher than measured with colloidal probe.

Surface roughness can be considered to be a possible reason for this effect: reorientation of large particles in the bar set-up may lead to higher adhesion due to contact area maximization, whereas for a colloidal probe the contact is predetermined. Rearrangement is furthermore not considered in the Rabinovich model. This leads to a deviation of the adhesion of larger particles measured with the Hopkinson bar from colloidal probe measurements and theory. In contrast, small particles in the Hopkinson bar set-up are expected to maintain their initial position being not able to readjust, which corresponds to the situation of a colloidal probe and is similar to the situation considered in the Rabinovich model.

8.2 Silica Particles

8.2.1 Hopkinson Bar Measurements on untreated Polystyrene Surface

Adhesion forces of spherical porous silica particles (diameters $4-7\,\mu m$) on a polystyrene surface (untreated) were measured with the Hopkinson bar set-up. Figure 8.7 shows an example microscope image taken during the experiment (zoom setting 1×). Brightness and contrast were enhanced and a sharpening filter was employed for better overview.

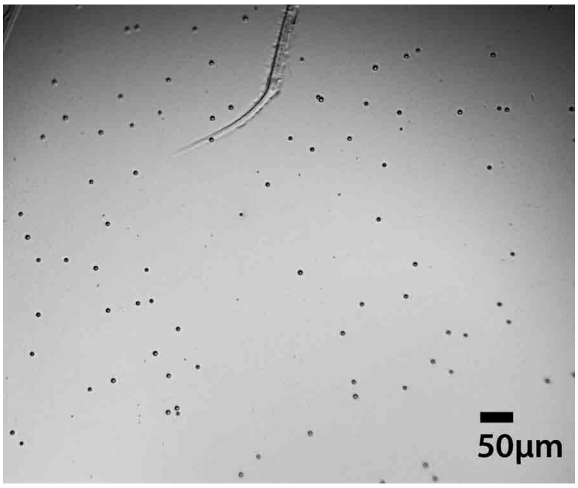

Figure 8.7: Microscope image of spherical silica particles (diameters $4-7\,\mu m$) on a polystyrene coated surface taken during the experiment.

The results are shown in Figure 8.8, where the adhesion is plotted versus particle diameter. During the experiment, relative humidity and temperature in the laboratory were $(38 \pm 2)\%$ and $(23 \pm 2)°C$, respectively. The air flow, which the sample was exposed to, had a flow rate of $(51 \pm 1)\,l/min$ and a relative humidity of about 20%. Adhesion values of 64 particles in total could be obtained with this experiment.

The measured adhesion forces show an increase with particle diameter from $(26 \pm 3)\,nN$, which is the smallest measured force for the $4\,\mu m$ particles, to $(140 \pm 16)\,nN$, which is the largest measured force for the $7\,\mu m$ particles (mean values of upper and lower adhesion limits). Compared to the polystyrene particles in chapter 8.1, the adhesion values of the porous silica particles are about a factor 3 lower. The main reason is probably the higher surface roughness of the silica particles: the r_{rms} value of the silica particles (referred to an area of $1 \times 1\mu m^2$) is about 8 times higher than the r_{rms} value of the polystyrene particles.

Also in this measurement, variations of the adhesion force of particles with identical diameters can be observed, obviously caused by local surface roughness and heterogeneity effects.

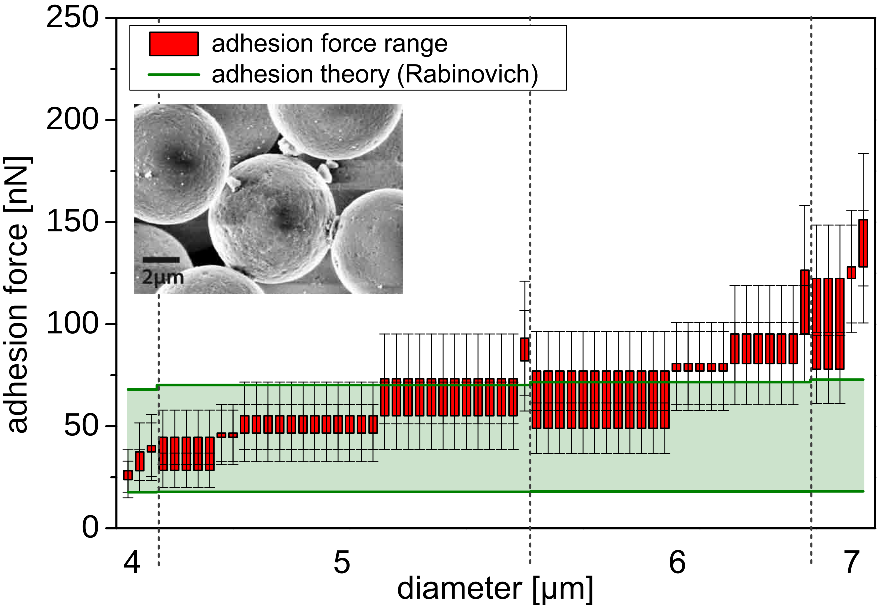

Figure 8.8: Adhesion forces (red ranges) of spherical porous silica particles ($4 - 7\,\mu\text{m}$) on a polystyrene surface measured with the Hopkinson bar system in comparison with theoretical values from the Rabinovich approach (green range). Each adhesion range represents a different single particle.

8.2.2 Comparison with Rabinovich Approach

Measured adhesion forces of silica particles on polystyrene were compared with theoretical predictions from the Rabinovich approach (green region in Figure 8.8).
Roughness parameters (Table 8.2) were determined from several AFM scans of the polystyrene surface (Figure 8.3b) and the silica particles (Figure 8.9, $1 \times 1\,\mu\text{m}^2$ scanning area) in order to calculate an upper and a lower theoretical adhesion limit.

A_H [J]	D_0 [nm]	r_{rms}(particle) [nm]	r_{rms}(substrate) [nm]	λ [nm]
$4 \cdot 10^{-20}$	0.17	4.67 ± 1.27	0.55 ± 0.10	214 ± 48

Table 8.2: Parameters to calculate adhesion forces of silica particles on a polystyrene surface in air with the Rabinovich model: Hamaker constant A_H of the silica-air-polystyrene combination (scaled down), distance of closest approach between surfaces D_0, r_{rms} values of particle and substrate and the lateral distance between asperities λ.

Since porous silica with a low density was used ($0.738\,\text{g/cm}^3$ compared to $2.2\,\text{g/cm}^3$ for standard silica), the Hamaker constant of the silica-air-polystyrene combination,

$A_H = 12 \cdot 10^{-20}$ J, was scaled down according to $A_H \propto \rho$ (Table 8.2).
Comparison of the measured forces of the silica particles on the polystyrene surface with the theory values (Figure 8.8) shows very good agreement for the smaller particles ($4 - 5\,\mu$m). However, again larger particles ($6 - 7\,\mu$m) exhibit slightly higher adhesion force values than expected from the Rabinovich model. This is the same trend as measured for the polystyrene particles.
A possible reason for this stronger increase of adhesion in the case of larger particles is that roughness might influence small and large particles differently in the Hopkinson bar set-up, as already discussed in chapter 8.1.2. At which diameter the deviation from theory, i.e. the overcoming of rolling friction and subsequent reorientation of a particle starts, seems to depend on the particular particle-surface combination as well as on the individual particle and its location on the surface. For the investigated polystyrene particles, the deviation starts at a diameter of about $7 - 8\,\mu$m, for the silica particles of about $6\,\mu$m. Due to statistical variations of the adhesion force an exact diameter cannot be stated.

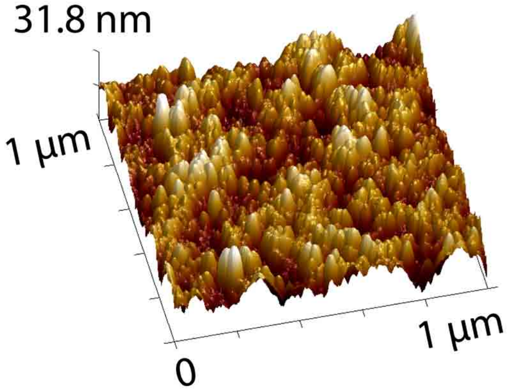

Figure 8.9: Example AFM height image of one of the used silica particles ($1 \times 1\,\mu\text{m}^2$ scanning area). It should be noted that the x and y axis are scaled in µm whereas the z axis is scaled in nm. Here, the height scale is roughly 10 times larger than in Figure 8.3. From several AFM scans of particles and the polystyrene substrate roughness parameters needed for the Rabinovich model were obtained.

8.2.3 Hopkinson Bar Measurements on hydrophilic Polystyrene Surface

Adhesion forces of spherical porous silica particles (diameters $4 - 7\,\mu$m) were also measured on a hydrophilized polystyrene surface using the Hopkinson bar device. During this experiment relative humidity and temperature in the laboratory were $(37 \pm 2)\%$ and (24 ± 1)°C respectively. The air stream had a flow rate of $(30 \pm 1)\,$l/min and a relative humidity of about 20%. The zoom setting in the optical system was 1×. With this experiment, adhesion values of 104 particles in total could be obtained. Figure 8.10 shows the measured forces on the hydrophilic polystyrene surface in comparison with the forces measured on the untreated polystyrene surface, which is hydrophobic.

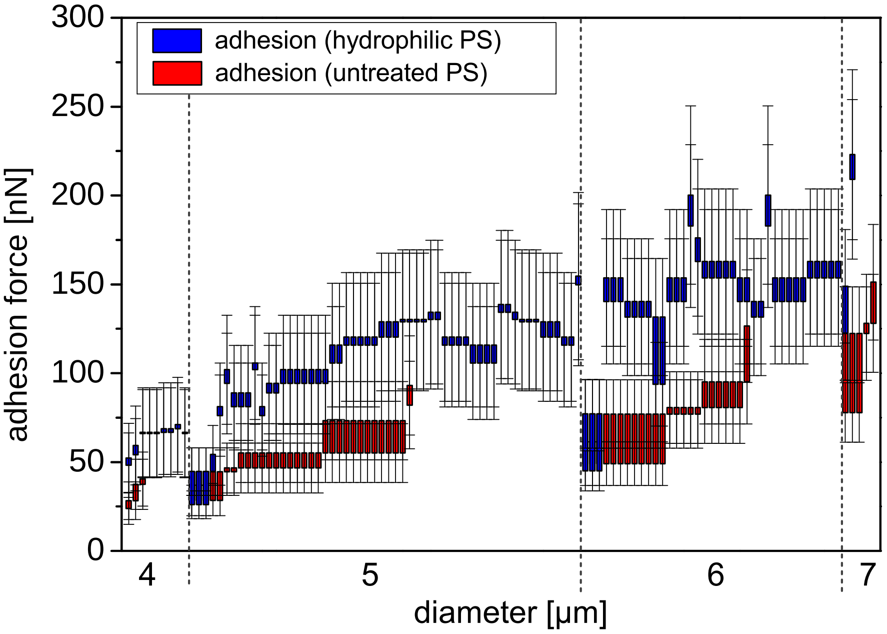

Figure 8.10: Adhesion forces of spherical silica particles ($4 - 7\,\mu\mathrm{m}$) on a hydrophilized (blue ranges) and an untreated (red ranges) polystyrene surface measured with the Hopkinson bar system. Each adhesion range represents a different single particle.

The surface roughness of the untreated and the hydrophilized polystyrene layer was nearly identical, which was verified by AFM measurements (chapter 6.1). Therefore, the roughness influence on the adhesion should be the same for both experiments and differences in the adhesion can be directly related to the difference in wettability of the surfaces.

	$\overline{F}_{adh}$ [nN] (4 µm)	$\overline{F}_{adh}$ [nN] (5 µm)	$\overline{F}_{adh}$ [nN] (6 µm)
untreated polystyrene	33 ± 6	54 ± 12	75 ± 13
hydrophilic polystyrene	64 ± 6	109 ± 25	142 ± 29

Table 8.3: Average adhesion force of 4 µm, 5 µm and 6 µm sized porous silica spheres on the untreated and the hydrophilized polystyrene surface measured with the Hopkinson bar system.

Table 8.3 gives an overview of the average adhesion forces of the 4 µm, 5 µm and 6 µm sized silica particles on untreated and hydrophilized polystyrene. The forces were cal-

culated from the mean values of minimum and maximum adhesion measured for each detached particle.
Comparing adhesion values of particles on the hydrophilized and the untreated polystyrene surface shows higher adhesion forces for the hydrophilic surface (roughly a factor of 2). This is expected since the surface energy of the hydrophilic surface should be higher [47]. In addition, capillary forces are expected to contribute on the hydrophilic surface due to the higher wettability, albeit to a small extent because of the low relative humidity.
Theoretical values with the Rabinovich approach were not calculated for the measurement on the hydrophilic polystyrene surface. One reason is that the hydrophilization changes the Hamaker constant of the polystyrene and it is not known to which extent. Moreover, since the Rabinovich approach describes van der Waals forces without considering capillary forces it can only give reasonable predictions for adhesion on the untreated polystyrene surface, where capillary forces play a negligible role.

8.2.4 Statistical Evaluation: Small Silica Particles

Measurements with the Hopkinson bar system were also conducted with smaller porous silica particles (spherical, average diameter 3.5 µm, manufacturer's information) on an untreated polystyrene surface. Here, a higher zoom-in of the optical system was used in order to determine the particle diameters more precisely (zoom setting 1.5×). In Figure 8.11 an example microscope image which was taken during the experiment is shown. For better overview brightness and contrast were enhanced and a sharpening filter was employed.

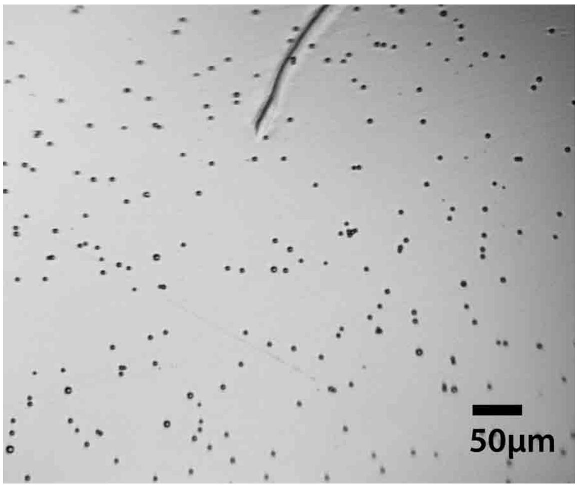

Figure 8.11: Microscope image of spherical silica particles (diameters 3−6 µm) on a polystyrene coated surface taken during the experiment. Here, a higher magnification was used.

In this experiment relative humidity and temperature in the laboratory were $(36 \pm 2)\%$ and $(24 \pm 1)^{\circ}$C, respectively, with a flow rate of the air stream of $(52 \pm 1)\,$l/min and a relative humidity in the air stream of about 20%. The results for particles with diameters in a range of $3 - 6\,\mu$m are plotted in Figure 8.12.

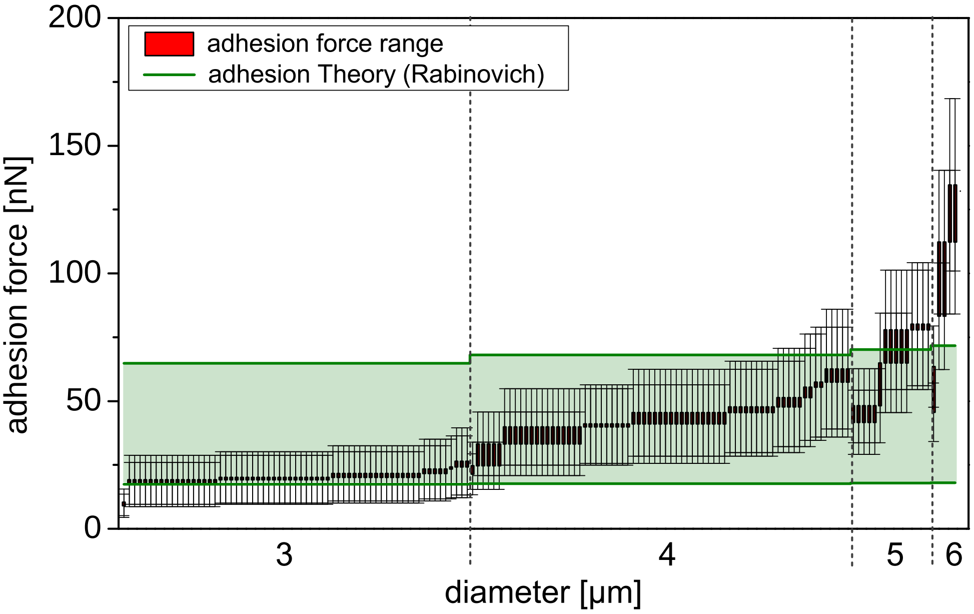

Figure 8.12: Adhesion forces (red ranges) of silica particles $(3 - 6\,\mu\text{m})$ on a polystyrene surface measured with the Hopkinson bar system in comparison with theoretical values from the Rabinovich approach (green range). Each adhesion range represents a different single particle. Here, a large number of particles could be investigated with a single experiment.

Here, adhesion forces of 157 particles could be obtained with only one experiment. This relatively large number of investigated particles allows a statistical evaluation of the data. Figure 8.13 illustrates the measured adhesion force ranges of 3 and $4\,\mu$m silica particles in a histogram. The particle fraction in the graph refers to the total number of measured particles with this size in this experiment. For better overview error bars are not shown.

Due to surface roughness and heterogeneity effects, for each particle diameter a statistical distribution of forces is obtained instead of a single value: the adhesion forces scatter around a mean value. This mean value was calculated from the average values of minimum and maximum adhesion for the 3 and $4\,\mu$m silica particles:

$\overline{F}_{adh}(3\,\mu\text{m}) = (20 \pm 2)\,\text{nN}$ and $\overline{F}_{adh}(4\,\mu\text{m}) = (43 \pm 8)\,\text{nN}$.

Additionally, the measured adhesion force ranges for the 3 and $4\,\mu$m particles were fitted with a Gaussian distribution function (Figure 8.13), which each fits the data quite well. Comparison of measured adhesion forces with theoretical predictions from the Rabinovich approach (green region in Figure 8.12) again shows good agreement for smaller particles, however, at a particle diameter of about $5 - 6\,\mu\text{m}$ a deviation from theory starts with the tendency to higher values. This is the same trend as observed in the other experiments. A possible explanation has been presented earlier.

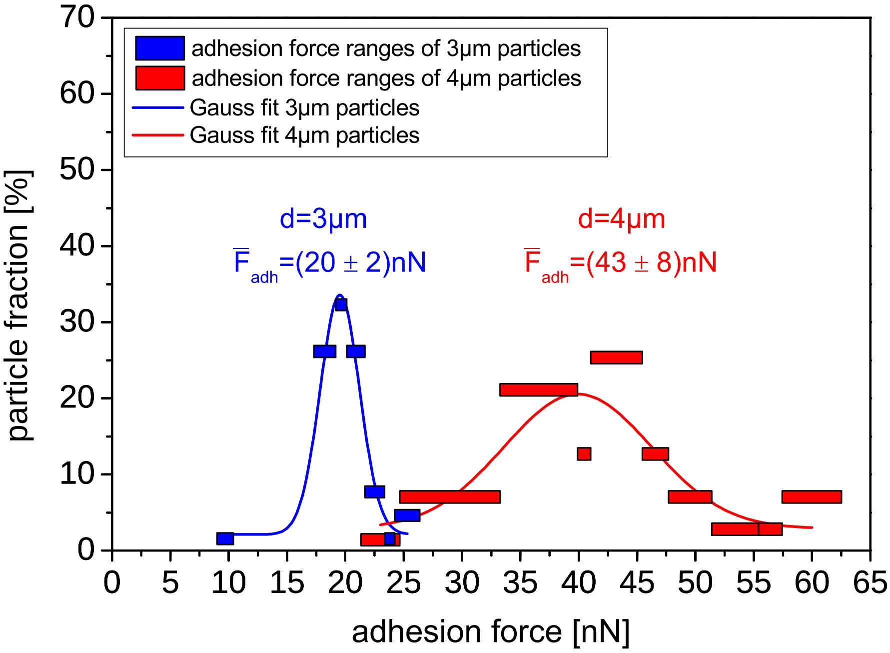

Figure 8.13: Histogram of the adhesion force of porous silica particles (diameter 3 and $4\,\mu\text{m}$) on untreated polystyrene measured with the Hopkinson bar method (red and blue ranges, respectively). Solid lines are Gaussian fits of the distributions.

8.2.5 Summary: Silica Particles

Adhesion forces of spherical porous silica particles (diameters $4 - 7\,\mu\text{m}$) were measured with the Hopkinson bar system on an untreated and a hydrophilic polystyrene surface under ambient conditions. Comparison of the adhesion forces on the untreated polystyrene with theoretical predictions by the Rabinovich model shows the same trend as observed for the polystyrene particles: an agreement for smaller particle sizes but a steeper increase with diameter than expected from theory for larger particle sizes, possibly caused by reorientation and contact area maximization.

Compared to particles on the untreated surface, particles on the hydrophilic polystyrene exhibit higher adhesion forces. The reason is presumably the higher surface energy and the influence of the capillary force in the case of the hydrophilic surface.

Furthermore, an experiment with smaller porous silica particles on an untreated polystyrene surface was carried out, where adhesion forces of particles having diameters down

to 3 µm could be obtained. Additionally, this experiment allowed a statistical evaluation of the measured adhesion forces since a large number of particles (more than 150) could be investigated.
Summarized, by measuring adhesion forces of spherical polystyrene and silica particles on a polystyrene surface and relating the results to theoretical predictions and measurements with a comparative technique, the new Hopkinson bar method developed in this thesis was successfully validated.

8.3 Dextran Particles

8.3.1 Hopkinson Bar Measurements

After the experiments with spherical particles having a well known surface chemistry, the Hopkinson bar measurements were extended to a more complex particle-surface combination. Dextran particles with a corrugated shape, consisting of Dextran T1 and Dextran T3.5 mixed in a ratio of 9:1, were used. Figure 8.14 shows an example microscope image taken during the experiment. For better overview, brightness and contrast were enhanced and a sharpening filter was employed. Regarding the optical system, a higher zoom-in was used than for the spherical particles (zoom setting 3×). Microscope images were taken at two adjacent locations on the sample.

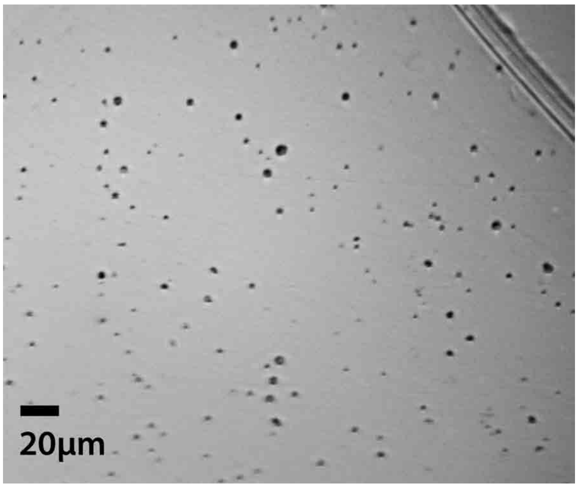

Figure 8.14: Microscope image of dextran particles (diameters $< 5\,\mu\mathrm{m}$) on a polystyrene coated surface taken during the experiment. Here, a very high magnification was used.

Since the dextran powder contained particles with sizes down to 1 µm, particles were extremely cohesive forming strong agglomerates. Additionally, as a result of the manufacturing process, nanoscale particles and particle fragments were present, as observed from SEM images. During sample preparation, these powder agglomerates were successfully dispersed in the dispersing chamber and separate single particles on the substrate were obtained (Figure 8.14). However, it cannot be excluded that nanosized particles or very small fragments (< 1 µm) still adhered to the the investigated particles.

Dextran powder is hygroscopic and thus very sensitive to humidity. Therefore, it had been stored in dry surroundings (relative humidity < 20%) using silicagel as desiccant. In order to avoid exposure to the humidity in the laboratory of (43 ± 2)% during the experiment, the Hopkinson bar set-up was covered with a polyethylene bag (Aldrich AtmosBag). After dispersing particles in a dry atmosphere onto the polystyrene substrate, the sample was immediately exposed to the air stream for horizontal dislocation of detached particles (relative humidity about 20%, flow rate (30 ± 1) l/min). The temperature was (24 ± 1)°C.

Evaluation of the taken microscope images was carried out by eye using the "photomerge" function in Photoshop (Adobe Photoshop CS3). In order to determine particle sizes from the taken microscope images, a spherical shape was approximated. The used high magnification led to a blurring of the particle border (Figure 8.14). Furthermore, not every particle was exactly in the focus of the microscope. Hence, particle diameters were determined by manually fitting a circle.

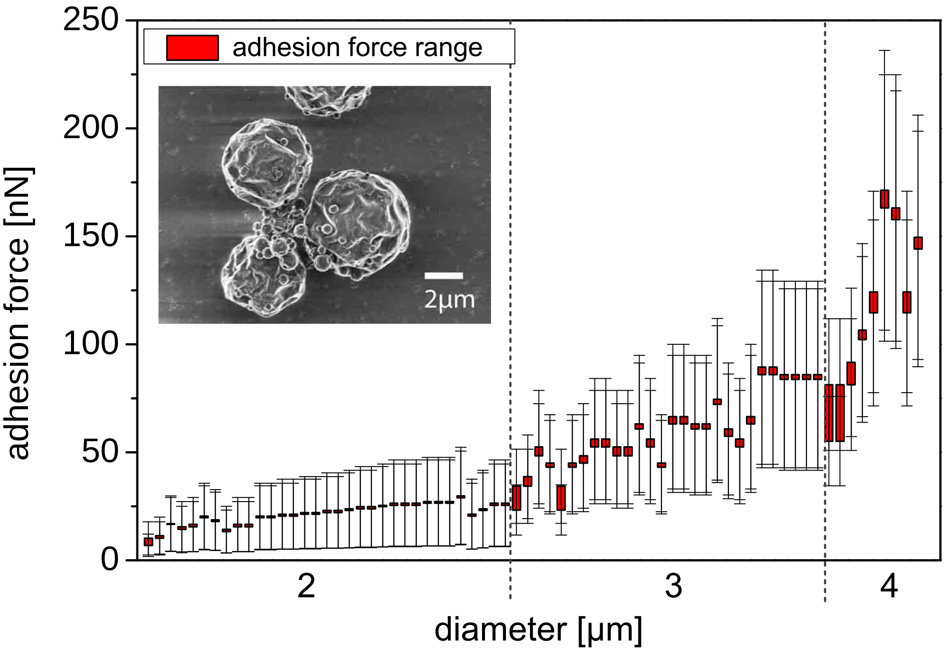

Figure 8.15: Adhesion forces (red ranges) of corrugated dextran particles on a polystyrene surface measured with the Hopkinson bar system. Each adhesion range represents a different single particle. Here, particles with diameters down to 2 µm could be investigated.

Diameters of the investigated particles were in a range of 2 − 4 µm. In total, adhesion forces of 70 corrugated dextran particles on a polystyrene surface (untreated) could be measured with this experiment. The results are plotted versus particle diameter in Figure 8.15. As expected, the adhesion forces increase with diameter from (9 ± 2) nN, which is the smallest value of the 2 µm particles, to (167 ± 6) nN, which is the largest value of the 4 µm particles. This increase with diameter seems to be stronger than a linear increase, since especially for the 4 µm particles a tendency to higher forces exists.

$\overline{F}_{adh}$ [nN] (2 µm)	$\overline{F}_{adh}$ [nN] (3 µm)	$\overline{F}_{adh}$ [nN] (4 µm)
21 ± 5	60 ± 17	116 ± 37

Table 8.4: Average adhesion force of 2 µm, 3 µm and 4 µm sized corrugated dextran particles on a polystyrene surface measured with the Hopkinson bar system.

For each particle diameter a statistical variation of the adhesion around a mean value can be observed. Table 8.4 gives an overview of the average adhesion forces of the 2 µm, 3 µm and 4 µm sized dextran particles on polystyrene. The forces were calculated from the mean values of minimum and maximum adhesion measured for each detached particle. In Figure 8.16 the forces of 2 and 3 µm particles are plotted as histogram.

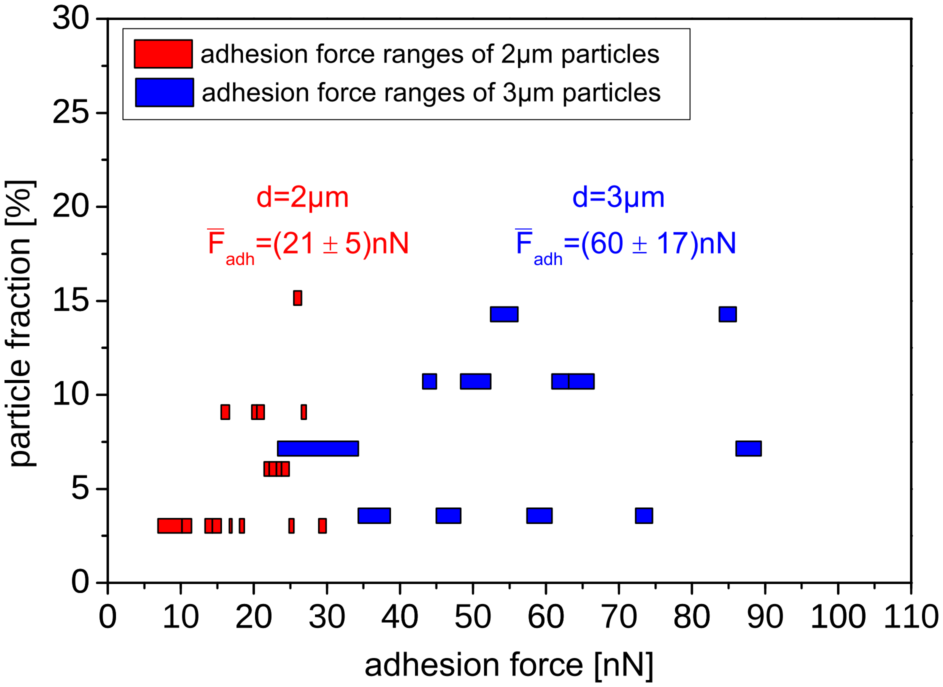

Figure 8.16: Histogram of the adhesion force of 2 and 3 µm sized corrugated dextran particles (red and blue ranges, respectively) on polystyrene measured with the Hopkinson bar method.

Compared to the adhesion of porous silica particles having the same diameter (chapter 8.2), the adhesion values of the dextran particles are higher. Considering for example the 3 µm particles, the adhesion of the dextran particles was about a factor 3 higher ($\overline{F}_{adh}(3\,\mu\mathrm{m}) = 20 \pm 2\,\mathrm{nN}$ for silica, $\overline{F}_{adh}(3\,\mu\mathrm{m}) = 60 \pm 17\,\mathrm{nN}$ for dextran). Compared to a spherical silica particle, a corrugated dextran particle of the same diameter should have a smaller contact area, touching the surface only with few of its curvatures. However, the dextran particles seem to have a much higher surface energy compared to silica and a lower nanoscale surface roughness. Furthermore, capillary forces due to formation of water bridges might have played a role, in spite of the dry surroundings. These effects seem to dominate compared to the corrugation, leading to higher adhesion forces.

8.3.2 Conclusion: Dextran Particles

Concluding, by measuring adhesion forces of corrugated dextran particles on a polystyrene surface it was possible to demonstrate that the Hopkinson bar system can be used to study more complex particle-surface combinations as well.

Being extremely sensitive to humidity and strongly cohesive, dextran powders with particle sizes below 5 µm are difficult to handle. Therefore, they represent fine powders, used for example in pharmaceutical industry, which cause difficulties in powder handling and processing due to their poor flow and dispersion properties. Corrugated particles are of particular interest in industrial research since it has been proved earlier that particle surface corrugation enhances the dispersibility [21] and thus improves the aerosol performance in dry powder inhalers, for instance. The polystyrene surface used in this thesis can be regarded as model system, e.g. for the wall in an inhaler device.

With the Hopkinson bar it was possible to measure adhesion forces of dextran particles down to 2 µm. This is of great significance, since it includes inhalation powders with typical particle diameters in a range of $1 - 5\,\mu\mathrm{m}$. Hence, the Hopkinson bar offers the possibility to directly measure adhesion forces of drug particles and correlate the results with the dispersion and aerosolization properties of the powders. This is a crucial step for the optimization of inhalation powders.

8.4 Discussion: The Hopkinson Bar Method

8.4.1 Which Factors potentially influence Adhesion?

With the Hopkinson bar method, which was developed in this thesis, adhesion of particles can be measured by inertial detachment caused by a mechanical excitation of the sample surface. This is realized by applying a series of shock pulses with stepwise increasing acceleration to the sample, which is attached to the Hopkinson bar, and detecting particle detachment. However, in how far does the adhesion obtained from such a measurement represent the true particle adhesion?

In order to determine the adhesion force one has to presuppose that in the moment of particle detachment the adhesion equals the normal detachment force, which is the particle mass m_P times the normal acceleration of the surface a in direction of the laser beam, measured with the laser Doppler vibrometer: $F_{adh} = F_{detach} = m_P \cdot a$. A possible lateral acceleration component, perpendicular to the laser beam, cannot be recorded with the vibrometer. In the case of a present lateral component, the obtained adhesion force would be smaller than the real particle adhesion, since an additional lateral detachment force would act on the particles parallel to the sample surface, which is not considered.

The main factor, which might generate a lateral acceleration component, would be the presence of transversal waves in the Hopkinson bar. As a consequence, a lateral force would be transferred to the sample plate and act on the particles. However, it has been proved that the acceleration at the bar's end is mainly generated by longitudinal waves [99]. A longitudinal and a transversal wave have different propagation velocities in the same medium. Usually the longitudinal wave propagates faster. Hence, by measuring the duration time between the force pulse at the left bar's end and the resulting acceleration pulse at the right bar's end one can determine the type of wave. For the used Hopkinson bar, transversal waves can be neglected.

Thus, a possible lateral acceleration could only be generated by the sample plate itself. Measurement of the displacement shows an elastic behavior of the steel substrate additionally to the forward movement of bar and sample: the overlapping edges first bend forward and subsequently snap backwards during the shock pulse (small overshot peak in Figure 5.8, right). It cannot be completely excluded, that this elastic response of the substrate potentially causes a lateral acceleration component. However, since the bending of the sample plate seems to be quite small (about 60 μm in direction of the laser beam) and no plastic deformation could be observed, a possible lateral acceleration component should also be rather small. Compared to the measuring accuracy of the Hopkinson bar system (chapter 8.4.2) it should be negligible.

Above the measuring limit of the laser vibrometer acceleration values are obtained from a calibration plot. Therefore one has to assume that the linear relation between the acceleration length of the projectile (distance from which it is shot to the bar's end) and the acceleration on the sample still exists. No indication could be found that the linear behavior gets lost above the vibrometer limit, but it cannot be excluded that the curve flattens at a certain acceleration. However, the measuring error of the adhesion force should most likely include this effect.

Another factor, which might cause a deviation of the adhesion force obtained with the Hopkinson bar from the true particle adhesion, could be the presence of the lateral air stream, which is applied in the set-up to remove detached particles. Lift and drag forces in the flow might reduce the force needed to detach particles from the surface. However, an estimation of fluid forces, which was performed in this work (chapter 5.5), shows a negligible contribution at the used flow rates.

In the Hopkinson bar set-up the particles are exposed to a series of shock pulses. Typically the number of excited pulses is between 20 and 30, depending on the investigated particle-surface combination. Thus, in how far has this number an influence on particle adhesion? Does the adhesion of a particle depend on its "history", i.e. the number of pulses it experienced?

Smaller particles in the Hopkinson bar set-up were generally exposed to more shock pulses compared to the larger ones, since they detached later due to their smaller inertia. However, for the smaller particles in particular, adhesion force measurements with the Hopkinson bar show an agreement with theoretical predictions and colloidal probe measurements. Hence, there is no indication that the shock pulses influence particle adhesion. To the contrary, it seems that small particles remain at the point of first contact kept in position and do not rearrange on the surface at all since their inertia is too weak to overcome rolling friction (chapter 8.1.2). Regarding the larger particles, the shock pulses might cause particle rearrangement on the surface leading to contact area maximization. This could explain why for larger particles forces measured with the Hopkinson bar device are higher than measured with the colloidal probe technique or theoretically predicted. Rearrangement of particles also occurs in powders, during any kind of industrial powder handling and processing, for instance. The statistical variation of the adhesion, which is a fundamental property caused by surface roughness and heterogeneity, makes it difficult to identify a clear trend. However, during the experiments no indication could be found that the number of shock pulses systematically influences adhesion of particles.

Thus, within the accuracy limits of the Hopkinson bar method, the measured forces should represent the true particle adhesion reasonably and reliably.

8.4.2 Measuring Accuracy of the Hopkinson Bar Method

In the Hopkinson bar set-up particles are detached from a surface by stepwise increase of the acceleration. Therefore, not a single adhesion value is measured for each detached particle, but an adhesion force range. The step width of the acceleration determines the size of this force range. The shock pulse reproducibility of about 5% limits the minimum reasonable step width to $5\,000 - 20\,000\,g$. Accordingly, the adhesion force of a particle can be narrowed down to a range of a few nN or a few hundred nN, depending on its diameter and density.

Additionally, a measuring error has to be considered for the upper and the lower limit of the adhesion force range. It consists of the error of acceleration, measured with the laser Doppler vibrometer (inaccuracy 1.5%) or determined from the calibration plot (reproducibility 5%) and the error of the diameter, determined from the microscope images (estimated $\Delta d = 0.5\,\mu\text{m}$). In all graphs, shown in this thesis, the maximum adhesion errors are plotted. Since the diameter error might have been overestimated, the real measuring error might possibly be smaller.

9 Summary, Conclusion and Outlook

9.1 Summary and Conclusion

In this thesis a new method to measure adhesion forces of micrometer-sized powder particles was developed as an alternative to the established colloidal probe and centrifuge technique.

The new method is based on particle detachment from a surface caused by its inertia. The required acceleration in the order of $500\,000\,g$ is provided by a shock excitation system using a Hopkinson bar, which the substrate with the particles is attached to. By mechanical impact an elastic wave is generated travelling through the bar and causing the acceleration at the bar's end. Stepwise increase of the acceleration leads to successive detachment of particles from the surface. The acting acceleration on the substrate is measured via laser Doppler vibrometry and particle detachment events are detected on-line by optical video microscopy. Subsequent automated data evaluation allows obtaining a statistical distribution of adhesion forces. Here, many individual particles can be investigated simultaneously (particle collectives).

After construction of the experimental set-up, the new method was validated by measuring adhesion forces for ensembles of single polystyrene and silica microspheres (diameter range $3 - 13\,\mu\text{m}$) on a polystyrene coated surface under ambient conditions. Measured adhesion forces of smaller particles showed an agreement with values from colloidal probe measurements and theoretical predictions of the Rabinovich model. However, for the larger particles a steeper increase of adhesion with diameter was observed than theoretically predicted or measured with the colloidal probe technique. This discrepancy might be induced by surface roughness and heterogeneity that influence small and large particles differently. A possible reorientation of larger particles by inertia during particle deposition on the surface and during the shock pulses might lead to stronger adhesive forces due to surface area maximization. For small particles, in contrast, attractive forces such as van der Waals might be so strong that they are unable to adjust on the surface.

Furthermore, measurements were carried out with corrugated dextran particles, which are strongly cohesive and humidity sensitive. Here, adhesion forces of particles with sizes down to $2\,\mu\text{m}$ were obtained. Thus, it could be demonstrated that the Hopkinson bar system offers the possibility to study more complex particle-surface combinations as well.

In conclusion, the Hopkinson bar method is a valuable alternative to the established techniques. Since adhesion forces of many single particles can be measured simultaneously, the method offers a statistical evaluation of the data, in contrast to the colloidal probe technique, where only single particle experiments are possible. Using the Hopkinson bar, in this thesis more than 150 individual particles could be investigated with a single experiment and there is the potential to even enhance this number.

Additionally, sample preparation and measuring effort as well as measuring time are considerably lower compared to the established techniques. As the developed optical system allows an on-line imaging of the sample surface, it is not necessary to remove the substrate after each acceleration step for image analysis, in contrast to the centrifuge method. Thus the new device has the potential to be used as routine tool.

Another advantage is the random orientation of the particles on the substrate, which can adjust freely like in real powders. In contrast, for a colloidal probe the orientation of the particle and thus the direction of contact is predetermined.

Thus, the Hopkinson bar method will be applicable to study a broad variety of particle-surface combinations on a routine basis, including strongly cohesive powders with particle sizes down to 2 μm. This is of particular relevance for fundamental as well as for industrial research. The new device provides various opportunities to extend the basic knowledge of mechanical microcontacts, for example by gaining a deeper insight on the influence of surface roughness and heterogeneity on adhesion. However, it might also be an important tool for standard analysis in industry. Especially in pulmonary drug delivery an improvement of the dispersibility of cohesive inhalation powders is desirable. These powders typically contain particles in a size range of $1 - 5\,\mu$m. The Hopkinson bar method offers the chance to directly measure adhesion forces of drug particles and correlate the results with the dispersion and aerosolization properties of the powders. Hence, it might be possible to identify parameters improving the dispersibility of pharmaceutical drug powders by a systematic scientific approach. This is a crucial step in order to enhance the performance of inhalation products.

9.2 Outlook for Future

The Hopkinson bar set-up, which was constructed in this thesis, offers some possibilities to be further developed or extended.

In order to perform adhesion measurements of particles under controlled environmental conditions, a humidity chamber could be developed enclosing the sample attached to the bar's end. A possibility to control the water vapor pressure would be by mixing a gas stream of dry nitrogen with a gas stream of nitrogen saturated with water vapor in a defined mixing ratio.

Additionally, there is the potential to further reduce the measuring time, for example by providing the optical system with an automatic focus for faster imaging.

In this thesis, the Hopkinson bar was used to study adhesion forces between particles and a substrate, however, it might be possible to study friction forces as well. By designing a sample plate where particles are placed on top, according to Figure 9.1, one could observe rolling or sliding on the surface and thus gain valuable information about particle friction.

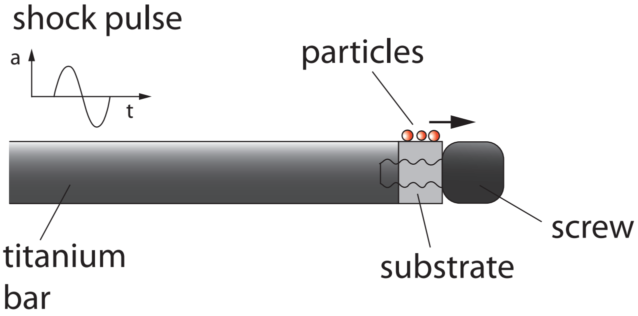

Figure 9.1: Future perspective: proposed sample configuration to study friction forces using the Hopkinson bar.

References

1. S. P. Newman and S. W. Clarke. Therapeutic aerosols 1. Physical and practical considerations. *Thorax*, 38(12):881–886, 1983.
2. J. Heyder. Deposition of inhaled particles in the human respiratory tract and consequences for regional targeting in respiratory drug delivery. *Proceedings of the American Thoracic Society*, 1:315–320, 2004.
3. J. S. Patton, C. S. Fishburn, and J. G. Weers. The lungs as a portal of entry for systemic drug delivery. *Proceedings of the American Thoracic Society*, 1(4):338–44, 2004.
4. W. F. Tonnis, G. F. Kersten, H. W. Frijlink, W. L. J. Hinrichs, A. H. de Boer, and J.-P. Amorij. Pulmonary Vaccine Delivery: A Realistic Approach? *Journal of Aerosol Medicine and Pulmonary Drug Delivery*, 25(5):249–260, 2012.
5. T. C. Carvalho, J. I. Peters, and R. O. Williams. Influence of particle size on regional lung deposition - What evidence is there? *International Journal of Pharmaceutics*, 406(1-2):1–10, 2011.
6. M. B. Dolovich, N. R. MacIntyre, P. J. Anderson, C. A. Camargo, N. Chew, C. H. Cole, R. Dhand, J. B. Fink, N. J. Gross, D. R. Hess, A. J. Hickey, C. S. Kim, T. B. Martonen, D. J. Pierson, B. K. Rubin, and G. C. Smaldone. Consensus statement: Aerosols and delivery devices. *Journal of Aerosol Medicine*, 13(3):291–300, 2000.
7. A. H. L. Chow, H. H. Y. Tong, P. Chattopadhyay, and B. Y. Shekunov. Particle engineering for pulmonary drug delivery. *Pharmaceutical Research*, 24(3):411–437, 2007.
8. M. Schäfer-Korting. *Drug delivery.* Springer Verlag, Berlin, Heidelberg, 2010.
9. S. Luding. Cohesive, frictional powders: contact models for tension. *Granular Matter*, 10(4):235–246, 2008.
10. M. Röck, M. Morgeneyer, J. Schwedes, D. Kadau, L. Brendel, and D. E. Wolf. Steady state flow of cohesive and non-cohesive powders. *Granular Matter*, 10(4):285–293, 2008.

11. S. Herminghaus. Dynamics of wet granular matter. *Advances in Physics*, 54(3):221–261, 2005.

12. Q. C. Sun, G. Q. Wang, and K. H. Hu. Some open problems in granular matter mechanics. *Progress in Natural Science*, 19(5):523–529, 2009.

13. I. S. Aranson and L. S. Tsimring. Patterns and collective behavior in granular media: Theoretical concepts. *Reviews of Modern Physics*, 78(2):641–692, 2006.

14. H. Krupp. *Advances in Colloid and Interface Science*, 1:111–239, 1967.

15. L. O. Heim, J. Blum, M. Preuss, and H. J. Butt. Adhesion and friction forces between spherical micrometer-sized particles. *Physical Review Letters*, 83(16):3328–3331, 1999.

16. L. O. Heim, S. Ecke, M. Preuss, and H. J. Butt. Adhesion forces between individual gold and polystyrene particles. *Journal of Adhesion Science and Technology*, 16(7):829–843, 2002.

17. Y. I. Rabinovich, J. J. Adler, A. Ata, R. K. Singh, and B. M. Moudgil. Adhesion between nanoscale rough surfaces - II. Measurement and comparison with theory. *Journal of Colloid and Interface Science*, 232(1):17–24, 2000.

18. M. Farshchi-Tabrizi, M. Kappl, Y. J. Cheng, J. Gutmann, and H. J. Butt. On the adhesion between fine particles and nanocontacts: An atomic force microscope study. *Langmuir*, 22(5):2171–2184, 2006.

19. K. Cooper, A. Gupta, and S. Beaudoin. Simulation of the adhesion of particles to surfaces. *Journal of Colloid and Interface Science*, 234(2):284–292, 2001.

20. M. Götzinger and W. Peukert. Particle adhesion force distributions on rough surfaces. *Langmuir*, 20(13):5298–5303, 2004.

21. C. Weiler, M. Egen, M. Trunk, and P. Langguth. Force control and powder dispersibility of spray dried particles for inhalation. *Journal of Pharmaceutical Sciences*, 99(1):303–316, 2010.

22. C. Weiler, M. Wolkenhauer, M. Trunk, and P. Langguth. New model describing the total dispersion of dry powder agglomerates. *Powder Technology*, 203(2):248–253, 2010.

23. N. Y. K. Chew and H. K. Chan. Use of solid corrugated particles to enhance powder aerosol performance. *Pharmaceutical Research*, 18(11):1570–1577, 2001.

24. N. Y. K. Chew, P. Tang, H. K. Chan, and J. A. Raper. How much particle surface corrugation is sufficient to improve aerosol performance of powders? *Pharmaceutical Research*, 22(1):148–152, 2005.

25. D. Lechuga-Ballesteros, C. Charan, C. L. M. Stults, C. L. Stevenson, D. P. Miller, R. Vehring, V. Tep, and M. Kuo. Trileucine improves aerosol performance and stability of spray-dried powders for inhalation. *Journal of Pharmaceutical Sciences*, 97(1):287–302, 2008.

26. H.-J. Butt, M. Makowski, M. Kappl, and A. Ptak. On the adhesion between individual particles. *Kona Powder and Particle Journal*, 29:53–66, 2011.

27. M. Kappl and H. J. Butt. The colloidal probe technique and its application to adhesion force measurements. *Particle & Particle Systems Characterization*, 19(3):129–143, 2002.

28. B. Cappella, H.-J. Butt, and M. Kappl. Force measurements with the atomic force microscope: Technique, interpretation and applications. *Surface Science Reports*, 59(1-6), 2005.

29. G. Boehme, H. Krupp, H. Rabenhost, and G. Sandstede. Adhesion measurements involving small particles. *Transactions of the Institution of Chemical Engineers*, 40:252–259, 1962.

30. F. Podczeck, J. M. Newton, and M. B. James. Adhesion and friction between powders and polymer or aluminum surfaces determined by a centrifuge technique. *Powder Technology*, 83(3):201–209, 1995.

31. F. Podczeck, J. M. Newton, and M. B. James. Variations in the adhesion force between a drug and carrier particles as a result of changes in the relative humidity of the air. *International Journal of Pharmaceutics*, 149(2):151–160, 1997.

32. F. Podczeck. Investigations into the reduction of powder adhesion to stainless steel surfaces by surface modification to aid capsule filling. *International Journal of Pharmaceutics*, 178(1):93–100, 1999.

33. H.-J. Butt and M. Kappl. *Surface and Interfacial Forces*. Wiley-VCH, 2010.

34. H.-J. Butt, K. Graf, and M. Kappl. *Physics and chemistry of interfaces*. Wiley-VCH, 2nd edition, 2006.

35. W. H. Keesom. On Waal's cohesion forces. *Physikalische Zeitschrift*, 22:129, 1921.

36. P. Debye. The van der Waals cohesion forces. *Physikalische Zeitschrift*, 21:178, 1920.

37. F. London. On the theory and systematic of molecular forces. *Zeitschrift für Physik*, 63:245, 1930.

38. H. C. Hamaker. The London - van der Waals attraction between spherical particles. *Physica*, 4:1058–1072, 1937.

39. E. M. Lifshitz. The theory of molecular attractive forces between solids. *Soviet Physics JETP-USSR*, 2:73–83, 1956.

40. I. E. Dzyaloshinskii, E. M. Lifshitz, and L. P. Pitaevskii. The general theory of van der Waals forces. *Advances in Physics*, 10(38):165–209, 1961.

41. W. Pietsch and H. Rumpf. Adhesion, capillary pressure, liquid volume and angle of contact of a liquid bridge between two spheres. *Chemie Ingenieur Technik*, 39(15):885–936, 1967.

42. H. Schubert. Kapillardruck und Zugfestigkeit von feuchten Haufwerken aus körnigen Stoffen. *Chemie Ingenieur Technik*, 45(6):396–401, 1973.

43. N. Harnby, A. E. Hawkins, and I. Opalinski. Measurement of the adhesional force between individual particles with moisture present. *Chemical Engineering Research & Design*, 74(A6):605–626, 1996.

44. L. Bocquet, E. Charlaix, S. Ciliberto, and J. Crassous. Moisture-induced ageing in granular media and the kinetics of capillary condensation. *Nature*, 396(6713):735–737, 1998.

45. Y. I. Rabinovich, M. S. Esayanur, K. D. Johanson, J. J. Adler, and B. M. Moudgil. Measurement of oil-mediated particle adhesion to a silica substrate by atomic force microscopy. *Journal of Adhesion Science and Technology*, 16(7):887–903, 2002.

46. Z. Fournier, D. Geromichalos, S. Herminghaus, M. M. Kohonen, F. Mugele, M. Scheel, M. Schulz, B. Schulz, C. Schier, R. Seemann, and A. Skudelny. Mechanical properties of wet granular materials. *Journal of Physics: Condensed Matter*, 17(9):S477–S502, 2005.

47. M. Fuji, K. Machida, T. Takei, T. Watanabe, and M. Chikazawa. Effect of wettability on adhesion force between silica particles evaluated by atomic force microscopy measurement as a function of relative humidity. *Langmuir*, 15(13):4584–4589, 1999.

48. R. Price, P. M. Young, S. Edge, and J. N. Staniforth. The influence of relative humidity on particulate interactions in carrier-based dry powder inhaler formulations. *International Journal of Pharmaceutics*, 246(1-2):47–59, 2002.

49. T. Young. An essay on the cohesion of fluids. *Philosophical Transactions of the Royal Society of London*, 95:65–87, 1805.

50. P. S. Laplace. Sur l'action capillarie. *Dixieme Livre du Traite de Mecanique Celeste*, pages 1–65, 1805-1806. Paris.

51. L. M. Skinner and J. R. Sambles. The Kelvin equation - A review. *Journal of Aerosol Science*, 3(3):199–210, 1972.

52. H.-J. Butt and M. Kappl. Normal capillary forces. *Advances in Colloid and Interface Science*, 146(1-2):48–60, 2009.

53. M. Fuji, K. Machida, T. Takei, T. Watanabe, and M. Chikazawa. Effect of surface geometric structure on the adhesion force between silica particles. *Journal of Physical Chemistry B*, 102(44):8782–8787, 1998.

54. V. L. Popov. *Kontaktmechanik und Reibung.* Springer-Verlag Berlin Heidelberg, 2010.

55. H. Hertz. Über die Berührung fester elastischer Körper. *Journal für die reine und angewandte Mathematik*, 92:156, 1882.

56. I. N. Sneddon. The relation between load and penetration in the axisymmetric boussinesq problem for a punch of arbitrary profile. *International Journal of Engineering Science*, 3(1):47–57, 1965.

57. T. C. T. Ting. The contact stresses between a rigid indenter and a viscoelastic half-space. *Journal of Applied Mechanics*, 33(4):845–854, 1966.

58. K. L. Johnson, K. Kendall, and A. D. Roberts. Surface energy and the contact of elastic solids. *Proceedings of the Royal Society London A*, 324:301–313, 1971.

59. B. V. Derjaguin, V. M. Muller, and Y. P. Toporov. Effect of contact deformations on adhesion of particles. *Journal of Colloid and Interface Science*, 53(2):314–326, 1975.

60. D. Tabor. Surface forces and surface interactions. *Journal of Colloid and Interface Science*, 58(1):2–13, 1977.

61. D. Maugis. Adhesion of spheres - The JKR-DMT transition using a Dugdale model. *Journal of Colloid and Interface Science*, 150(1):243–269, 1992.

62. J. A. Greenwood and J. B. P. Williamson. Contact of nominally flat surfaces. *Proceedings of the Royal Society of London A*, 295(1442):300, 1966.

63. K. N. G. Fuller and D. Tabor. Effect of surface roughness on adhesion of elastic solids. *Proceedings of the Royal Society of London A*, 345(1642):327–342, 1975.

64. K. Iida, A. Otsuka, K. Danjo, and H. Sunada. Measurement of the adhesive force between particles and a substrate by means of the impact separation method - effect of the surface roughness and type of material of the substrate. *Chemical & Pharmaceutical Bulletin*, 41(9):1621–1625, 1993.

65. H. Rumpf. Die Wissenschaft des Agglomerierens. *Chemie Ingenieur Technik*, 46(1):1–11, 1974.

66. Y. I. Rabinovich, J. J. Adler, A. Ata, R. K. Singh, and B. M. Moudgil. Adhesion between nanoscale rough surfaces - I. Role of asperity geometry. *Journal of Colloid and Interface Science*, 232(1):10–16, 2000.

67. G. Binning, C. F. Quate, and C. Gerber. Atomic force microscope. *Physical Review Letters*, 56(9):930–933, 1986.

68. R. Garcia and R. Perez. Dynamic atomic force microscopy methods. *Surface Science Reports*, 47(6-8):197–301, 2002.

69. W. A. Ducker, T. J. Senden, and R. M. Pashley. Direct measurement of colloidal forces using an atomic force microscope. *Nature*, 353:239–241, 1991.

70. W. A. Ducker, T. J. Senden, and R. M. Pashley. Measurement of forces in liquid using a force microscope. *Langmuir*, 8:1831–1836, 1992.

71. H.-J. Butt. Measuring electrostatic, van der Waals, and hydration forces in electrolyte solutions with an atomic force microscope. *Biophysical Journal*, 60(6):1438–1444, 1991.

72. J. L. Hutter and J. Bechhoefer. Calibration of atomic force microscope tips. *Review of Scientific Instruments*, 64(7):1868–1873, 1993.

73. J. L. Hutter. Comment on tilt of atomic force microscope cantilevers: effect on spring constant and adhesion measurements. *Langmuir*, 21(6):2630–2632, 2005.

74. B. Ohler. Cantilever spring constant calibration using laser Doppler vibrometry. *Review of Scientific Instruments*, 78(6), 2007.

75. K. K. Lam and J. M. Newton. Investigation of applied compression on the adhesion of powders to a substrate surface. *Powder Technology*, 65(1-3):167–175, 1991.

76. H. Mizes, M. Ott, E. Eklund, and D. Hays. Small particle adhesion: measurement and control. *Colloids and Surfaces A - Physicochemical and Engineering Aspects*, 165(1-3):11–23, 2000.

77. G. R. Salazar-Banda, M. A. Felicetti, J. A. S. Goncalves, J. R. Coury, and M. L. Aguiar. Determination of the adhesion force between particles and a flat surface using the centrifuge technique. *Powder Technology*, 173(2):107–117, 2007.

78. K. F. Graff. *Wave motion in elastic solids.* Dover Publications, 1975.

79. B. Hopkinson. A method of measuring the pressure produced in the detonation of high explosives or by the impact of bullets. *Philosophical Transactions of the Royal Society of London - Series A*, 213:437–456, 1914.

80. B. W. Abbott and R. H. Cornish. A stress wave technique for determining the tensile strength of brittle materials. *Experimental Mechanics*, 5(5):148–153, 1965.

81. H. Kolsky. *Stress waves in solids.* Dover Publications, 1963.

82. R. A. Eubanks, D. Muster, and E. G. Volterra. An investigation of the dynamic properties of plastics and rubber-like materials. Technical Report 1, Mechanics Department Illinois Institute of Technology, Chicago, 1952.

83. T. C. Togami, V. I. Bateman, and F. A. Brown. Evaluation of a Hopkinson bar fly away technique for high amplitude shock accelerometer calibration. In *68. Shock and Vibration Symposium*, Baltimore (United States), 1997.

84. R. M. Davies. A critical study of the Hopkinson pressure bar. *Philosophical Transactions of the Royal Society of London - Series A*, 240(821):375–457, 1948.

85. H. Kolsky. An investigation of the mechanical properties of materials at very high rates of loading. *Proceedings of the Physical Society - Section B*, 62:676–700, 1949.

86. Q. Deng, Y. Li, T. Suo, C. Chen, and X. Chang. Study of initiator's shock resistibility through impact using Hopkinson pressure bar. In *Advanced Materials Research, 7th International Conference on Fracture and Strength of Solids*, volume 33-37, pages 401–406, China, 2008.

87. J. Huang, S. Xu, and S. Hu. Effects of grain size and gradation on the dynamic responses of quartz sands. *International Journal of Impact Engineering*, 59:1–10, 2013.

88. A. Umeda and K. Ueda. Study on the dynamic force/acceleration measurements. *Sensors and Actuators A - Physical*, 21(1-3):285–288, 1990.

89. Y. Zhang, J. Zu, and H.-Y. Zhang. Dynamic calibration method of high-pressure transducer based on quasi-delta function excitation source. *Measurement*, 45(8):1981–1988, 2012.

90. Physikalisch-Technische Bundesanstalt Braunschweig (Germany). Stoß-Beschleunigungserreger mit drei Hopkinson-Stäben. `http://www.ptb.de/cms/fachabteilungen/abt1/fb-17/ag-171/forschung-und-entwicklung-01/stoss-beschleunigungserreger-1-000-ms2-bis-100-000-ms2.html`. [02.10.2013, 14:59].

91. H. Nicklich and M. Brucke. Latest design of sine and shock exciters for calibration purposes. In *1st IMEKO TC22 International Conference*, Merida (Mexico), 2007.

92. H. Nicklich, M. Brucke, and M. Mende. The need for controlled shocks - A new type of shock exciter allows to apply well defined mechanical shocks. In *Fundamental and Applied Metrology, 19th IMEKO World Congress*, pages 2512–2515, Lisbon (Portugal), 2009.

93. SPEKTRA Schwingungstechnik und Akustik GmbH Dresden (Germany). SE-221 HOP-HS Hopkinson-Stab Stoßerreger. `http://www.spektra-dresden.de/spektra/index.php?option=com_content&view=article&id=121%3Ase-221-hop-hs-hopkinson-stab-stosserreger&catid=49%3Astosserreger&Itemid=60&lang=de`. [02.10.2013, 15:21].

94. B. V. Derjaguin and A. D. Zimon. Adhesion of particles of a powder to plane surfaces. *Kolloidnyi Zhurnal*, 23(5):544–552, 1961.

95. K. Hein, T. Hucke, M. Stintz, and S. Ripperger. Analysis of adhesion forces between particles and wall based on the vibration method. *Particle & Particle Systems Characterization*, 19(4):269–276, 2002.

96. S. Ripperger and T. Hucke. Measurement of adhesion forces between particles and rough substrates in air with the vibration method. *Kona Powder and Particle Journal*, 22:121–133, 2004.

97. H. Mueller. *Stoßförmige Kalibrierung von Beschleunigungsaufnehmern nach dem Vergleichsverfahren.* PhD thesis, Technische Universität Braunschweig, 2001.

98. SPEKTRA Schwingungstechnik und Akustik GmbH Dresden (Germany). Pneumatischer Stoßerreger, Stoßpendel. `http://www.spektra-dresden.de/spektra/index.php?option=com_content&view=category&layout=blog&id=49&Itemid=60&lang=de`. [02.10.2013, 15:57].

99. M. Brucke. *Alternative Methoden zur Anregung von Wellen in Stäben zur Kalibrierung von Beschleunigungsaufnehmern.* PhD thesis, Technische Universität Braunschweig, 2010.

100. D. Leighton and A. Acrivos. The lift on a small sphere touching a plane in the presence of a simple shear flow. *Zeitschrift für angewandte Mathematik und Physik*, 36(1):174–178, 1985.

101. P. Cherukat and J. B. McLaughlin. The inertial lift on a rigid sphere in a linear shear flow field near a flat wall. *Journal of Fluid Mechanics*, 263:1–18, 1994.

102. M. E. O'Neill. A sphere in contact with a plane wall in a slow linear shear flow. *Chemical Engineering Science*, 23(11):1293–1298, 1968.

103. G. Lacaze, M. Wick, and S. Cappelle. Emerging fermentation technologies: Development of novel sourdoughs. *Food Microbiology*, 24(2):155–160, 2007.

104. N. Vogel, S. Goerres, K. Landfester, and C. K. Weiss. A convenient method to produce close- and non-close-packed monolayers using direct assembly at the air-water interface and subsequent plasma-induced size reduction. *Macromolecular Chemistry and Physics*, 212(16):1719–1734, 2011.

105. C. W. Extrand. Spin coating of very thin polymer films. *Polymer Engineering and Science*, 34(5):390–394, 1994.

106. D. B. Hall, P. Underhill, and J. M. Torkelson. Spin coating of thin and ultrathin polymer films. *Polymer Engineering and Science*, 38(12):2039–2045, 1998.

107. M.-S. Kim, J.-H. Choi, J.-H. Kim, and Y.-K. Park. Accurate determination of spring constant of atomic force microscope cantilevers and comparison with other methods. *Measurement*, 43:520–526, 2010.

Glossary

AFM	atomic force microscope/microscopy
ASCII	American standard code for information interchange (character-encoding scheme)
CF	cystic fibrosis
COPD	chronic obstructive pulmonary disease
DMT	Derjaguin, Muller and Toporov
DPI	dry powder inhaler
DVB	divinylbenzene
e.g.	exempli gratia, for example
i.e.	id est, that is
JKR	Johnson, Kendall and Roberts
PS	polystyrene
rms	root mean square
rpm	revolutions per minute
sccm	standard cubic centimeters per minute
SEM	scanning electron microscope/microscopy

List of Figures

List of Tables

Acknowledgements

[In der elektronischen Fassung aus Datenschutzgründen entfernt]

Curriculum Vitae

[In der elektronischen Fassung aus Datenschutzgründen entfernt]